

Unclassified

SECURITY CLASSIFICATION OF THIS PAGE

DTIC FILE COPY

2

Form Approved
OMB No. 0704-0188

REPORT DOCUMENTATION PAGE			
1a. REPORT SECURITY CLASSIFICATION Unclassified		1b. RESTRICTIVE MARKINGS	
AD-A218 331 <small>20. DECLASSIFICATION/DISSEMINATION SCHEDULE EEB 23 1990</small>		3. DISTRIBUTION/AVAILABILITY OF REPORT Approved for public release; Distribution unlimited	
4. PERFORMING ORGANIZATION REPORT NUMBER(S)		5. MONITORING ORGANIZATION REPORT NUMBER(S) AFOSR - TR. 90 - 0240	
6a. NAME OF PERFORMING ORGANIZATION Johns Hopkins University	6b. OFFICE SYMBOL (if applicable) NC	7a. NAME OF MONITORING ORGANIZATION AFOSR/NC	
6c. ADDRESS (City, State, and ZIP Code) 34th and Charles Streets Baltimore, MD 21218		7b. ADDRESS (City, State, and ZIP Code) Building 410 Bolling AFB, DC 20332-6448	
8a. NAME OF FUNDING/SPONSORING ORGANIZATION AFOSR	8b. OFFICE SYMBOL (if applicable) NC	9. PROCUREMENT INSTRUMENT IDENTIFICATION NUMBER AFOSR-87-0320	
8c. ADDRESS (City, State, and ZIP Code) Building 410 Bolling AFB, DC 20332-6448		10. SOURCE OF FUNDING NUMBERS	
		PROGRAM ELEMENT NO 61102F	PROJECT NO. 3303
		TASK NO. A3	WORK UNIT ACCESSION NO.
11. TITLE (Include Security Classification) Ultrastructure Processing of Ordered Polymers			
12. PERSONAL AUTHOR(S) R.K. Eby			
13a. TYPE OF REPORT Final	13b. TIME COVERED FROM 8/1/87 TO 5/31/89	14. DATE OF REPORT (Year, Month, Day) 1990, 1, 18	15. PAGE COUNT 156
16. SUPPLEMENTARY NOTATION			
17. COSATI CODES		18. SUBJECT TERMS (Continue on reverse if necessary and identify by block number) Nonlinear Elasticity, Temperature, PBT, Strong Fibers, Modulus, Laser-Generated Ultrasound, X-ray, Relaxation, Orientation, Stress, Crystal Modulus, Unit Cell, (con't)	
FIELD	GROUP	SUB-GROUP	
19. ABSTRACT (Continue on reverse if necessary and identify by block number)			
<p>In order to explore the nonlinear elasticity of high-performance PBZT fibers, a method using laser-generated ultrasound has been developed to measure the Young's modulus of the fibers as a function of temperature and static tensile stress. Up to 530°C and 1.7 GPa tensile stress, the nonlinear elasticity changes systematically with temperature, tensile stress and fiber processing conditions. There is a relaxation associated with a structural transition at about 300 - 400°C.</p> <p>X-ray diffraction has also been used to measure both the crystal modulus and aspects of the ultra-structure such as crystal size, unit cell structure and orientation. It is shown that improved crystal orientation with increased tensile stress is one of the most important mechanisms of the nonlinear elasticity. Measurements of orientation distribution are combined with other measurements to make calculations of the microscopic (con't)</p>			
20. DISTRIBUTION/AVAILABILITY OF ABSTRACT <input checked="" type="checkbox"/> UNCLASSIFIED/UNLIMITED <input type="checkbox"/> SAME AS RPT. <input type="checkbox"/> DTIC USERS		21. ABSTRACT SECURITY CLASSIFICATION Unclassified	
22a. NAME OF RESPONSIBLE INDIVIDUAL Dr. Donald R. Ulrich, Program Manager		22b. TELEPHONE (Include Area Code) (202)767-4963	22c. OFFICE SYMBOL NC

18. (con't)

Uniform Stress, Uniform Strain, Processing, Crystal Size



19. (con't)

modulus for the assumptions of uniform stress and uniform strain. The measured apparent crystal moduli are considerably greater than the measured ultrasonic ones. All are less than the theoretical values. The assumptions of uniform stress and uniform strain have also been used to calculate the macroscopic moduli. Both results exhibit less nonlinear elasticity than those observed experimentally. These phenomena are discussed in the context of the ultrastructure of the PBZT fibers.

AIR FORCE OFFICE OF SCIENTIFIC RESEARCH (AFSC)

BOLLING AIR FORCE BASE, WASHINGTON, D.C.

This document contains neither recommendations nor conclusions of the Air Force. It has been reviewed and is
approved for public release base IAW A.R. 190-12.

It is unclassified.

Approved for public release

Code: Technical Information Division

ULTRASTRUCTURE PROCESSING OF ORDERED POLYMERS

Ronald K. Eby
The Johns Hopkins University
Baltimore, MD 21218

1 January 1990

Final Report for Period 1 August 1987 - 31 May 1989

Prepared for

AIR FORCE OFFICE OF SCIENTIFIC RESEARCH
Building 410
Bolling AFB, DC 20332-6448

90 02 23 029

Approved for public release;
distribution unlimited.

TABLE OF CONTENTS

1 Introduction.....	1
 1.1 A Realizable Dream.....	1
 1.1.1 Extended Chain Flexible Polymer Fibers.....	3
 1.1.2 Liquid Crystalline Polymer Fibers.....	4
 1.2 The Molecular Composition and Processing of PBZT Fibers...9	
 1.3 The Properties of PBZT Fibers.....	10
 1.3.1 Tensile Properties.....	13
 1.3.2 Compressional Properties.....	15
 1.3.3 Thermal Properties.....	21



1.3.4 Chemical Properties.....	23
1.4 The Structure of PBZT Fibers.....	25
1.4.1 Crystallographic Structure.....	25
1.4.2 Longitudinal Organization and Lateral Order.....	29
1.4.3 Microvoids.....	35
2 Basic Concept of Anisotropic Elastic Behavior of Crystalline Polymers.....	39
2.1 Fundamentals.....	39
2.2 General Consideration.....	42
2.3 Different Approaches.....	48
2.3.1 Macroscopic Approach.....	48
2.3.2 Microscopic Approach.....	49
2.3.3 Molecular Approach.....	51

3 Characterization and Experimental Methods.....	55
 3.1 Laser Generated Ultrasonic Method.....	55
 3.1.1 Basic Principles of Laser Generated Ultrasound.....	56
 3.1.2 Experimental Method.....	64
 3.2 X-ray Diffraction Method.....	69
 3.2.1 Basic Principles of Wide Angle X-ray Diffraction of Polymers.....	70
 3.2.2 X-ray Modulus Measurements.....	73
 3.2.3 Determination of Crystalline Orientation Distribution.....	78
 3.2.4 Measurements of 2 Equatorial Scan.....	82
 3.2.5 Thermal Wide Angle X-ray Diffraction Measurements.....	88
 3.3 Sampling.....	88
4 Results and Discussion.....	90

4.1 Nonlinear Stress-Modulus Behavior at Room Temperature.....	90
4.2 Uniform Stress and Uniform Strain Models.....	96
4.2.1 Uniform Stress and Uniform Strain Assumptions for PBZT Crystals.....	96
4.2.2 Uniform Stress and Uniform Strain Assumptions for PBZT Fibers.....	111
4.3 Nonlinear Stress-Modulus Behavior at High Temperature....	121
5 Conclusions and Suggestions.....	137
References.....	141

Chapter One

Introduction

1.1 A Realizable Dream

In an ancient Chinese legend, about 5000 years ago, a goddess invented the use of natural materials to make textile for the benefit of her people. Until 100 years ago, people were still able only to use natural materials, such as cotton, silk and wool to produce filaments, fabrics and clothings. Since the beginning of this century, scientists and engineers started to make man-made fibers, first from regenerated cellulose, then from synthetic polymer consisting of chemical raw materials derived from oils and coal. Since then, some scientists have devoted themselves to exploiting and developing various polymeric fibers whose properties are superior to other materials, and they have an earnest desire to produce polymer fibers as strong as steel. Indeed, by means of theoretical calculations, it has long been recognized that the theoretical tensile modulus of a polymer chain should approach the modulus of steel. But until a decade ago, these theoretical approaches were considered unlikely to be achieved because all known polymers had moduli about two orders of magni-

tude lower. The explanation for the low modulus is that polymer chains fold and assume a random entangled and twisted configuration which has a lower load bearing capacity. Consequently, many scientists pointed out that the greatest strength would result from a structure of highly oriented, extended and densely packed chains. Now this dream has come true. Some polymers, for example Kevlar, PBZT and poly (*p*-phenylene benzobisoxazole) (PBO) have been processed into fibers which exhibit moduli greater than 200 GPa.

Strong motivation for the further exploration of high performance fibers comes from advanced industry. The aerospace business seeks polymer fibers with advantages of strength, stiffness, thermal stability, weather-resistance, weight-savings and economy. The high specific strength and modulus of such fibers have opened a new area for material science and engineering. Furthermore, a variety of other special features, such as radar-invisibility and mission-adaptive shapes, enhance their position as a class of materials with commercial importance[1-4].

Polymer researchers have pursued the problem of producing high-performance polymer fibers with well-aligned extended and closely packed chains by two basic approaches: (1) physically processing conventional flexible

chain polymers in such a way that a permanent deformation of the internal structure may occur; and (2) chemically designing rigid rod-like polymers by synthesizing polymers containing aromatic rings in the main backbone[1,5-10].

In this chapter we review the work and results of many others.

1.1.1 Extended Chain Flexible Polymer Fibers

Owing to the low rigidity, flexible-chain polymers are normally spun by freezing or spinning from nematic melts at high rates of shear, and superhigh drawing in solid states in order to produce strong fibers. Two typical examples are gel-spinning and solid-state extrusion of the flexible chain polymers[1,10].

Pennings first developed the gel spinning of very high molecular weight (HMW) polyethylene (PE)[11]. The spinning and ultra-drawing of the HMWPE crystallized gel lead to the ultimate high modulus fiber. Now several commercial products are used in textile and composites. However, a limitation for usage is the low melting point of PE[1^o].

Porter et al. have reported making extraordinary fibers by the solid state extrusion of many polymers[13]. A bulk polymer in the solid state is squeezed through a die under very high pressure to form fibers. Very high draw ratios

(up to 250 times) have been achieved. This produces extremely efficient conversion of the lamellar crystals into fibrillar crystals, with a measure of crystallinity of 96% in fibers and a modulus, 220 GPa. Unfortunately, it appears rather difficult to commercialize at present.

1.1.2 Liquid Crystalline Polymer Fibers

The fundamental principles which determine the tenacity, modulus and some other mechanical properties of fibers are as follows[1,10]:

- (1) mechanical properties, especially the tensile strength, are determined by the intramolecular forces of chemical bonds in the main chains of macromolecules and by the forces of various intermolecular interactions, such as hydrogen bonds, dispersion forces and Van der Waals forces;
- (2) orientation of macromolecules is an essential factor in the fiber failure mechanism;
- (3) extension of the macromolecules can make the ultimate strong fibers.

Based on these ideas, polymer scientists have synthesized a series of para-oriented aromatic polyamids possessing inherently rigid molecular chains

in an extended conformation. Such systems under certain conditions of concentration, solvent, molecular weight and temperature can form liquid crystalline solution to be wet- or dry-wet-spun to obtain high performance fibers[1,10,14,15]. The typical example, Kevlar fibers, poly (*para* phenylene terephthalamide) (*p*-PTA) (Fig. 1), a new generation of aramid fibers, exhibits high strength (3.5GPa), high modulus (130GPa) and high temperature resistance (Tab.1).

Encouraged by the success of Kevlar, polymer researchers at the Air Force Materials Laboratory, have been exploring the aromatic hetero cyclic polymers for high temperature applications[1]. These polymers, PBZT and PBO, exhibit even better thermal stability and environmental resistance, and offer double the modulus, higher strength and similar compressive properties, compared with Kevlar (Tab. 1 and Fig. 2). Furthermore, they have a potentially better properties, because of their comparatively high theoretical moduli. Although another commercial high performance fiber, carbon fiber, has a very high tensile modulus and strength, it is quite brittle which would limit its usage in many respects. It also has high electrical conductivity which influences its use too.

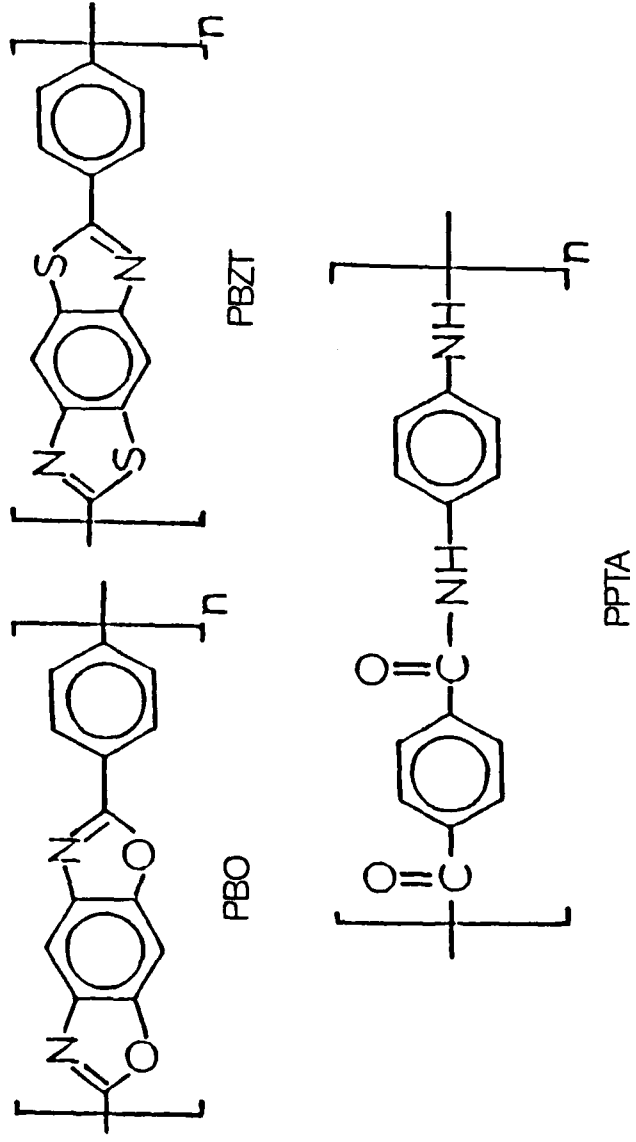


Fig. 1 Rigid rodlike macromolecules for high-performance fibers: *p*PTA, PBZT and PBO.

Table 1. Comparison of Properties of High-Performance Fibers

Material	Young's Modulus (GPa)	Tensile Strength (GPa)	Elongation to Break (%)	Density (g/cm ³)	Compressive Strength (MPa)	
Nylon (DuPont 728)	6	1.0	18.0	1.14	100	
Drawn PE	85	1.7	2.0	0.95	25	
Gel-spun PE (Spectra™ 1000)	170	3.0	1.7	0.97	70	
Solid-State-Extruded PE	220	5.0	2.3	0.99	-	
Thermotropic Polyester	80	2.6	3.2	1.4	200	
Kevlar™ 49	130	3.6	2.6	1.44	480	
Kevlar™ 149	185	3.5	2.0	1.47	450	
PBZT	330	4.2	1.3	1.58	400	
PBO	365	5.8	1.6	1.58	400	
Carbon P100	720	2.2	0.3	2.15	480	
Carbon T300	230	3.2	1.4	1.76	2880	
Carbon T50	390	2.4	0.6	1.81	1600	
Steel	200	4.2	2.1	7.8	-	
S Glass	80	4.5	4.5	2.4	>1000	
Boron	400	3.8	1.0	2.50	>5000	

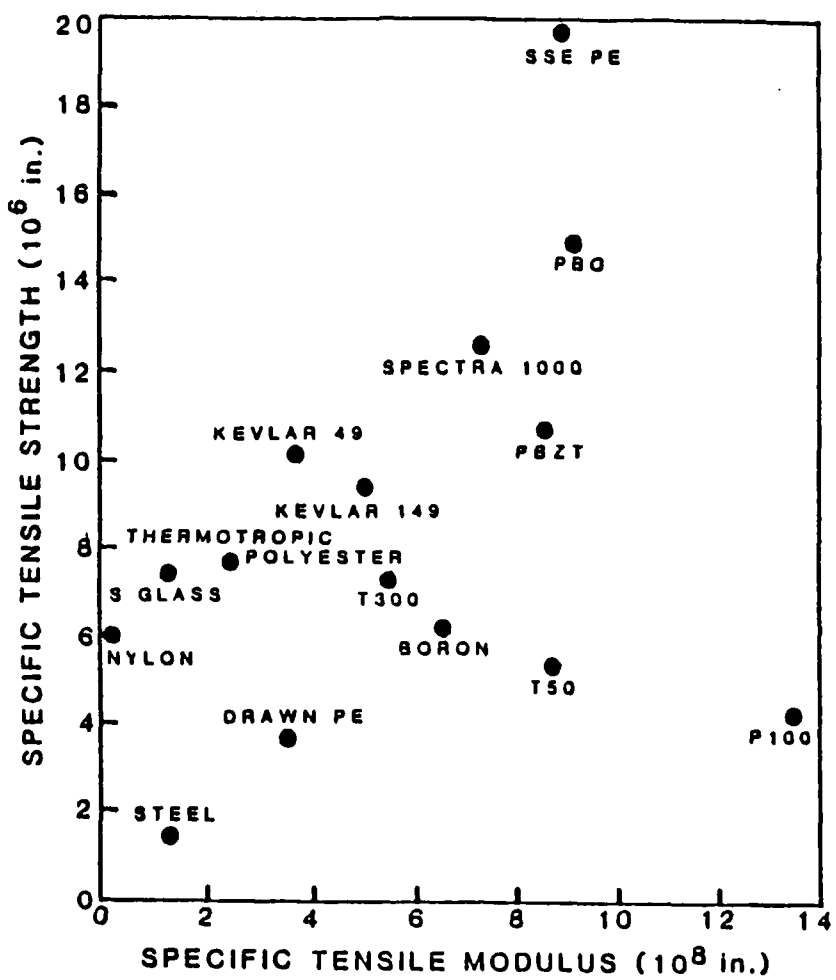


Fig.2 Plot of specific strength vs. specific modulus for a variety of fibers[1].

A notable research effort on PBZT system sponsored by the U. S. Air Force (Ordered Polymer Research Program) has achieved great success. The principal objective of their research work is, comparable to current commercial fibers, to develop new materials and possessing methodes.

1.2 The Molecular composition and Process of PBZT Fibers

In order to obtain high performance products, the PBZT precursor for spinning fibers must have a high molecular weight. The synthesis of the forming monomer of PBZT, 2,5-diamino-1,4-benzene dithiol dihydrochloride (DABDT), is divided into four steps[16-33]:

- (1) *p*-phenylenebisthiourea (BTU) preparation;
- (2) 2,6-diaminobenzobisthiazole (DABBT) preparation;
- (3) DABBT recrystallization; and
- (4) DABDT preparation.

Then DABDT is dehydrochlorinated in the medium of PPA and P_2O_5 . After adding in terephthalic acid (TPA) and P_2O_5 , the polymerization begins while stirring for 48 hrs. At last the products consisting of 83% P_2O_5 and

15% PBZT are obtained. The chemical reaction is shown in Fig. 3.

Normally the molecular weight (M_n) of PBZT products is about 10,000.

The compounds of the PBZT system are only soluble in strong acids such as methane sulfonic acid (MSA), chlorosulfonic acid (CSA) and poly (phosphoric acid) (PPA). Two types of spinning dopes, PBZT/MSA and PBZT/PPA systems, are commonly chosen to form either an anisotropic or a unoriented nematic spinning solution. The dopes are prepared by dissolving about 5-10% PBZT polymers into the above strong acids. The dry-jet-wet spinning method is selected to make fibers, as shown in Fig. 4. The coagulation bath contains H_2O . Heat treatment for small-scale production is accomplished by drawing through an oven.

1.3 Properties of PBZT Fibers

1.3.1 Tensile Properties

As indicated above, PBZT system fibers have outstanding tensile behavior. For the as-spun fibers, the modulus is about 100 GPa and strength 1 GPa; for heat-treated (HT) fibers the modulus reaches as high as 300 GPa

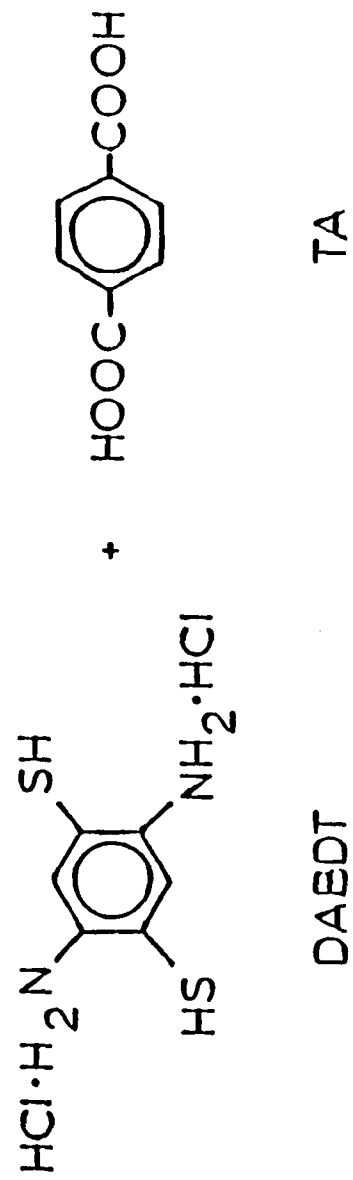


Fig.3 The scheme of the synthesis procedure of PBZT.

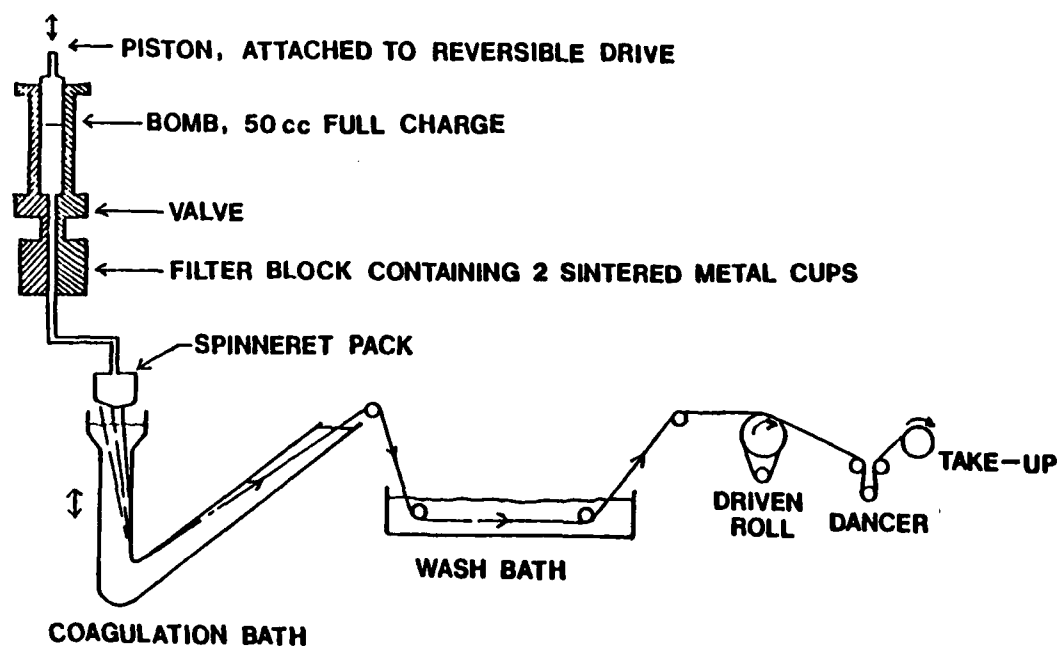


Fig.4 Schematic diagram of the spinning processing of PBZT fibers.

and strength around 2.6 GPa[1,5,15]. These values are much better than most of the commercial high performance fibers, which clearly shows the potential advantages of PBZT system fibers in composites for use in aerospace. The stress-strain (S-S) characteristics of PBZT are shown in Tab.1 and Figs. 5 and 6.

The earlier work disclosed that the tensile S-S curve of PBZT as-spun fibers exhibits elastic-plastic behavior with strain hardening. A high modulus is exhibited in the initial linear region followed by a region of limited plastic deformation (1-3%) (Fig. 5). Furthermore, the modulus of elasticity increases with reextension after initial plastic deformation. The relative amount of increase in modulus of a work hardened fiber with plastic deformation is in the range of 0-100%, depending on processing and history[15,34-38].

The tensioned heat treatment considerably enhances the modulus and strength of PBZT fibers. Different heat treatment temperatures and stresses would lead to different fibers. Fig. 6 shows several stress-strain curves of the PBZT film at various temperatures. The S-S curves exhibit a departure from linear elastic behavior, which was considered to be caused by irregularities and internal stresses introduced during processing[36]. The plasticizing effect

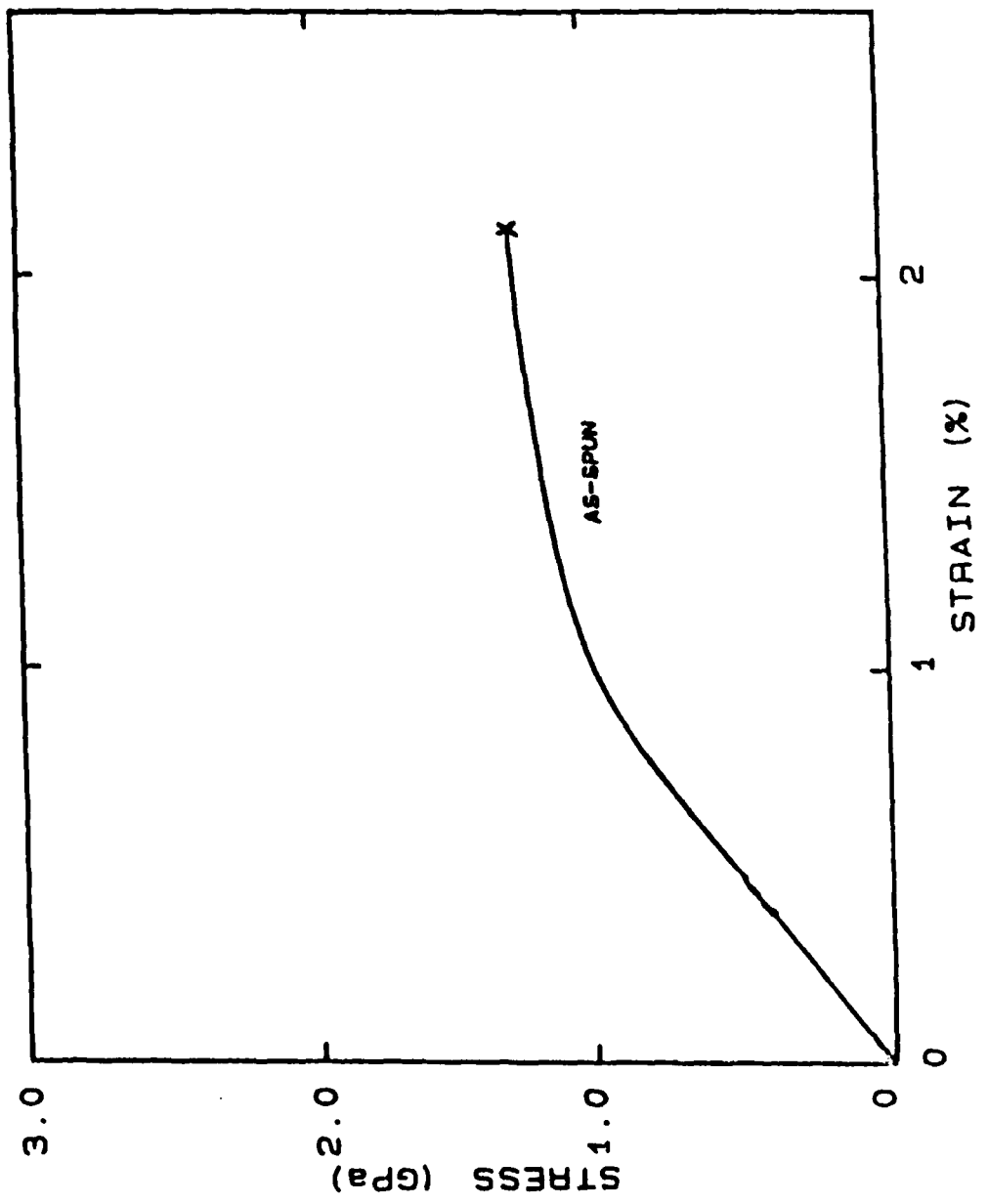


Fig.5 The tensile behavior of as-spun PBZT fibers[15].

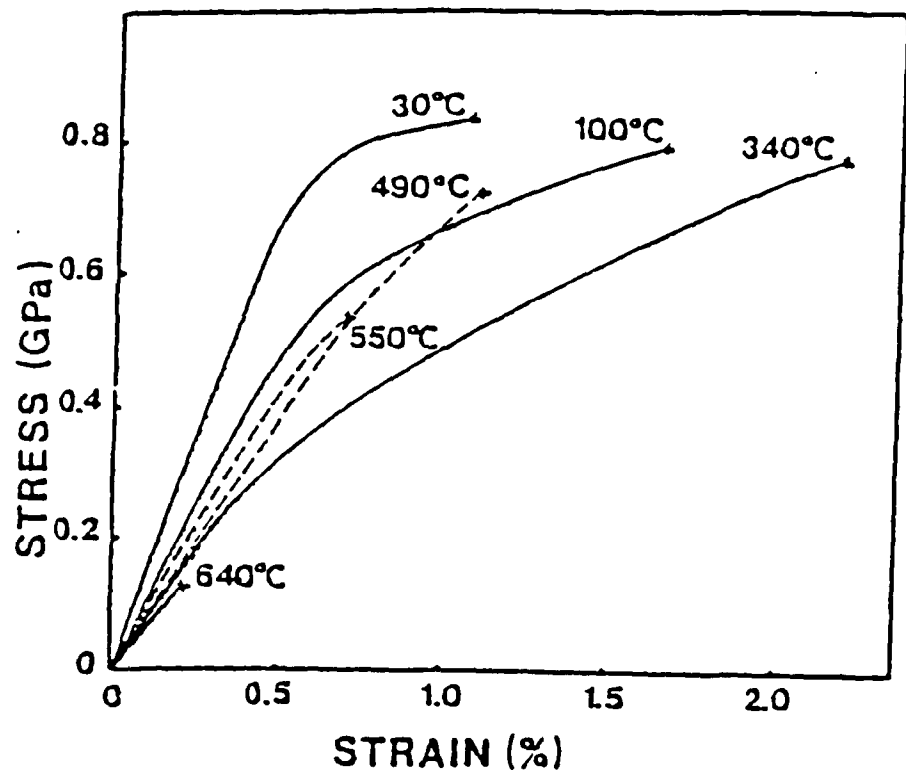


Fig.6 Stress-strain curves at various temperatures for PBZT film[48].

of any residual solvent also has to be taken into account[38]. Consequently, it is very interesting that the research on PBZT fibers by means of the laser-generated ultrasonic method has disclosed that there is a clear nonlinear elasticity behavior for PBZT fibers, which has a great significance for making composite materials. The correlation among stress, temperature, modulus and structure of the PBZT fibers will be discussed in more detail in Chapter 4.

1.3.2 Compressional Properties

Until now the impressive technical achievement of making polymer fibers with superior tensile properties must be tempered to some degree by their relatively modest mechanical performance laterally. This phenomenon could be attributed to the inherently weak transverse interaction between the polymer chains.

The compressive properties of PBZT fibers are a little worse than Kevlar (Fig. 7)[15]. But the improved PBZT (680 MPa) is almost the same as Kevlar (740 MPa)[15,39,40].

Commonly, from the experience of Kevlar, some people think that the onset of plastic deformation for PBZT fiber system during compression may

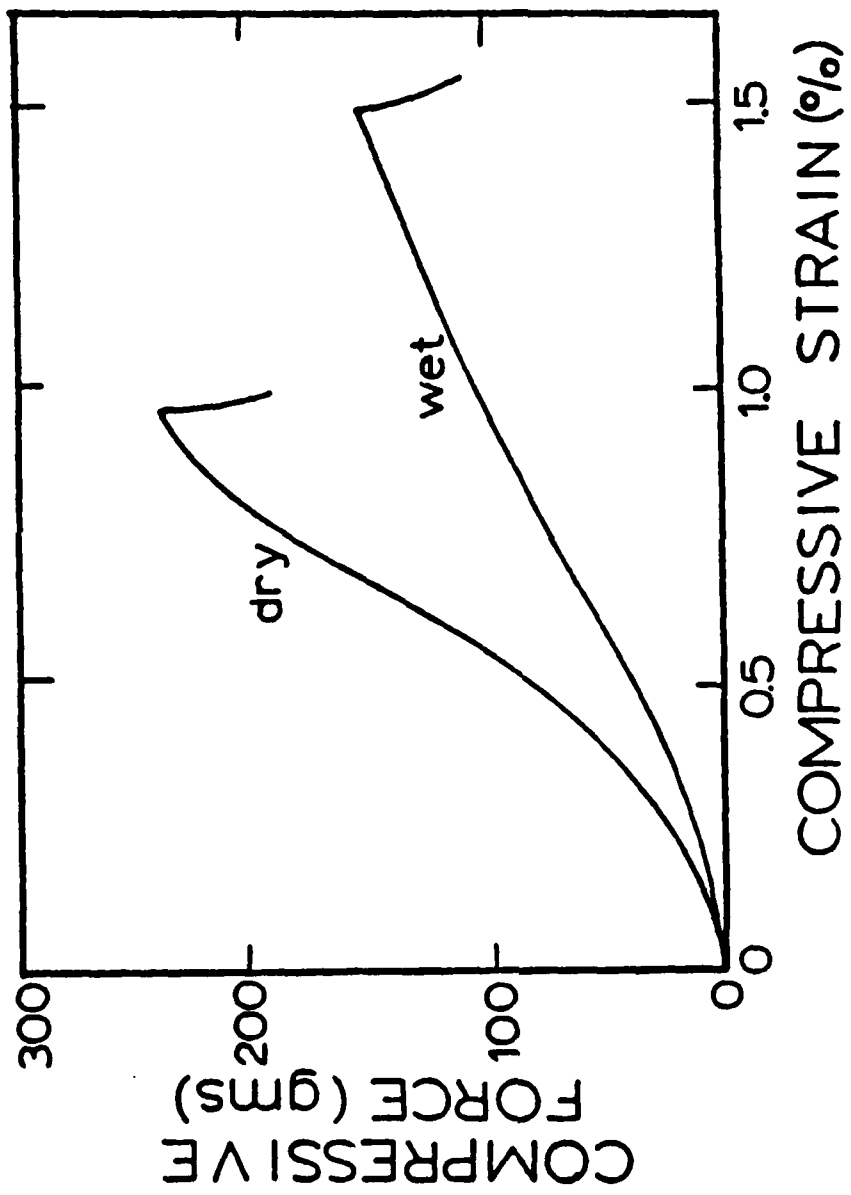


Fig.7 Compressive force-strain behavior for hollow wet vs. dry
PBZT fibers[15].

arise from shearing of the molecular chains and lead subsequently to the formation of oblique kink bands within the fibers[41-47].

The kink bands on the surface of the PBZT fiber initiate as thin bands oriented at about 70° to the fiber axis. The arrow C, in Fig. 8, points to an incipient band[47]. At higher level of compressive strain, the bands propagate across the fiber diameter and eventually form the thick bulging perpendicular to deformation bands seen in Figs. 8-11[47]. These large bands form periodically along the fiber length. Owing to the shear failure occurring in the most poorly aligned regions, we may expect that the fibers with high average orientation should have high compressive strengths. However the compressive strength of PBZT is relatively insensitive to improvement in average axial orientation by tension-heat-treatment. Therefore, it is unlikely that shear failure initiates compressive kink band formation in PBZT fiber system. The residual stress generated by drying PBZT fibers may be the cause of compressive buckling observed in the dried fibers. Regions of a fiber that are under residual compression will reach critical buckling stress first. Therefore, premature nucleation of kink bands could occur in such regions.

Fig.8 Electron micrograph showing the bended structure of PBZT[47].

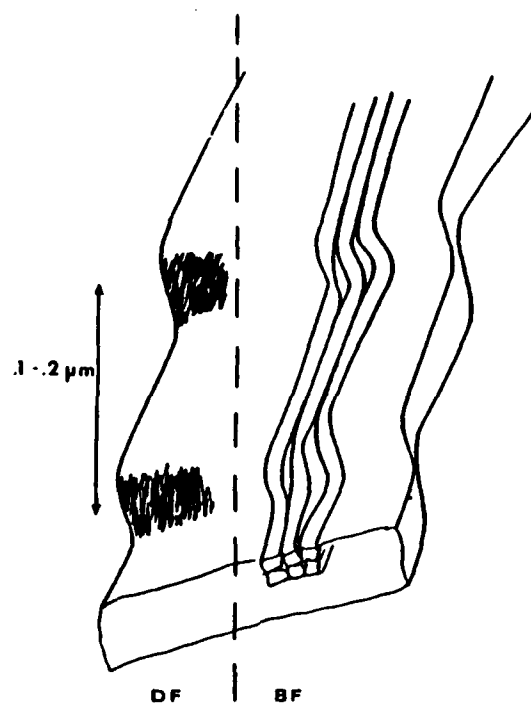


Fig.9 Schematic diagram of the fibrillar structure of the ribbonlike fragments obtained after peeling and mold sonication of PBZT fibers[47].

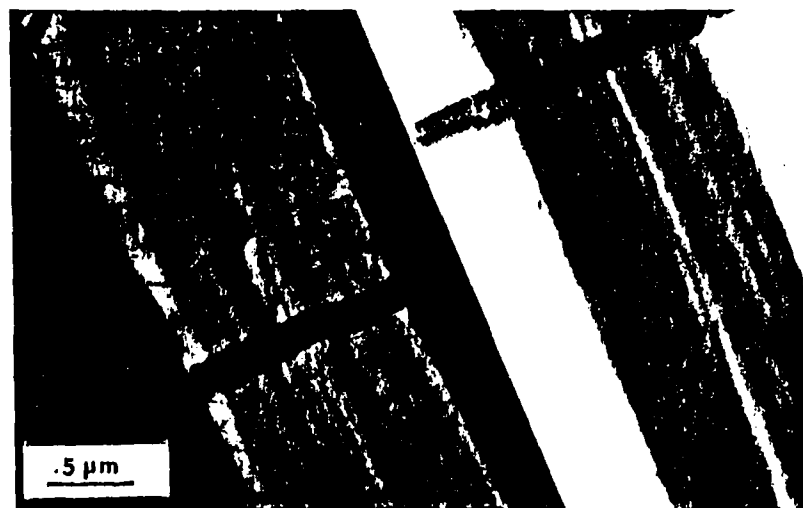


Fig.10 Bright field (BF) (right) and dark field (DF) (left) images of a fragment of a PBZT fiber showing the band structure which appears in DF[47].

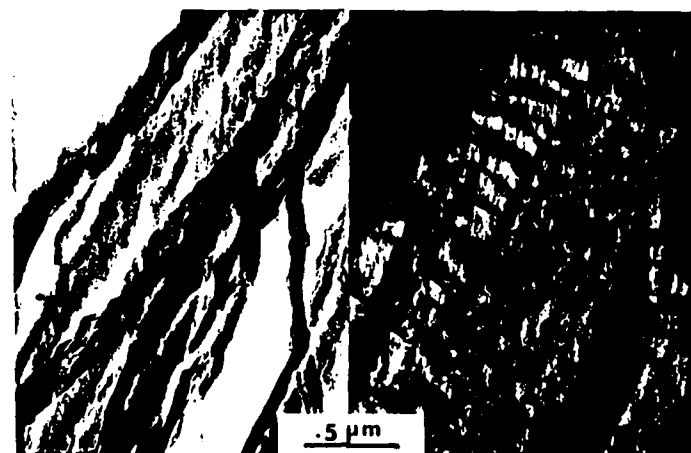


Fig.11 BF (left) and DF (right) images of ribbonlike fragments of a PBZT fiber showing the fibrillar texture of the ribbons[47].

1.3.3 Thermal Properties

As described before, heat treatment of PBZT as-spun fiber produces a highly significant improvement in mechanical and other properties. The HT-PBZT fibers exhibit outstanding thermal stability, compared to most polymer fibers, even Kevlar. They do not melt and only decompose in air at temperatures above 700°C, which is much better than Kevlar (decomposition at about 500°C). Of course, these numbers depend upon the duration, the rate of processing and the situation of the temperature measurements.

The high dimensional stability of PBZT fibers at elevated temperature is also an important feature for many engineering applications. The calculated thermal expansion coefficient for HT-PBZT is approximately $-1.0 \times 10^{-6} / ^\circ\text{C}$, which is better than that of Kevlar, $-3.0 \times 10^{-6} / ^\circ\text{C}$ [39].

The force-temperature (F-T) behavior of the HT-PBZT fibers is shown in Fig. 12[15]. Apparently, PBZT is superior to Kevlar 49 in heat resistance. For the effect of temperature on S-S curves, the decreasing rate of the S-S curve is greater for Kevlar than for PBZT. At 200°C, the HT-PBZT retains 73% of its original strength while Kevlar retains only 60-65%. Fig. 13 is the temperature dependence of fiber tensile strength[15]. Due to the negative

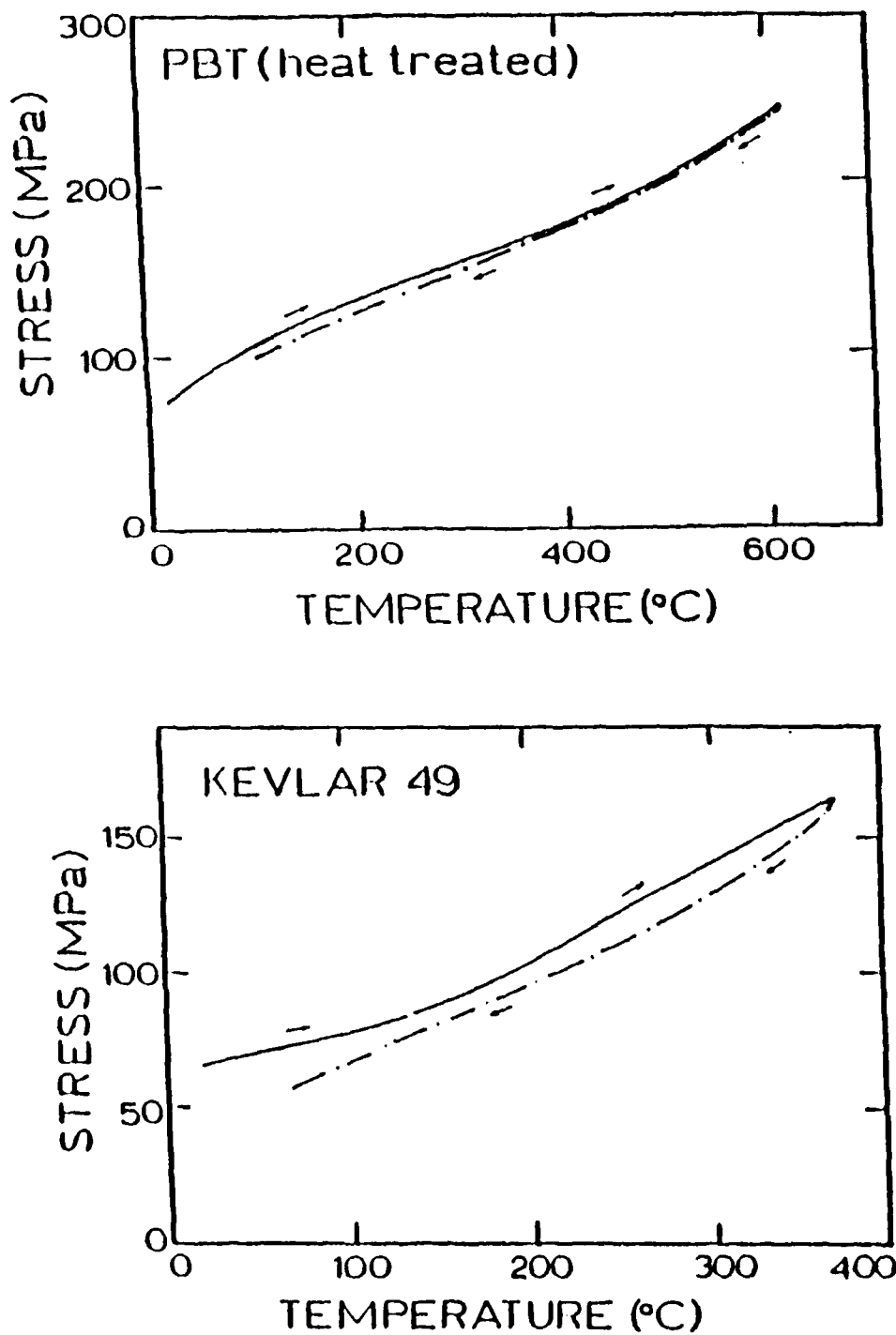


Fig.12 Stress-temperature profiles for tension heat treated PBZT and Kevlar 49 fibers[41].

coefficient of thermal expansion to the PBZT fiber axis, the properties of the composites made of these kinds of fibers would change when they are subjected to wide variations in temperature. For PBZT fibers, the interesting results in the relationships of stress, modulus and temperature, which deviate from linear elasticity, will be discussed in detail in Chapter 4.

1.3.4 Chemical Resistance

PBZT fibers, due to their highly ordered aromatic structures, are generally extremely resistant to chemical attack except by strong acids at high concentrations or elevated temperatures. For example, the as-spun PBZT fiber, after 200 hours exposure to chloroform, dimethyl acetamide, acetone, and water, keeps essentially both its modulus and strength unchanged. The same modulus retention was also observed after 3700 hours exposure in dimethyl acetamide and water environments with a 67% retention of strength. This high corrosion resistance is a highly desirable characteristic in engineering applications[15,39-44].

However, strong acids hurt the fiber mechanical properties. After 200 exposure hours in nitric acid both modulus and tenacity of PBZT fibers

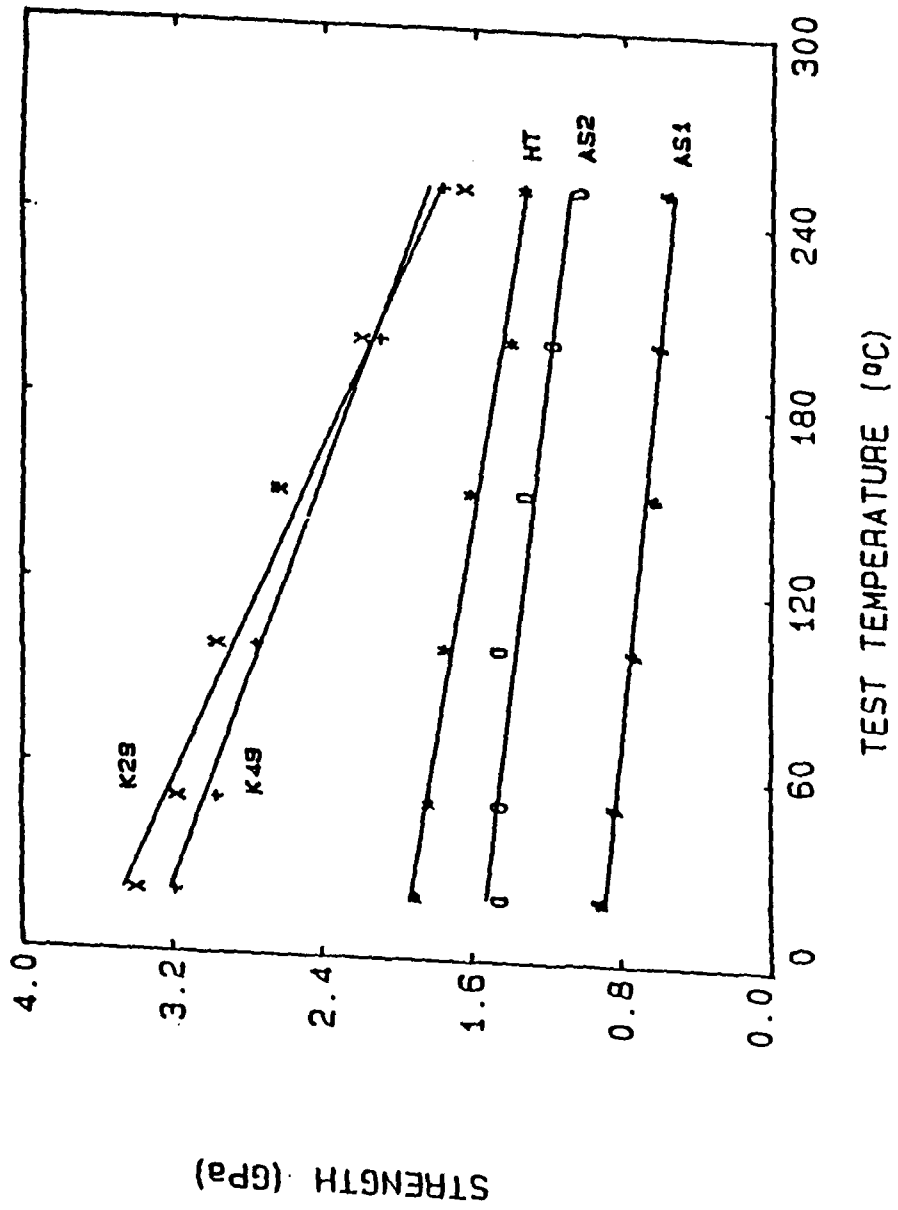


Fig.13 Temperature dependence of the tensile strength of as-spun and HT PBZT, and Kevlar 49 fibers[15].

reduced about 50%, while in sulfic acid the reduction was 80-85%[15,39-44].

1.4 Structure of PBZT Fibers

Obviously the properties of a material depend on its composition and structure. In the case of the PBZT fiber system we now have considerable information available. This information will play a role if we are going to exploit the composition of structure in more detail.

1.4.1 Crystallographic Structure

Studies of wide angle x-ray diffraction (WAXD) and selected area electron diffraction (SAED) on PBZT fibers have also shown that the linear molecules align perfectly along the fiber axis direction and possess a very high degree of axial orientation[30,45-49]. There is no apparent evidence for small angle two or four point meridional reflection which is traditionally associated with chain folding in polyamide and polyester fibers. Such an observation supports further the existance of an extended chain conformation. In the fiber direction there exists no definite order, namely, no three-dimensional crystal-

line order has been found. So, it is assumed that PBT is a single phase crystalline material, with a monoclinic crystal unit cell structure[50-55]. Different authors gave different structures:

Roche's model[47],

$$a = 0.597 \text{ nm} \quad \gamma = 95.2^\circ$$

$$b = 0.362 \text{ nm} \quad \rho = 1.65 \text{ g/cm}^3$$

$$c = 1.254 \text{ nm} \quad Z = 1$$

Odell's model I[46],

$$a = 0.655 \text{ nm} \quad \gamma = 116.4^\circ$$

$$b = 0.356 \text{ nm} \quad \rho = 1.713 \text{ g/cm}^3$$

$$c = 1.235 \text{ nm} \quad Z = 1$$

Odell's model II[46],

$$a = 1.196 \text{ nm} \quad \gamma = 100.9^\circ$$

$$b = 0.356 \text{ nm} \quad \rho = 1.713 \text{ g/cm}^3$$

$$c = 1.235 \text{ nm} \quad Z = 2$$

Odell's model III[46],

$a = 1.196 \text{ nm}$ $\gamma = 102.1^\circ$

$b = 0.352 \text{ nm}$

$c = 1.251 \text{ nm}$

Fratini's model[56],

$a = 1.223 \text{ nm}$ $\gamma = 106.3^\circ$

$b = 0.365 \text{ nm}$

$c = 1.251 \text{ nm}$

Heat-treatment would greatly improve the regularity of the crystal structure of PBZT and lead to denser and more perfect crystals. Fig. 14 is the suggested packing arrangement of PBZT molecules and basal projection of the crystal unit cell[15].

1.4.2 Longitudinal Organisation and Lateral Order

The longitudinal section of PBZT fibers does not exhibit a distinctive periodic organization, as we discussed before, but there is an ordered crystalline material, crystallite, throughout the fiber, which is composed of microfibrils and fibrils. The small crystallites are regularly disoriented

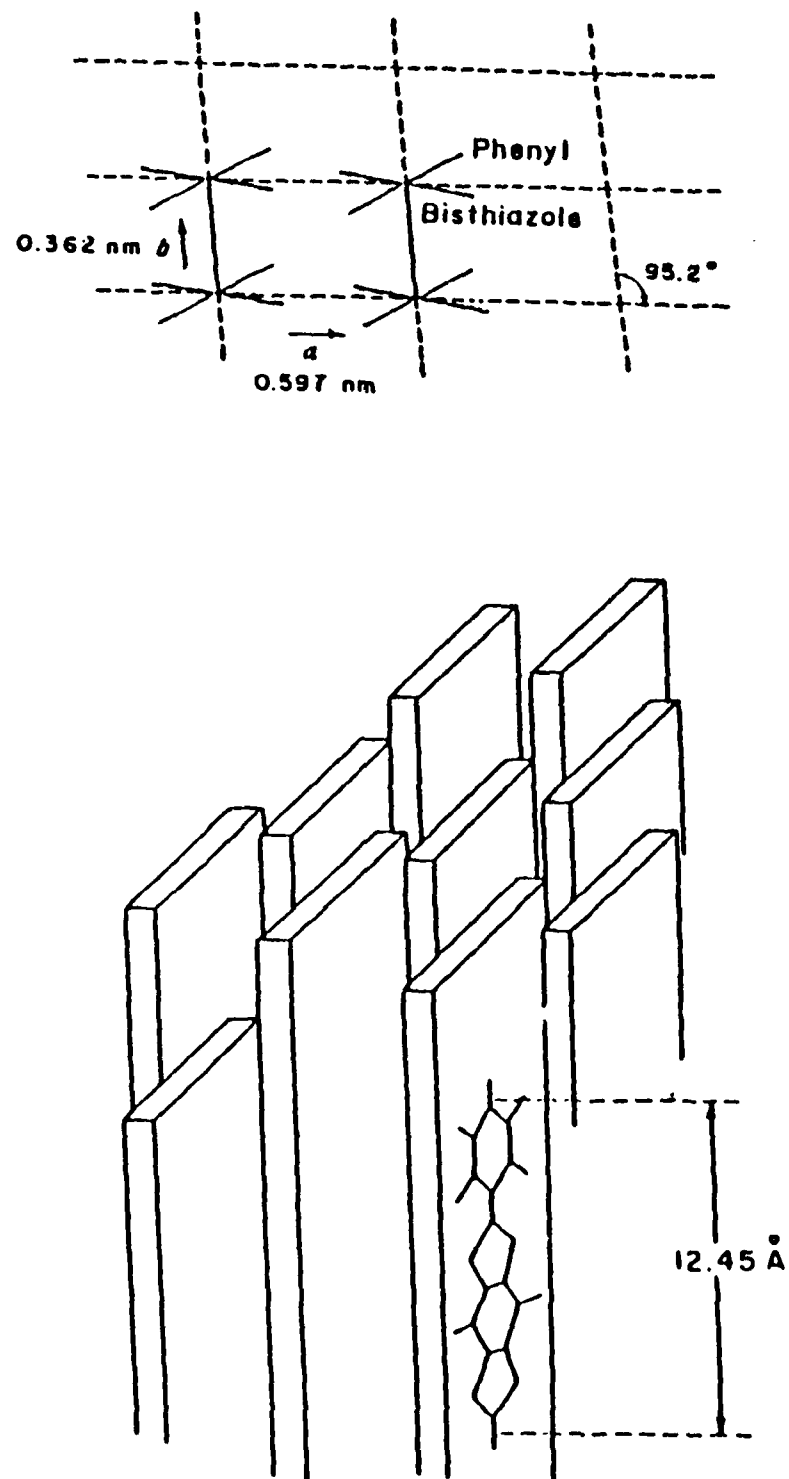


Fig.14 Schematic diagram of the crystal unit cell structure of PBZT[15].

throughout the fragment of fibrils. From dark-field electron microscope observations, the strongest diffracting crystallites are elongated in shape with their average length being about 5 times larger than their width, which ranges from approximately 60 to 80 Å. Owing to γ being close to a right angle, the ratio of L_{100}/L_{010} was used to evaluate the cross-section of an average PBZT "crystallite", where L is the lateral coherence size calculated from WAXS. The cross-section is approximately rectangular with a ratio of side lengths of roughly 1:1.5. Fibers with different history would have different sizes of supermolecular structures. An estimation of the number of molecular chains comprising the lateral coherence size is as follows: for as-spun fibers, the average is about 20 chains, and for HT fibers (treated above 600°C), the average is about 400 chains. The local extent of the lateral molecular order (based on (100) crystal profile) is roughly 2 nm for as-spun fibers, roughly 8 nm for HT fibers treated at 450°C and 10 to 12 nm for HT fibers treated at 600°C[36,42-48].

By means of electron microscopy, thinner ribbonlike fibrils are observable. Each of these flat ribbons appears to consist of smaller "microfibrils" of lateral dimension varying from 50-80 Å, as described before(Figs. 15 and 16). These ribbons exhibit a wavy texture, each microfibril changing its direction

in relation to its neighbors. According to Roche's observation, the crystalite size is around 40×150 Å or below. The long direction of the crystallites makes a slight angle ($10 - 20^\circ$) with the fiber direction, similar to that made by the microfibrils[36].

It could be concluded now that in PBZT fibers, there are textured ordered ribbons, fibrils present all along the length of fibers, with neighboring crystallites in approximately the same orientation within a band. A schematic diagram of the texture of these kinked ribbons is proposed in Figs. 8-11[47]. The ribbon is built up of closely packed microfibrils. Each microfibril consists of a succession of narrow crystallites embedded in a somewhat less ordered matrix. The bands also reflect the susceptibility of the fibrils to transverse kinking or buckling (Fig. 17)[42].

Furthermore, because of the translational freedom allowed by the absence of hydrogen bonding and the finite lengths of a PBZT molecule or a fibril in a PBZT fiber, tensile stresses in the fibrils are transferred through shear interactions which are directly dependent on the nature of the intermolecular forces. Therefore the lateral or shear stresses present in fibrillar and microfibrillar boundaries are important in determining fracture. Owing to the



Fig.15 Comparison of surface undulations and interior fibrillar alignments in (a) as-spun, and (b) tension heat treated PBZT fibers[36].

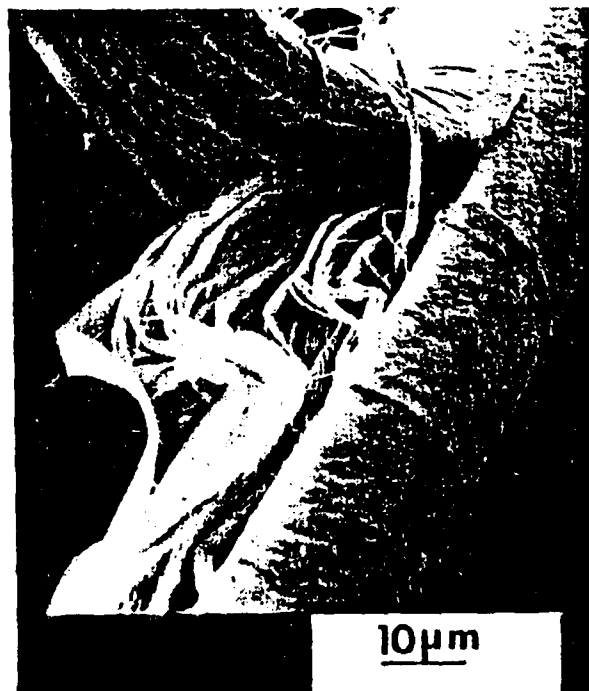


Fig.16 SEM micrograph of a partially peeled PBZT fibers[47].

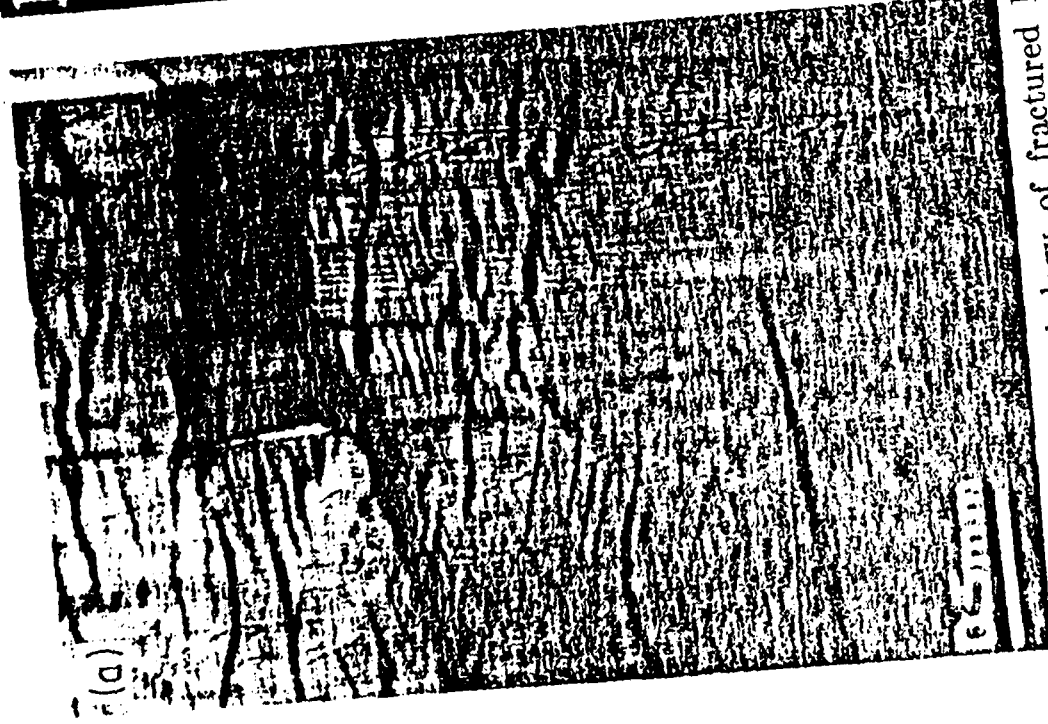
preferred orientation influencing the shear stress, the tensile properties would be sensitive to the preferred orientation of molecules. The tension used during the heat treatment also influences the fiber orientation. The applied tension during heat treatment results in an increase in overall molecular orientation, which leads to higher tensile modulus and tenacity. So the tension heat-treatment increases both the longitudinal and lateral orders, namely the overall axial molecular orientation and the extent as well as perfection of lateral molecular order[15,40-42].

For as-spun fibers, the existence of a wavy or wrinkled fibrillar morphology of varying severity (Figs. 15 & 17) indicates that the longitudinal structure is an initial non-uniform fibrillar organization. Then, tension heat-treatment makes the structure be highly oriented in the fiber direction with a more uniform fiber appearance. Hence, the tension heat-treatment perfects not only the molecular organization, but the overall fibrillar morphology[15,40-42,48].

1.4.3 Microvoids



(a)



(b)

Morphology of fractured PBZT fibers: (a) optical micrograph
Fig.17 Morphology of fractured PBZT fibers: (a) optical micrograph showing band; (b) SEM micrograph showing transverse band; (b) SEM micrograph showing transverse bands and axial splitting[42].

One of the important characteristics of PBZT fibers, similar to many other wet-spun fibers, is the exhibition of a diffuse, continuous distribution of intensities of Small Angle X-ray Scattering (SAXS). This diffuse scattering is caused by the presence of microvoids generally 10 nm or less in size. By means of electron microscopy, it is observed that void "tails" extend from the central region of a macrovoid (Fig. 18)[42]. The void extends in length the distance of a few fiber diameters but with a narrower cross-section. The average concentration of voids is between 2 and 5 voids per mm. Such a feature has an adverse effect on the potential mechanical properties. Because these voids can occupy about 10-15% of the load bearing cross-section of the fiber, the observed values of modulus are crudely 91-99% of the void free fiber modulus. The presence of voids will, however, have a slightly greater effect on the observed value of tensile strength. It is expected that during a tensile test, the failure would be initiated in the fiber segment possessing the largest microvoid because of the effective reduction in loading bearing area and the stress concentration. The measured fiber strengths are roughly 85-90% of a void free fiber strength. Examination of fracture ends of tensile tested PBZT fibers reveals that the failures are in fact initiated at voids (Fig. 18). The elliptically shaped region in the picture shows that the macrovoids region is the location

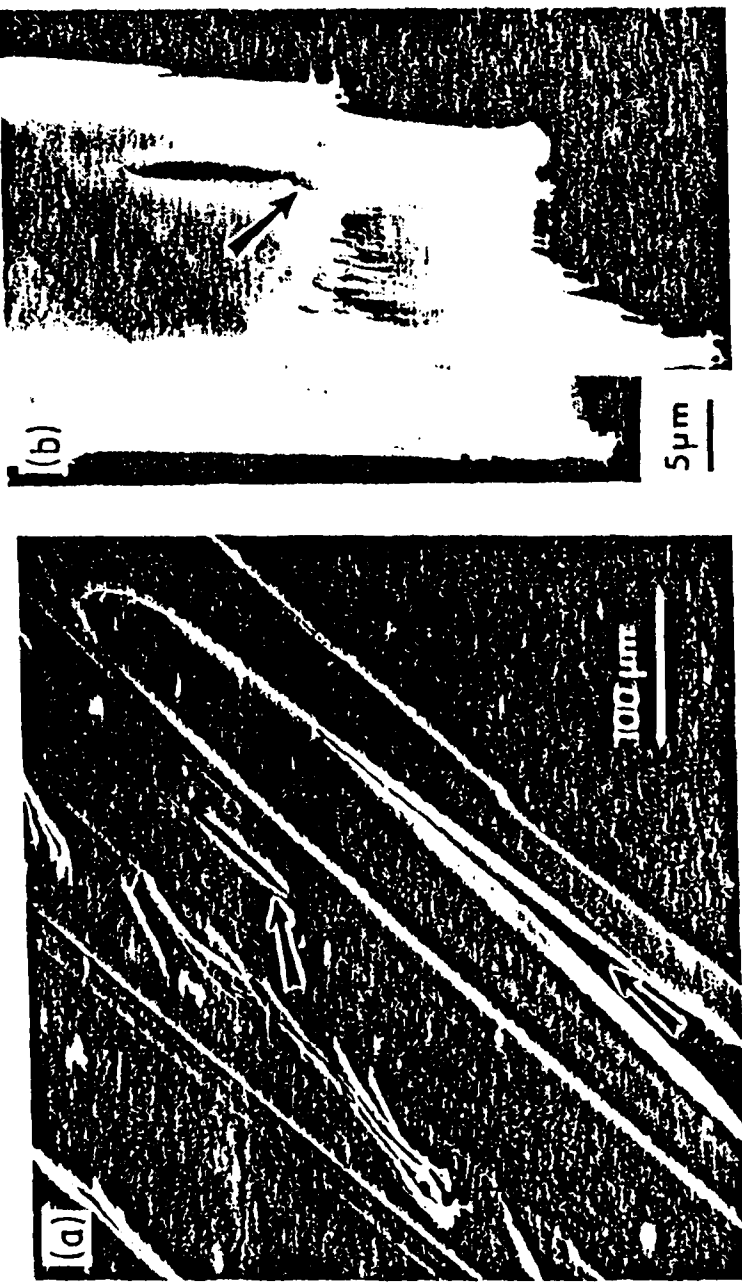


Fig.18 SEM micrographs of PBZT films: (a) low magnification micrograph of film surface; (b) high magnification of tensile fracture. Arrows point to voids[42].

at which the fracture occurs[15,39,57-62].

Since the scattered intensity of HT fiber bundles is greater than that of as-spun fiber with similar thickness, this indicates that fibrillation increases the number of voids. However the improved lateral packing in the HT-fiber results in fewer large microvoids, that is, the fibrils fill in some of the larger voids[15,57-62].

The fibrillar morphology and elongated axial shape of the voids indicate that the voids do not act as strong stress concentrators in the manner normally associated with holes and cracks. The fibrillar structure itself would serve to cause crack defects provided the interfibrillar forces are less than one-fifth of the axial fibril cohesion. So, although the voids will tend to reduce the potential lateral and longitudinal strengths, the effective reduction in cross-section area resulting from the presence of microvoids will have a relatively small effect on the tensile properties compared with the existance of the long macrocracks lying at small angles to fiber axis. Propagation of these central cracks should facilitate fracture over extensive lengths to the weak outer layers of the fiber.

From above review, it is evident that PBZT system has excellent tensile

mechanical properties, significantly high thermal stability and great environmental resistance. Hence, since shortly after the first preparation of PBZT in 1977, the system has become a leading candidate for the development of high performance fibers.

Chapter Two

Basic Concept of Anisotropic Elastic Behavior of Crystalline Polymers

2.1 Introduction

Unlike traditional materials of construction, the mechanical properties of polymers: (1) are strongly dependent upon processing history, (2) may undergo dramatic changes at various temperatures, and (3) are sensitive to the duration of an applied load. Such variability in the mechanical properties is utilized and interpreted from three different points of view[63-65].

Structural engineers are primarily interested in using characteristic mechanical property data to predict load-deformation response, and time-temperature stability. In this use, a polymeric material is viewed as a homogeneous macroscopic continuum and the well-known techniques of elasticity theory are used to predict performance. This approach treats the observed mechanical properties as the fundamental material descriptors. Consequently, the sensitivity of the mechanical properties to processing history presents a major problem to the practitioners of this approach[65].

On the other hand, material engineers, who do not view such variability in properties as a problem that detracts from the serviceability of polymeric materials, tend to emphasize the potential for tailoring polymeric materials to specific applications. In order to understand the necessity for exercising properties control, the polymeric material is treated as a heterogeneous mixture of microscopically distinct components. Each microscopic phase component is considered as a homogeneous and generally anisotropic continuum. In this view, the mechanical properties of the individual phase components assume the role of the fundamental material descriptors. Accordingly, a knowledge of (1) the properties of each phase, (2) the mechanism of phase coupling and (3) the internal distributions of the load-deformation field is sufficient, in principle, to predict the macroscopic properties. Since the phase properties are frequently inaccessible to direct evaluation, they are treated as adjustable parameters in models based on mechanical analogs. The practitioners of this idea tend to treat the properties of the phase components as invariant with respect to processing and attempt to establish empirical correlations between the observed mechanical properties and processing conditions through the influences of changes in spatial organization of the phase components[65].

At the submicroscopic level, materials scientists direct attention to relating chemical composition, molecular structure and supermolecular organization to the behavior of the microscopic phase components. At this level of abstraction, the phase properties are described in terms of intra- and intermolecular force fields. The characteristic parameters of the molecular structures and the force fields assumed the role of the fundamental meterals descriptors[65].

It is obvious that a synthesis of all three approaches is essential to the understanding and optimum utilization of polymeric materials. The molecular approach offers the potential for relating molecular composition and structure to the phase properties, and hence serves as the link between the chemistry and physics of materials. The microscopic approach provides techniques for relating phase properties to bulk properties and thereby provides the connection between the molecular theory of matter and the engineering applications. The macroscopic approach contains the means of relating materials properties to performances. Collectively these approaches provide a methodology for developing guidelines to design of molecular systems for optimum materials performance[65].

2.2 General Consideration

Before proceeding with the details of the macroscopic, microscopic and molecular approaches, it would be useful to summarize briefly the basic notions underlying the description of the mechanical behavior of materials. The ability of a material to transfer force to deformation (and vice versa) is the principal descriptor used to characterize the mechanical behavior of materials.

The most general linear relationship between stress and strain is obtained by assuming that each of the components of stress tensor σ is linearly related to all the components of strain tensor ϵ and vice versa. Thus

$$\sigma_{xx} = a\epsilon_{xx} + b\epsilon_{yy} + c\epsilon_{zz} + d\epsilon_{xz} + \dots \quad (2-1)$$

and

$$\epsilon_{xx} = a'\sigma_{xx} + b'\sigma_{yy} + c'\sigma_{zz} + d'\sigma_{xz} + \dots \quad (2-2)$$

where x,y,z are Cartesian coordinate axes, a,b,...,a',b',..., are constants. This is the so-called generalized Hooke's law.

In tensor notation the second-rank tensor σ_{ij} is related to the second-rank strain tensor ϵ_{ij} by fourth-rank tensors C_{ijkl} and S_{ijkl} . Thus

$$\sigma_{ij} = C_{ijkl} \epsilon_{kl} \quad (2-3)$$

or equivalently

$$\epsilon_{ij} = S_{ijkl} \sigma_{kl} \quad (2-4)$$

where $\sigma_{ij} = \sigma_{xx}, \sigma_{yy}, \epsilon_{yy}, \dots$, etc.

The fourth-rank tensor S_{ijkl} and C_{ijkl} contain the compliance and stiffness constants respectively, with i, j, k, l taking values 1, 2, 3 and the stresses and strains in terms of x, y, z .

It is customary to adopt an abbreviated nomenclature in which the generalized Hooke's law relates the six independent components of stress to the six independent components of the engineering strains. Thus

$$\sigma_p = C_{pq} \epsilon_q \quad (2-5)$$

and

$$\epsilon_p = S_{pq} \sigma_q \quad (2-6)$$

where σ_p represents $\sigma_{xx}, \sigma_{yy}, \sigma_{zz}, \sigma_{xz}, \sigma_{yz}, \sigma_{xy}$, and ϵ_p represents $\epsilon_{xx}, \epsilon_{yy}, \epsilon_{zz}, \epsilon_{xz}, \epsilon_{yz}, \epsilon_{xy}$. In the matrices of C_{pq} and S_{pq} , p and q take values 1, 2, ..., 6. In the case of the stiffness constants the values of p and q are obtained in terms of i, j, k, l by substituting 1 for 11, 2 for 22, 3 for 33, 4 for 23, 5 for 13 and 6 for 12. For the compliance constants rather more complicated rules apply owing to the occurrence of the factor-2 difference between the definition of the

tensor shear strain components and the definition of engineering shear strains.

Thus

$$\begin{aligned} S_{ijkl} &= S_{pq} \quad \text{when } p \text{ and } q \text{ are 1, 2 or 3,} \\ 2S_{ijkl} &= S_{pq} \quad \text{when either } p \text{ or } q \text{ are 4, 5 or 6,} \\ 4S_{ijkl} &= S_{pq} \quad \text{when both } p \text{ and } q \text{ are 4, 5 or 6.} \end{aligned} \tag{2-7}$$

The existence of a strain-energy function provides the relationships

$$C_{pq} = C_{qp} \tag{2-8}$$

and

$$S_{pq} = S_{qp} \tag{2-9}$$

and reduces the number of independent constants from 36 to 21. Thus

$$\left[\begin{array}{cccccc} c_{11} & c_{12} & c_{13} & c_{14} & c_{15} & c_{16} \\ c_{12} & c_{22} & c_{23} & c_{24} & c_{25} & c_{26} \\ c_{13} & c_{23} & c_{33} & c_{34} & c_{35} & c_{36} \\ c_{14} & c_{24} & c_{34} & c_{44} & c_{45} & c_{46} \\ c_{15} & c_{25} & c_{35} & c_{45} & c_{55} & c_{56} \\ c_{16} & c_{26} & c_{36} & c_{46} & c_{56} & c_{66} \end{array} \right] \tag{2-10}$$

The S matrix is similar to the C matrix. These matrices define the relationships between stress and strain in a general elastic solid, whose properties vary with direction, i. e. an anisotropic elastic solid.

Since the material has not been modified by the choice of coordinate axes, the stiffnesses C'_{ijkl} (or compliances) under new reference axes must be

related to the stiffnesses C_{ijkl} . It has been demonstrated that the apparent descriptors C'_{ijkl} referenced with respect to an arbitrary orthogonal axes system $(\vec{a}_1, \vec{a}_2, \vec{a}_3)$ are related to the C_{ijkl} referenced with respect to a base orthogonal axes system $(\vec{a}_1, \vec{a}_2, \vec{a}_3)$. By the transformation

$$C'_{ijkl} = \sum_{k=1}^3 \sum_{l=1}^3 \sum_{p=1}^3 \sum_{q=1}^3 \omega_{ki} \omega_{lj} \omega_{ps} \omega_{qt} C_{klpq} \quad (2-11)$$

where the $\omega_{\alpha\beta}$ are the elements of the rotation matrix associated with the coordinate transformation. The components $\omega_{\alpha\beta}$ could be identified as the direction cosine between \vec{a}_α and \vec{a}_β . It is convenient to express the $\omega^{\alpha\beta}$'s in terms of three Eulerian angles in order to emphasize the fact that only three of the nine components $\omega_{\alpha\beta}$ are independent[65].

The Eulerian angles are defined as the three successive angles of rotation. The sequence will be started by rotating the initial system of axes x, y, z, by an angle ϕ counterclockwise about the z axis, and the resultant coordinate system will be labelled the $\xi \eta \zeta$ axes. In the second stage the intermediate axes, $\xi \eta \zeta$, are rotated about the ξ axis counterclockwise by an angle θ to produce another intermediate set, the $\xi' \eta' \zeta'$ axes. Finally the $\xi' \eta' \zeta'$ axes are rotated counterclockwise by an angle ψ about the ξ' axis to produce the desired $x' y' z'$ system of axes. Fig. 19 illustrates the various stages of the sequence. The

Eulerian angles θ , ϕ , ψ thus completely specify the orientation of x' , y' , z' as the three needed generalized coordinates[66-68].

The elements of the rotation matrix corresponding to successive rotation of ϕ , θ , and ψ are defined:

$$\Omega = \begin{bmatrix} \omega_{xx} & \omega_{xy} & \omega_{xz} \\ \omega_{yx} & \omega_{yy} & \omega_{yz} \\ \omega_{zx} & \omega_{zy} & \omega_{zz} \end{bmatrix} \quad (2-12)$$

where

$$\begin{aligned} \omega_{xx} &= \cos\psi\cos\phi - \cos\theta\sin\phi\sin\psi & \omega_{xy} &= \cos\psi\sin\phi + \cos\theta\cos\phi\sin\psi & \omega_{xz} &= \sin\psi\sin\theta \\ \omega_{yx} &= -\sin\psi\cos\phi - \cos\theta\sin\phi\cos\psi & \omega_{yy} &= -\sin\psi\sin\phi + \cos\theta\cos\phi\cos\psi & \omega_{yz} &= \cos\psi\sin\theta \\ \omega_{zx} &= \sin\theta\sin\phi & \omega_{zy} &= -\sin\theta\cos\phi & \omega_{zz} &= \cos\theta \end{aligned}$$

These general relationships are the basis for the analysis of the anisotropic elastic properties. The macroscopic approach applies these relationships to the bulk material; the microscopic approach utilizes these relationships to describe the response of each phase and attempts to construct the bulk response; the molecular approach attempts to predict the fundamental materials descriptors C_{ijkl} for each phase component from a knowledge of the inter- and intramolecular force field.

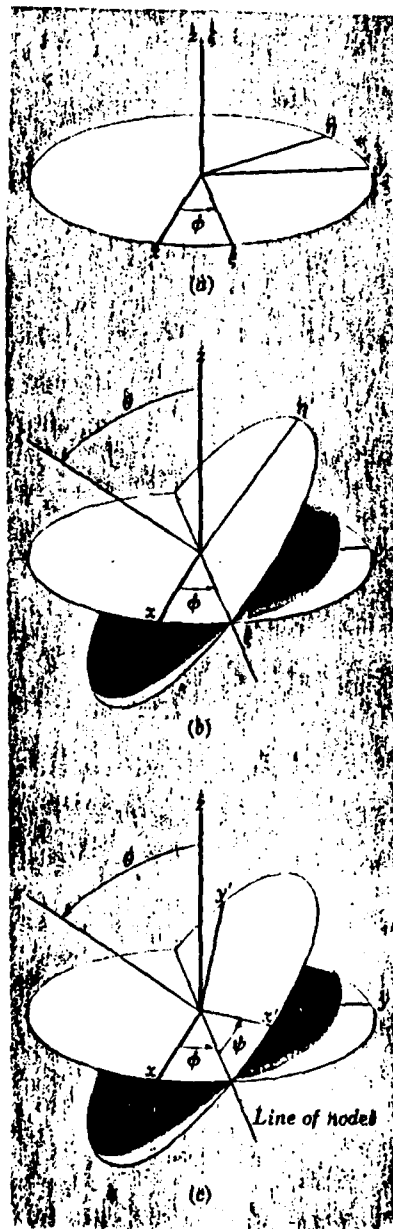


Fig.19 The rotations defining the Eulerian angles[68].

2.3 Different Approaches

2.3.1 Macroscopic Approach

The macroscopic approach is directed toward the practical issue of describing and predicting the extent to which structural components will deform in response to an applied load, or alternately, the resistance of a structure to deformation. From practical characterization consideration, it is usually easier to control the application of a load rather than to prescribe a pure deformation. Hence it is useful to express strain as a function of stress. From the generalized Hooke's law

$$\epsilon = S \sigma \quad (2-13)$$

where array S is a 6×6 symmetric matrix whose elements S_{pq} (S_{pq}) are compliance constants.

Traditionally, material response has been characterized by engineering "constants" rather than by the elements of the elastic constants or compliance array. Young's modulus E is used to describe the ability of a material to transfer a pure extensional strain into a pure extension stress; Poisson's ratio ν is used to indicate the extent to which the lateral dimensions of a body change

in response to a pure extensional (or compressional) strain, and finally, the shear modulus G is used to describe the ability of a material to transfer a pure shear stress. For anisotropic materials, the engineering constants are reported for each unique material direction[65].

Practically, the loading (or deformation) directions are not coincident with the unique axes. The material response in any arbitrary direction can be predicted through the transformation matrix by Eulerian angles, as described before. In other words, the engineering constants (E_i , G_{ij} , ν_{ij}) experimentally determined for loads (or deformation) along the material axis can be used to compute S_{ij} 's, and the response with respect to various angles may also be determined from these relationships.

2.3.2 Microscopic Approach

The microscopic approach to the analysis of mechanical properties takes cognizance of the heterogeneous nature of materials. Heterogeneity in polymer fibers may be the natural consequence of fibrillar or crystal morphologies developed under various processing conditions. The microscopic approach treats each phase component of a heterogeneous system as a homogeneous

continuum whose properties are specified; i. e., the properties of the phase component are assigned the role of the fundamental material descriptors. Although the macroscopic approach makes use of the techniques of analysis reviewed above, the internal stress-strain fields of a heterogeneous system are locally influenced by[65-71]:

- (i) the relative magnitudes of the phase properties,
- (ii) the size, shape and relative orientation of the phase regions,
- (iii) the packing geometries of the phase regions,
- (iv) the connection between the phase regions.

In order to achieve tractability, simplifying assumptions concerning the internal stress-strain fields and the phase geometry have been introduced. Two of the most fundamental models are Voigt (Uniform Strain) and Reuss (Uniform Stress) for two-phase materials:

$$\text{Voigt: } C_{ij} = V_\alpha \langle C_{ij} \rangle_\alpha + V_\beta \langle C_{ij} \rangle_\beta \quad (2-14)$$

$$\text{Reuss: } S_{ij} = V_\alpha \langle S_{ij} \rangle_\alpha + V_\beta \langle S_{ij} \rangle_\beta \quad (2-15)$$

where V_α and V_β are volume fractions of phases α and β , and

$$\langle C_{ij} \rangle_\gamma = \int_0^\pi \int_0^\pi \int_0^{\pi/2} n_\gamma(\theta, \phi, \psi) C_{ij}(\theta, \phi, \psi)_\gamma \sin\theta d\theta d\phi d\psi \quad (2-16)$$

$$\langle S_{ij} \rangle_\gamma = \int_0^\pi \int_0^\pi \int_0^{\pi/2} n_\gamma(\theta, \phi, \psi) S_{ij}(\theta, \phi, \psi)_\gamma \sin\theta d\theta d\phi d\psi \quad (2-17)$$

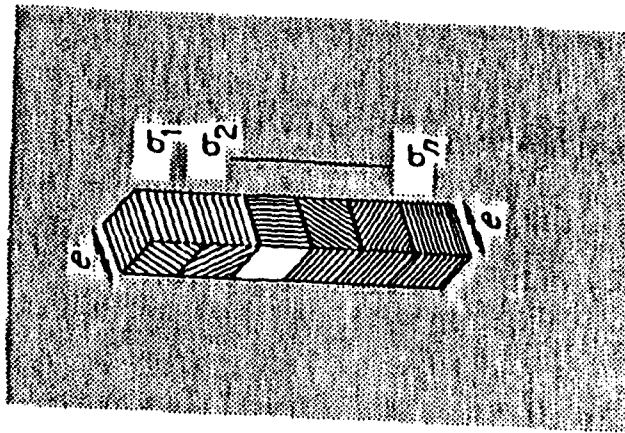
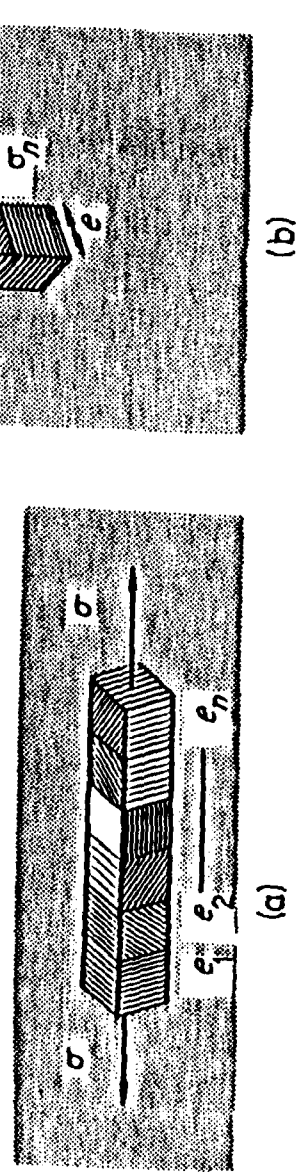
where n is an orientation density function. Fig. 20 shows the aggregate model (a) for uniform stress; (b) for uniform strain[64].

Several other models have been proposed to give results intermediate between the extremes of the Voigt and Reuss models. Models based on uniform stress or uniform strain fields can not be strictly correct. The interfacial forces are not in equilibrium for constant strain; interfacial discontinuities must exist for constant stress. Nonetheless, these models do provide useful guidelines at a minimum of computational effort. They may be readily extended to multiphase ($n > 2$) systems[64,65].

2.3.3 Molecular Approach

The molecular approach is different from both methods described above. It abandons the continuum view and adopts an atomistic view which has the potential for associating specific mechanical behavior with chemical groups. For polymer materials, this approach may be associated with the coordination of motions of various segments of the molecule as the geometrical rearrangements due to external actions.

Fig.20 The aggregate models: (a) for uniform stress; and (b) for uniform strain[64].



The link between the molecular view and the continuum view may be readily established by coupling the mechanistic foundation of the continuum approach with the structure-energy relation of the molecular approach. The general basis for this characterization may be loosely categorized in terms of two extreme organizational models; the ideal gas-like organization and the ideal crystal-like organization. The former model reflects the characteristics of a disordered system in which the random nature of the structure dominates the behavior. Alternatively, the ideal crystal-like model emphasizes the characteristics of perfectly ordered systems. The ability to specify precise locations emphasizes the symmetry of the systems and promotes the utilization of the mathematical tools of crystallography in the analysis of these well-ordered models. Changes in the intra- and intermolecular energies associated with the mutual interactions of specific chemical species dominate the behavior of the system. It is reasonable to expect that these two distinct theoretical approaches may eventually provide the underlying concepts for a molecular description of the disordered and ordered phase components of heterogeneous polymeric materials. But both of them are only the ideal models. There will still be a distance between the models and practical situations[65].

The PBZT fibers are composed of rod-like rigid molecules. Hence, in the molecular approach they are close to the ideal crystal-like organizations. It is our task to combine all three methods for exploring the relationship between the structure and properties of PBZT high-performance fibers. Emphasis would be given to the microscopic approach, since this approach provides the crucial connection between the macroscopic area and the molecular mechanism.

Chapter Three

Characterizations and Experimental Methods

To characterize the structure and properties of PBZT high performance fibers, two main methods were chosen. One was wide angle x-ray diffraction (WAXD) and the other was laser-generated ultrasound. In addition, transmission electron microscopy (TEM), scanning electron microscopy (SEM), differential scanning calorimetry (DSC), thermogravimetry (TG), density measurements, etc were used as the auxiliary tools.

3.1 Laser Generated Ultrasonic Method

The measurement of propagation of ultrasonic waves in polymer fibers discloses the correlations between ultrasonic velocity and the elastic properties of the materials. Analysis of the results has enabled the principal independent elastic constants to be derived and to obtain data on the quantitative behavior of the fibers as a function of the structure[72].

3.1.1 Basic Principles of Laser Generated Ultrasound

Soon after the development of the pulsed laser in the early 1960s, it was used to generate stress waves in solids by a very rapid deposition of energy. Since that early work, there have been a number of reports of the use of laser-generated ultrasound to analyze bulk solids.

When the laser beam impinges on the solid sample, stress waves (including ultrasonic waves) are generated by the rapid energy deposition. The deposition of heat energy in the sample is so rapid that it results in an unbalanced stress state as the heated material wants to expand but is initially restrained by its own inertia. This stress gradient then begins to propagate through the sample. In addition, the intense heat from the laser pulse also results in a very short duration high pressure, which contributes to stress wave initiation by acting on the material surface. These are two main reasons which explain the cause of laser-generated ultrasound qualitatively[64,73-81].

Before proceeding to discuss the principles for a unidirectional fiber, a brief introduction to the propagation of acoustic waves in anisotropic solids is given[73]. In an anisotropic material there is no simple relation between the direction of propagation of a wave and the direction of the particle

displacement. In other words, in general the waves are not pure longitudinal or transverse types.

The equation of motion for an anisotropic body may be obtained by substituting the stress σ_{ij} from the anisotropic linear stress-strain relation

$$\sigma_{ij} = c_{ijkl} \epsilon_{kl} \quad (i,j,k,l = 1,2,3) \quad (3-1)$$

into Newton's law

$$\frac{\partial \sigma_{ij}}{\partial x_j} = \rho \frac{\partial^2 u_i}{\partial t^2} \quad (3-2)$$

to give

$$\rho \frac{\partial^2 u_i}{\partial t^2} = c_{ijkl} \frac{\partial \epsilon_{kl}}{\partial x_j} \quad (3-3)$$

where ρ is the volume density and u_i the displacement vector. Substitution of the linearized strain-displacement relation

$$\epsilon_{kl} = \frac{1}{2} \left(\frac{\partial u_k}{\partial x_l} + \frac{\partial u_l}{\partial x_k} \right)$$

into eqn.(3-3) yields

$$\rho \frac{\partial^2 u_i}{\partial t^2} = \frac{1}{2} c_{ijkl} \left(\frac{\partial^2 u_k}{\partial x_j \partial x_l} + \frac{\partial^2 u_l}{\partial x_j \partial x_k} \right) \quad (3-4)$$

A unidirectional material is assumed to be transversely isotropic, i.e. isotropic in planes normal to the preferred direction (for a fiber, the fiber

direction). Because of the symmetry with respect to k and l , eqation (3-4) reduces to

$$\rho \frac{\partial^2 u_i}{\partial t^2} = c_{ijkl} \frac{\partial^2 u_l}{\partial x_j \partial x_k} \quad (3-5)$$

Supposed that a plane harmonic wave has the form of

$$u_i = (A d_i) \exp[i \omega(x_j s_j - t)] \quad (3-6)$$

where A is the amplitude, d_i the component of a unit vector defining the direction of the particle displacements, ω is the angular frequency and s_j the component of the slowness vector defined as

$$s_j = \frac{n_j}{v} \quad (3-7)$$

here n_j are the components of a unit vector describing the direction of propagation and v is the phase velocity. Substitution eqn.(3-6) into eqn.(3-5) gives

$$(c_{ijkl} s_j s_l - \rho \delta_{ik}) u_k = 0 \quad (3-8)$$

where δ_{ik} is the Kronecker delta. Eqn.(3-8) is known as Christoffel's equation.

It represents a set of three homogeneous equations of the first degree with u_1 , u_2 and u_3 as unknowns. For a nontrivial solution the determinant of the coefficients must be zero,

$$|c_{ijkl} s_j s_l - \rho \delta_{ik}| = 0 \quad (3-9)$$

which can also be written in the form

$$|\Gamma_{jk} - \rho v^2 \delta_{jk}| = 0 \quad (3-10)$$

where $\Gamma_{ik} = c_{ijkl} n_j n_l$ is known as the Christoffel stiff matrix. Evaluation of Eqn.(3-10) leads to a cubic equation in (v^2):

$$\begin{bmatrix} (\Gamma_{11} - \rho v^2) & \Gamma_{12} & \Gamma_{13} \\ \Gamma_{12} & (\Gamma_{22} - \rho v^2) & \Gamma_{23} \\ \Gamma_{13} & \Gamma_{23} & (\Gamma_{33} - \rho v^2) \end{bmatrix} \quad (3-11)$$

where

$$\Gamma_{11} = c_{11}n_1^2 + c_{66}n_2^2 + c_{55}n_3^2 + 2c_{56}n_2n_3 + 2c_{15}n_1n_3 + 2c_{16}n_1n_2$$

$$\Gamma_{12} = c_{16}n_1^2 + c_{26}n_2^2 + c_{45}n_3^2 + (c_{46} + c_{25})n_2n_3$$

$$+ (c_{14} + c_{56})n_1n_3 + (c_{12} + c_{66})n_1n_2$$

.....

Here for stiffnesses, we use the abbreviated subscript notation as follows:

1 - $x_1 x_1$

2 - $x_2 x_2$

3 - $x_3 x_3$

4 - $x_2 x_3, x_3 x_2$

5 - $x_1 x_3, x_3 x_1$

6 - $x_1 x_2, x_2 x_1$

when x_3 is chosen as the axis of symmetry in the fiber direction, the five independent stiffnesses form a matrix of the form:

$$[\mathbf{c}_{ij}] = \begin{bmatrix} \mathbf{c}_{11} & \mathbf{c}_{12} & \mathbf{c}_{13} & 0 & 0 & 0 \\ \mathbf{c}_{12} & \mathbf{c}_{11} & \mathbf{c}_{13} & 0 & 0 & 0 \\ \mathbf{c}_{13} & \mathbf{c}_{13} & \mathbf{c}_{33} & 0 & 0 & 0 \\ 0 & 0 & 0 & \mathbf{c}_{44} & 0 & 0 \\ 0 & 0 & 0 & 0 & \mathbf{c}_{44} & 0 \\ 0 & 0 & 0 & 0 & 0 & \mathbf{c}_{66} \end{bmatrix} \quad (3-12)$$

where $\mathbf{c}_{66} = \frac{1}{2} (\mathbf{c}_{11} - \mathbf{c}_{12})$ and the five independent stiffness constants are \mathbf{c}_{11} , \mathbf{c}_{12} , \mathbf{c}_{13} , \mathbf{c}_{33} and \mathbf{c}_{44} .

The three roots of eqn. (3-11) are in general different, giving rise to three different velocities of propagation. From the properties of \mathbf{c}_{ijkl} it follows that Γ_{ik} is a symmetric and positive definite matrix. That is, $\Gamma_{ik} = \Gamma_{ki}$, $\Gamma_{ik} \mathbf{d}_i \mathbf{d}_k \geq 0$ for all \mathbf{d}_i . This results in all of the eigenvalues of Γ_{ik} being real and positive and their corresponding eigenvectors orthogonal. Therefore, for a given direction of propagation, defined by the vector \mathbf{n}_j , there will be three waves with mutually perpendicular displacement vectors, but with different phase velocities (Fig. 21). In general, these waves will not be pure longitudinal or pure transverse, but one quasilongitudinal (QL) and the others quasi-transverse (QT) (Fig. 22). However, for certain special directions of propagation, which are usually directions of symmetry, one wave is pure longitudinal and the others pure transverse.

Now we adapt the general analysis to the propagation of plane waves in

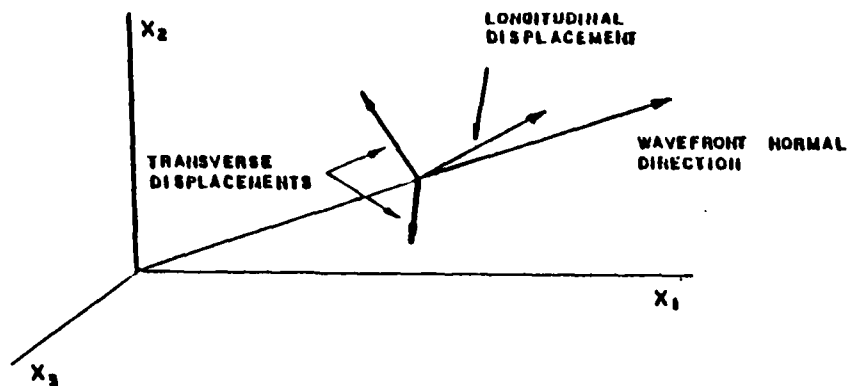


Fig.21 Relationships between the wavefront normal direction and displacement vectors[73].

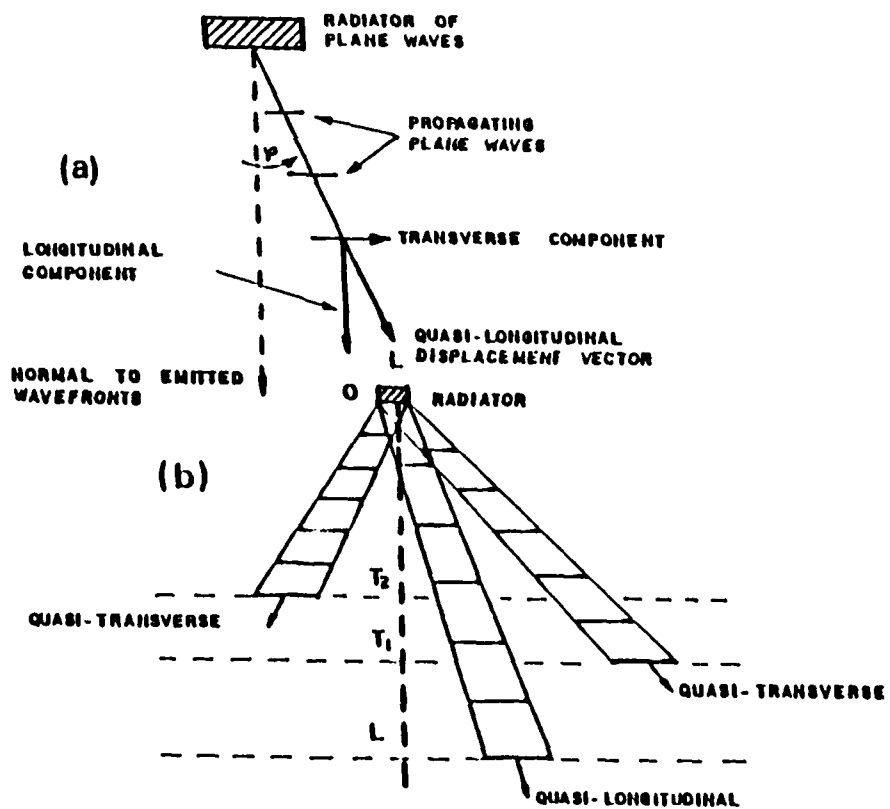


Fig.22 (a) The propagation of a QL wave in an anisotropic material; (b) the three possible energy beam in an anisotropic solid[73].

unidirectional fibers. Since the (x_2, x_3) plane is defined by the fiber direction and the wave direction, the plane harmonic wave is written as

$$\mathbf{u} = (u_1, u_2, u_3) \exp[i\omega(s_3x_3 + s_2x_2 - t)] \quad (3-13)$$

where u_i are the amplitudes of displacement components. The Christoffel's equation for these amplitudes may lead to the following set of equations

$$(c_{33}s_3^2 + c_{44}s_2^2 - \rho)u_3 + (c_{44} + c_{23})s_2s_3u_2 = 0 \quad (3-14)$$

$$(c_{44} + c_{23})s_2s_3u_3 + (c_{44}s_3^2 + c_{22}s_2^2 - \rho)u_2 = 0 \quad (3-15)$$

$$(c_{44}s_3^2 + c_{66}s_2^2 - \rho)u_1 = 0 \quad (3-16)$$

where ρ and c_{ij} are effective mass density and the effective elastic moduli, respectively. Eqn.(3-16) represents a pure transverse wave with displacement vector perpendicular to the plane containing the preferred direction and the direction of propagation. Since

$$s_3 = \frac{\cos\phi}{v} \quad \text{and} \quad s_2 = \frac{\sin\phi}{v} \quad (3-17)$$

where ϕ denotes the angle between the preferred direction and the direction of propagation, the velocity of propagation will be

$$v = \left(\frac{c_{44} \cos^2\phi + c_{66} \sin^2\phi}{\rho} \right)^{\frac{1}{2}} \quad (3-18)$$

with $c_{66} = \frac{c_{11} - c_{12}}{2}$. Waves in the preferred direction and in any perpendicular direction have velocities $(\frac{c_{44}}{\rho})^{\frac{1}{2}}$ and $(\frac{c_{66}}{\rho})^{\frac{1}{2}}$, respectively. The

waves governed by these equations are not purely longitudinal, nor purely transverse, because the displacement vector is neither in the direction of, nor perpendicular to the direction of propagation. The velocities of propagation are obtained by equating to zero the determinant of the coefficients:

$$(\mathbf{c}_{33} \cos^2\phi + \mathbf{c}_{44} \sin^2\phi - \rho v^2) (\mathbf{c}_{44} \cos^2\phi + \mathbf{c}_{22} \sin^2\phi - \rho v^2) = \\ (\mathbf{c}_{44} + \mathbf{c}_{23})^2 \sin^2\phi \cos^2\phi \quad (3-19)$$

When the wave propagates along the preferred direction or normal to it, that is, along a symmetry axis of the fibers, equations for both cases are obtained from Eqns. (3-14), (3-15) and (3-17) by setting $\phi = 0$ and $\phi = 90^\circ$, respectively. For propagation along the fiber direction ($\phi = 0$),

$$\left(\frac{\mathbf{c}_{33}}{v^2} - \rho \right) \mathbf{u}_3 = 0 \quad (3-20)$$

and

$$\left(\frac{\mathbf{c}_{44}}{v^2} - \rho \right) \mathbf{u}_2 = 0 \quad (3-21)$$

there results a purely longitudinal wave traveling with velocity $(\frac{\mathbf{c}_{33}}{\rho})^{1/2}$ and a purely transverse wave with velocity $(\frac{\mathbf{c}_{44}}{\rho})^{1/2}$. For propagation normal to fiber axis ($\phi = 90^\circ$),

$$\left(\frac{\mathbf{c}_{44}}{v^2} - \rho \right) \mathbf{u}_3 = 0 \quad (3-22)$$

and

$$\left(\frac{c_{22}}{v^2} - \rho \right) u_2 = 0 \quad (3-23)$$

there results a purely transverse wave with velocity $(\frac{c_{44}}{\rho})^{1/2}$ and a purely longitudinal wave with velocity $(\frac{c_{22}}{\rho})^{1/2}$.

Moseley, Ward and Samuels analyzed three possible situations for the ultrasonic waves propagating in polymer fibers (Fig. 23)[64,82,83]. If the fiber is assumed to be a single phase system, namely its properties are a function of the average distribution of the units that make up the system, the sonic velocity, c is related to the sonic modulus, E_s , i.e. elastic modulus measured at high frequency via the expression

$$E_s = \rho c^2 \quad (3-24)$$

3.1.2 Experimental Method

Single laser pulses of about 15 ns duration and about 20 mJ energy are produced by a Q-switched ND:YAG laser. The light is aimed directly at the fiber sample (which comprises a few to a few hundred single filaments) and is focused into a line near the sample by a simple cylindrical lens with its axis

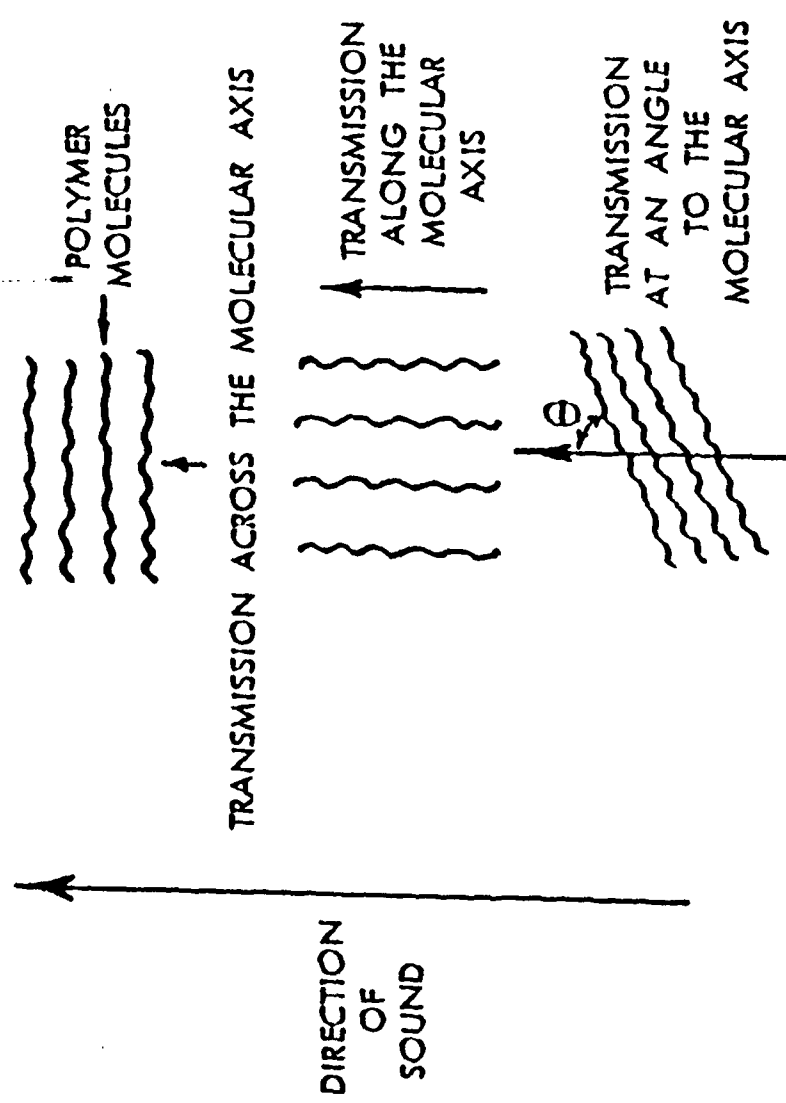


Fig.23 Possible modes of sound transmission in polymers[83].

perpendicular to that of the fiber (the wavelength used is 532 nm). The fiber sample hangs vertically and perpendicular to the direction of the beam. Close to the upper end, a piezoelectric transducer (Acoustic Emission Technology Co., Model MC500) is clamped. At the other end, a cardboard glued on the fibers is used to hang various weights. Mirrors to reflect the laser beam are mounted on a stage which can move up and down (parallel to the axis of the sample) to change the laser incidence positions on the fibers (Fig. 24). A sampling oscilloscope is triggered by signal from a photodiode placed near the beam at the lens. The amplified and filtered signal from the transducer is recorded at a 10 ns sampling period. The travel time is taken as the difference in the time between the trigger and the arrival of the ultrasonic wave at the transducer (seen in Fig. 25). The end and temperature effects are reduced by dividing the difference between two propagation distances by the difference between the corresponding arrival times for equivalent points on the pulsed sinusoidal signal. For each pulse these times are recorded for several points on the signal. The frequency (about 0.5 MHz) of the observed signal is a function of the characteristics of the pulse, the fiber, the transducer, the electronics, the stress on the fibers and the temperature. The resonant frequency of the transducer and attenuation in the fiber are especially important. The

SOUND VELOCITY MEASUREMENT SYSTEM

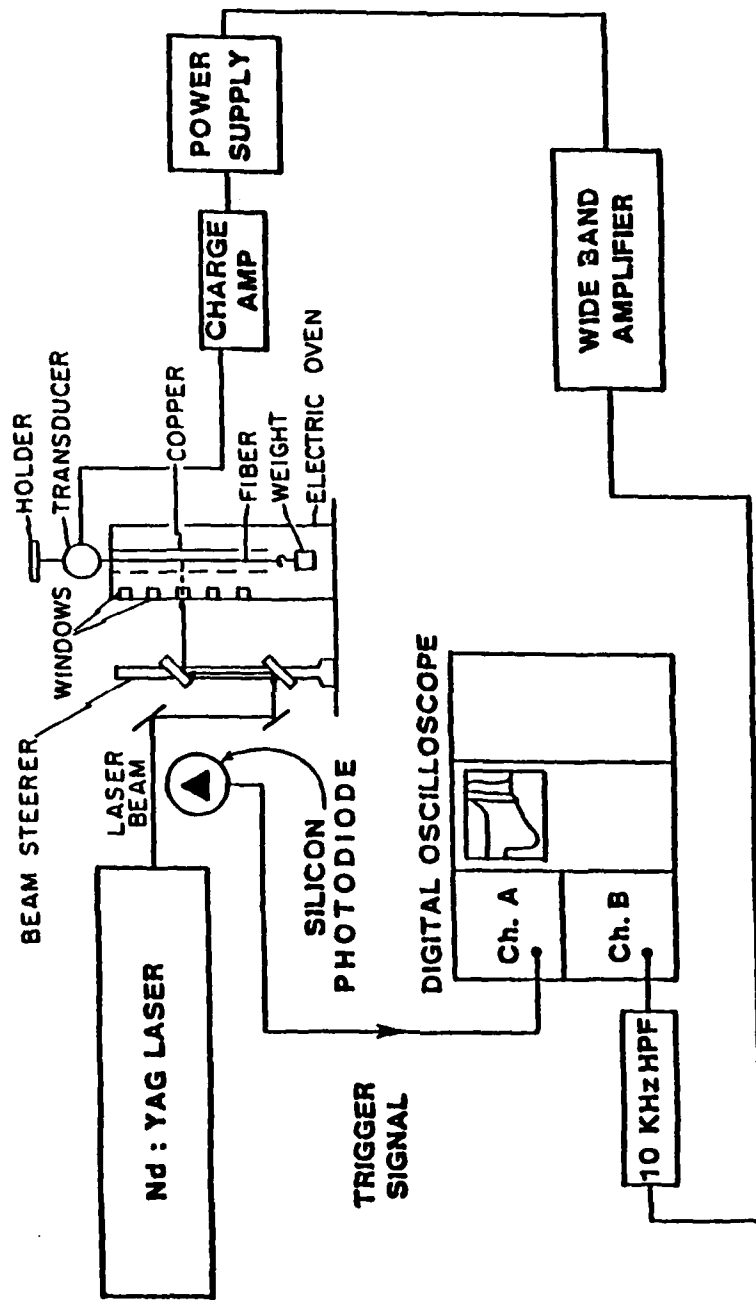


Fig.24 Schematic diagram of ultrasonic velocity measurement system

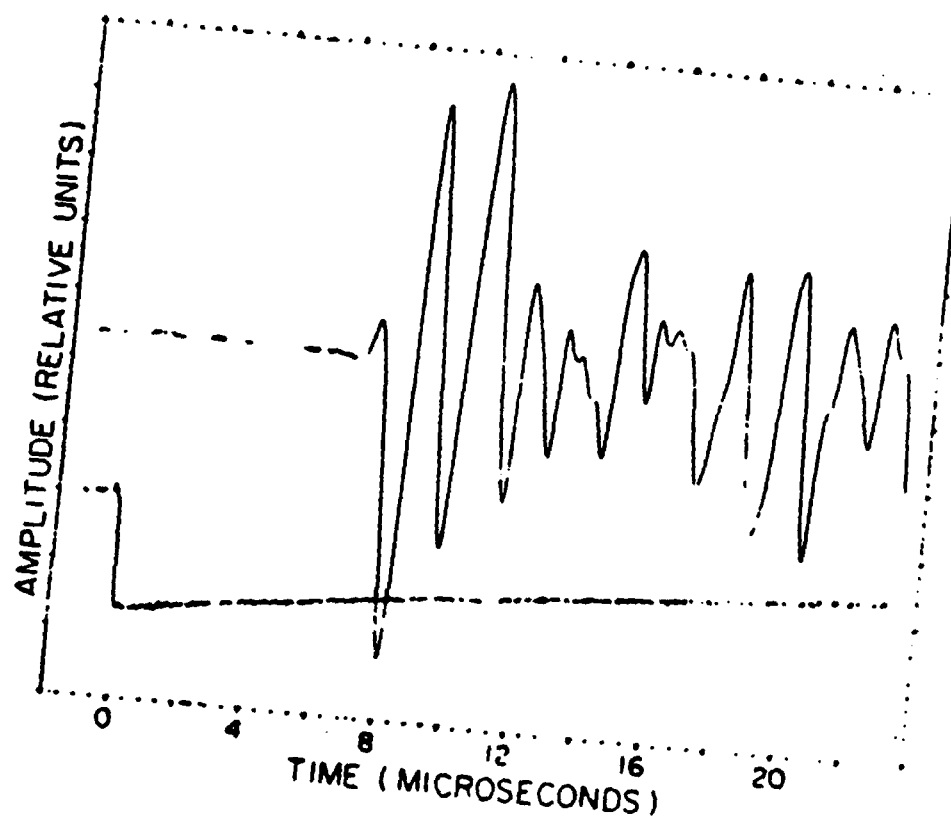


Fig.25 Typical ultrasonic signal (top) and trigger signal (bottom) recorded and displayed.

standard deviation of the measured velocity varies somewhat from sample to sample, but overall is about 1%. When the ultrasonic wavelength is very large by comparison with the diameter of the sample fiber, the particle displacement is effectively axial for longitudinal mode. If the attenuation is small, Young's modulus (E_s) is equal to the product of the density (ρ) and the square of the velocity (c):

$$E_s = \rho c^2 \quad (3-24)$$

The oven surrounding the sample (shown in Fig. 24) is composed of silica materials. Heating-wires were wrapped on surface of inner cylinder. The heating rate can be varied from 4–10°C/min. It also can keep the temperature constant at the desired temperature. The temperature was calibrated by means of the voltage of a control-variatic and temperature reading from a fine thermometer. The Maximum temperature used was about 650°C. Various static weights are hung on the lower end of the fiber sample. The maximum stress put on the HT PBZT fibers was about 2000 MPa.

3.2 X-ray Diffraction Method

X-ray diffraction is a very useful technique for determination of the morphological structure. WAXS has been of especially vital importance in understanding oriented crystalline polymers and has been widely used in measuring their crystalline parameters. In the x-ray analysis of polymeric materials, the diffraction data are usually less abundant than in the case of single crystals of low-molecular-weight substances. (1) The polymer samples are normally composed of many crystallites; (2) the crystalline areas coexist with the disorder areas; (3) the orientation will influence the measurement, especially for polymer fibers and films. So, several supplemental methods have been developed to give successful results in determinations of crystal modulus, orientation distributions, unit cell parameters and other crystalline features[84-94].

3.2.1 Basic Principles of WAXD of Crystalline Polymers

since crystalline polymers are composed of many crystallites, the resulting WAXS pattern will be the superposition of the diffraction from each crystallite individually. If all of the crystallites are randomly oriented in the polymer sample, the crystallites which are in the position to reflect the (hkl) plane will give a scattered beam at the same angle with reference to the incident x-

ray beam. The locus of all directions making that angle with the incident beam is a cone having the incident beam as its axis, which results in a so-called Debye-Scherrer ring. Its position on the x-ray diffraction film characterizes the interplanar spacing (d-spacing), which produced the diffraction according to Bragg's law. Other crystallites in the polymer sample will be in a position to scatter x-rays from different crystal planes and the sum of all of the diffracted beams will be the final powder pattern obtained from the sample.

If the crystallites are not oriented at random but have their crystal axes oriented around a preferred direction, the Debye-Scherrer ring will not be complete but instead will take the form of an arc. In polymer fibers, some crystal axes will have a preferred direction with respect to the axis of the fibers. At the same time, other crystal axes will have a random orientation in the plane perpendicular to the fiber axis. This is a so-called uniaxial orientation situation. Thus, if a diffraction photograph of a crystalline polymer is taken with the incident x-ray normal to the fiber axis, an oriented rotation pattern will be obtained. This pattern demonstrates that crystallites have a preferred orientation with respect to the fiber axis. The more perfect the crystallites orient, the shorter the Debye-Scherrer arcs will be. At the extreme

they would become sharp spots.

Previous discussion shows that not only can the crystal structure of a crystalline polymer fiber can be determined by WAXS, but also the orientation of the crystallites. Furthermore, WAXS is the only practical method to measure the orientation distribution of the structural units, crystallites[87,88].

In addition, through the variation of a peak position ($\Delta\theta$), the changes in d-spacing caused by temperature, stress, etc. could be calculated[84,85]. If we know the stress applied to the crystals to cause the changes in d-spacing, we could determine the crystal modulus. From Bragg's law

$$\lambda = 2 d \sin\theta \quad (3-25)$$

so

$$d = \frac{\lambda}{2 \sin\theta} \quad (3-26)$$

By differentiation with respect to both sides of the equation

$$\Delta d = -\frac{\lambda}{2} \frac{\cos\theta}{\sin^2\theta} \Delta\theta \quad (3-27)$$

divided by d, we obtain

$$\frac{\Delta d}{d} = -\operatorname{ctg}\theta \Delta\theta \quad (3-28)$$

Using the stress vs d-spacing curve, we can extrapolate to zero stress to

get the d-spacing of the polymer crystal under no stress and from the slope of the curve we could calculate the crystal modulus.

For the WAXD measurements of the PBZT fibers, a Picker FACS-I system was used to characterize crystalline features such as unit cell parameters, crystal modulus, crystal size and crystallite orientation distributions. The instrument consists of a PDP 8/I computer which is interfaced to the goniostat (diffractometer), the x-ray tube shutter and the diffracted beam filter wheels. Each of the four goniostat angles (2θ , ω , χ , ϕ) is controlled by the computer programming[84,85].

3.2.2 X-ray Modulus Measurements

The measurements were made on the Picker FACS-I system with a filtered Cu K α radiation from a rotary anode x-ray tube. Incident and diffracted beam collimators with a 1.0 mm aperture diameter were used. The symmetrically variable aperture (SVA) was set at 2X5 (mm).

The sample was positioned to the center of the radiation. Owing to the ratio of $\Delta\theta$ to the fractional change in d being proportional to $\tan\theta$, the high angle reflection would give the best measure of the ratio of d-spacing variation

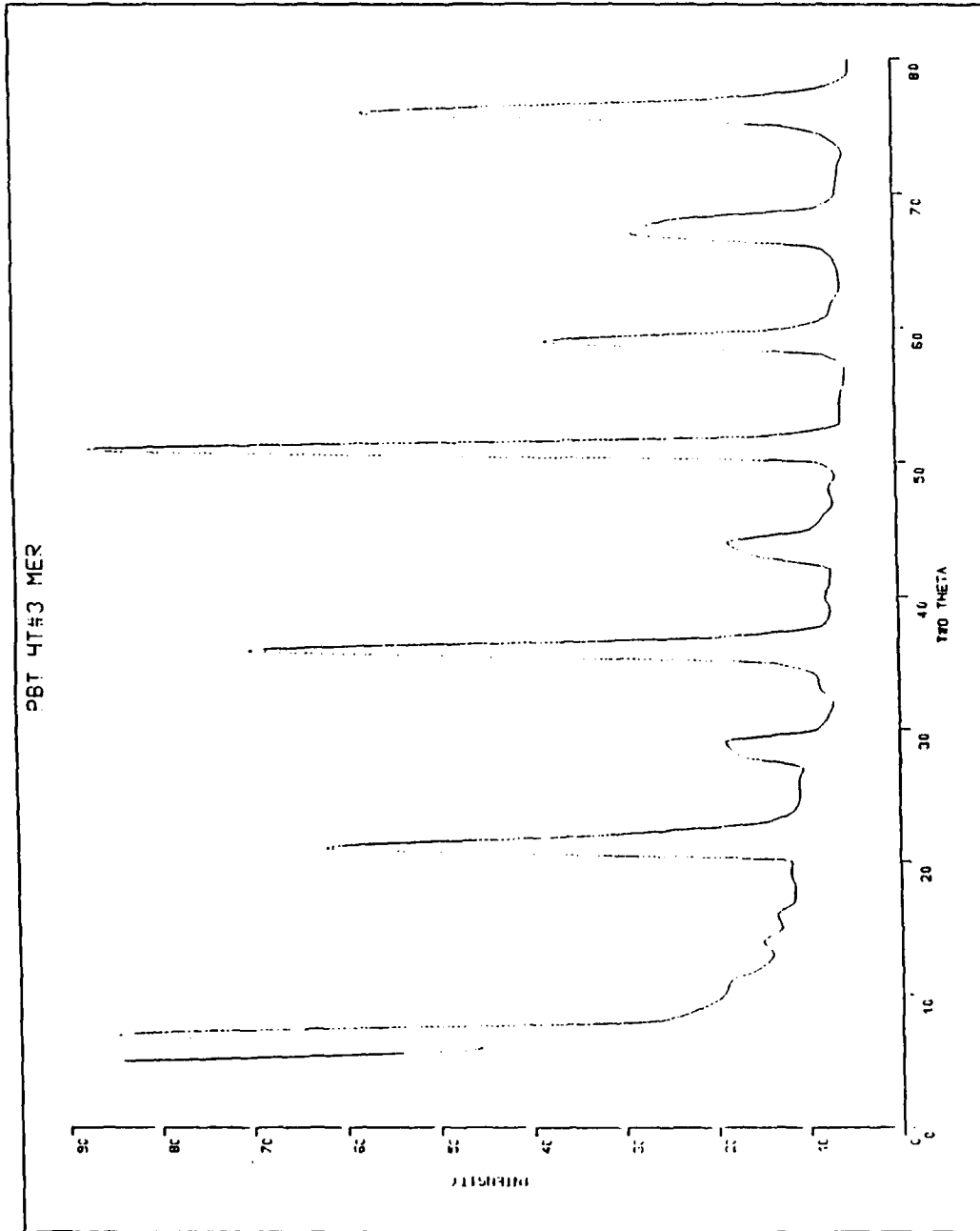


Fig.26 The meridian scanning of the HT-650 PBZT fiber sample for x-ray modulus measurement.

- a Mounting pin
- b Rotatable base. The bearing is shown as [diagram]
- c Nylon rotation lock screws
- d Tension screw (motorized)
- e Cantilever mount, moved by tension screw
- f Cantilever pivot
- g Tension arm (strain gauges on upper and lower surfaces)
- h Sample mount hinge (groove and knife edge pivot)
- i Upper sample mount
- j Sample mount length adjustment screws
- k Fiber sample
- l Sample end piece
- m Adjustment screws to center sample in the X-ray beam
- n Goniometer head base
- o Strain gauge bridge leads

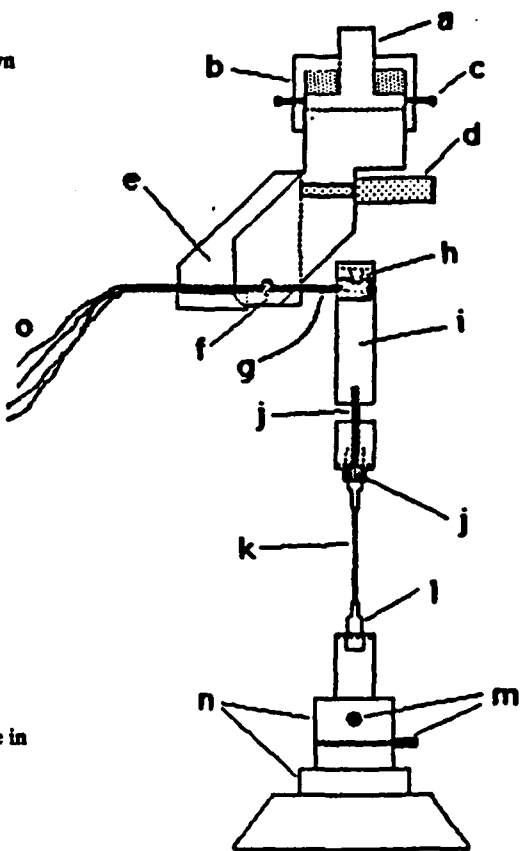


Fig.27 Fiber deformation device for x-ray modulus measurements[84].

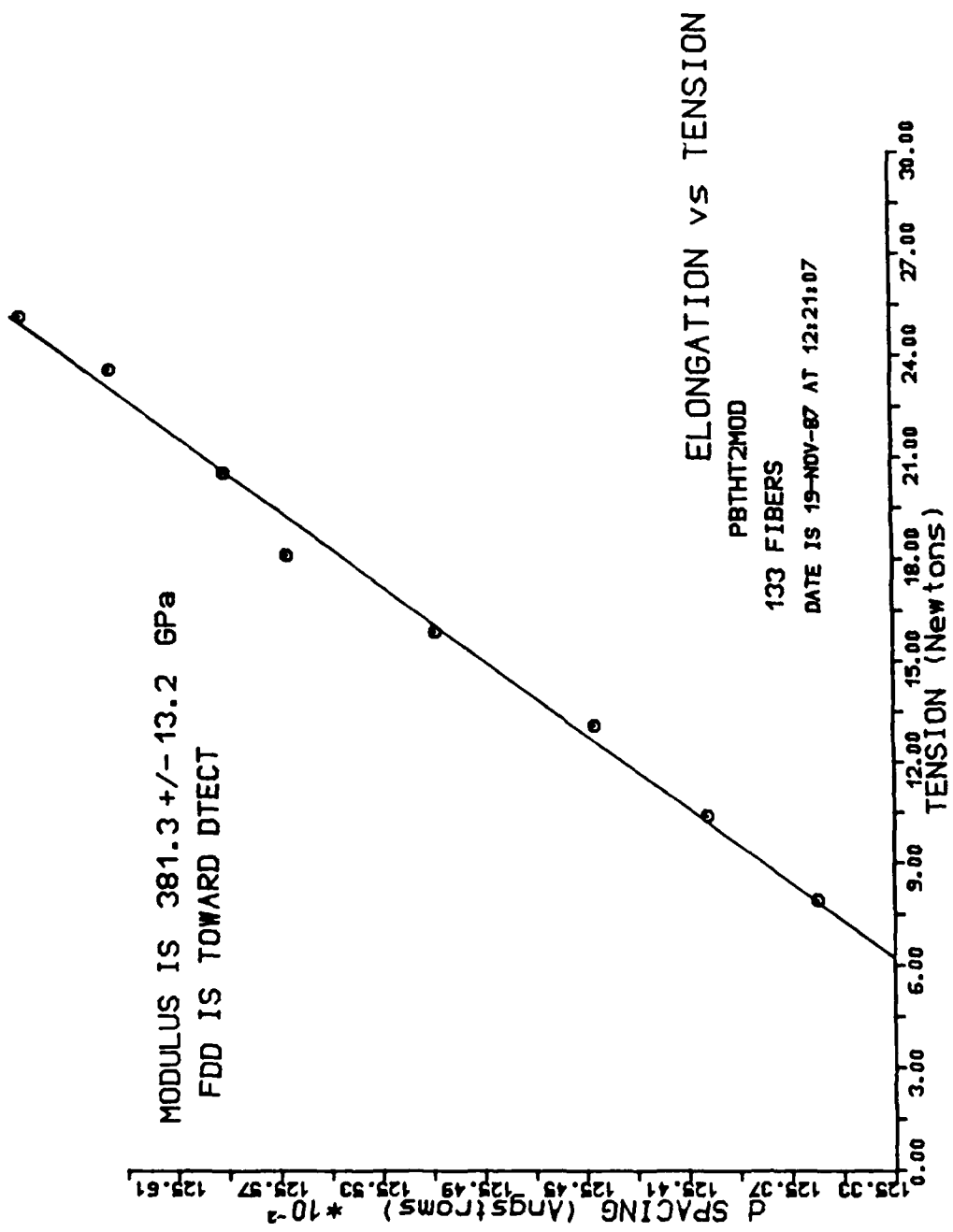


Fig.28 an example of the computer print-outs of the x-ray modulus measurements.

($\Delta d/d$). The (0 0 10) peak (at 2θ about 76°) was chosen as the reflected peak (Fig. 26)[84].

As shown in Fig. 27, the force put on the sample was controlled by the computer. When the tension limits were decided upon, the range between both limits would be divided into 6 or 7 equal intervals and 2θ would be determined at each selected tension. Starting at the maximum tension, the scans were made at every second tension value as the tension was decreased. The elastic modulus in GPa was calculated by a linear least-squares fit of the tension reading of the strain gauge (in mV) and the d-spacing (in Å). The relation between the linear modulus, Y, in Å/mV, was given by

$$Y = \frac{0.0882 d_o S \rho}{M D_f N_f} \quad (3-29)$$

where d_o (Å) was the average lattice spacing; S (gm/mV) the strain gauge calibration to measure the force put on the sample; ρ (g/cm³), the fiber density (measured by the pycnometer method); D_f , the denier per fiber and N_f , the number of filaments in the sample. The program could calculate the experimental results and print them out automatically. Fig. 28 is the print-out obtained from the x-ray modulus measurements.

3.2.3 Determination of Crystallite Orientation Distribution

The measurements were made on a Picker FACS-I system with filtered (0.01 inch Ni filter) Cu K α radiation from a rotary anode x-ray tube with HOG monochromator, operated at 50 kV and 50 to 80 mA. Incident and diffracted beam collimators with 1.0 mm and 1.5 mm apertures, respectively were used. The SVA was set at 3×3 (mm). The parameters of the analyzer were chosen as gain at 10, rejection limits were upper 7.0, lower 4.0; photomultiplier voltage potentiometer was at 4.42 (about 950V). The (010) crystal peak (2θ at about 26°) was chosen for the χ scan.

A fiber sample about 1mm thick was mounted on a sample holder. The sample was adjusted to the center of the radiation. Before a χ scan, a 2θ scan was examined first to select the correct peak center and the background positions above and below the peak ($\pm \Delta 2\theta$). The diffraction intensity was then the peak count minus the average background count rate. This measurement was totally controlled by the computer. The χ scan for PBZT fibers was carried out from -17° to $+17^\circ$, with the step of 0.1° . (Beyond the range, the first layer line would be encountered). Figs. 29-31 are the measured crystal orientation distribution curves (i. e. the I vs. χ curves) for all three PBZT samples.

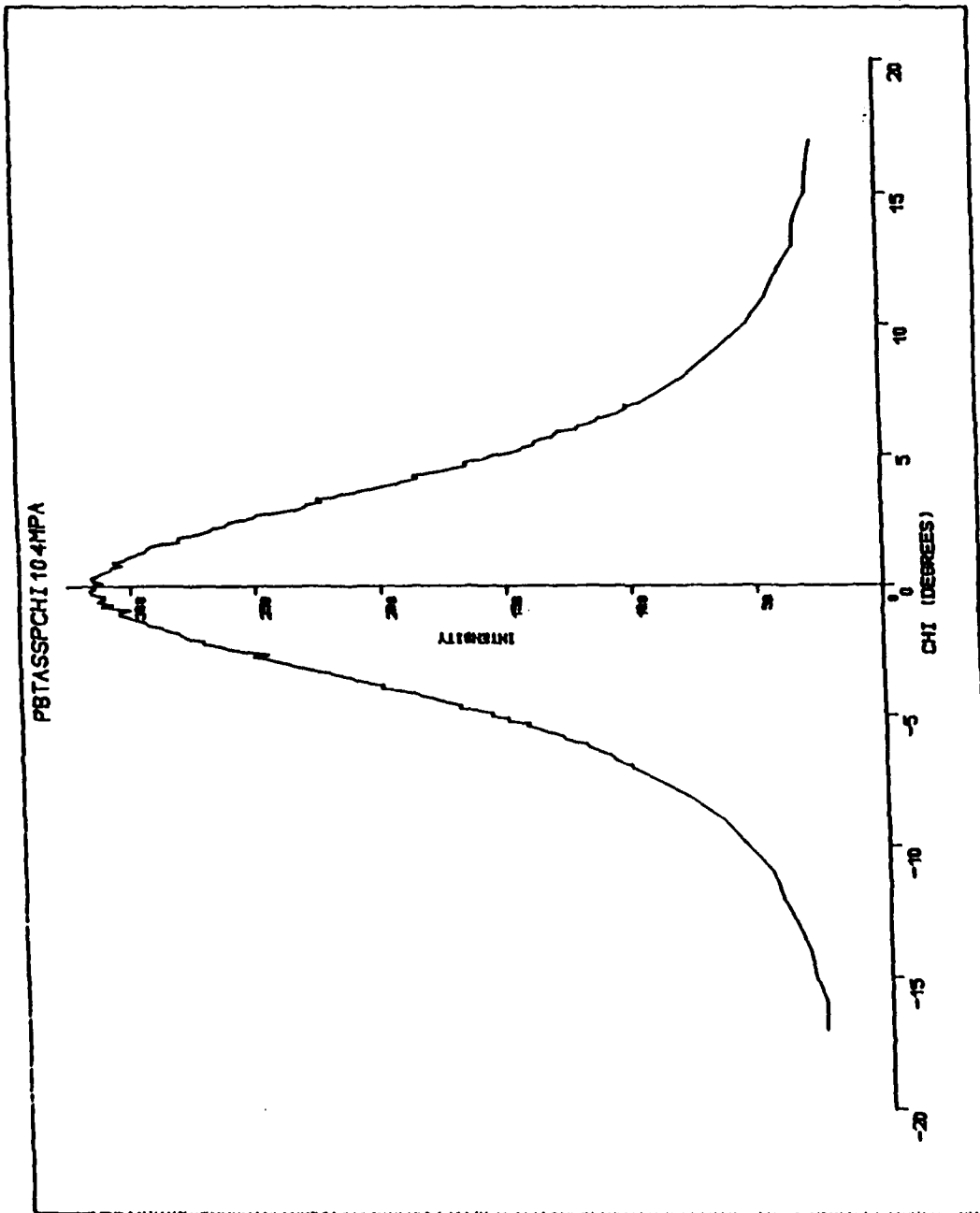


Fig.29 The χ scanning intensity distribution curve for as-spun PBZT fibers.

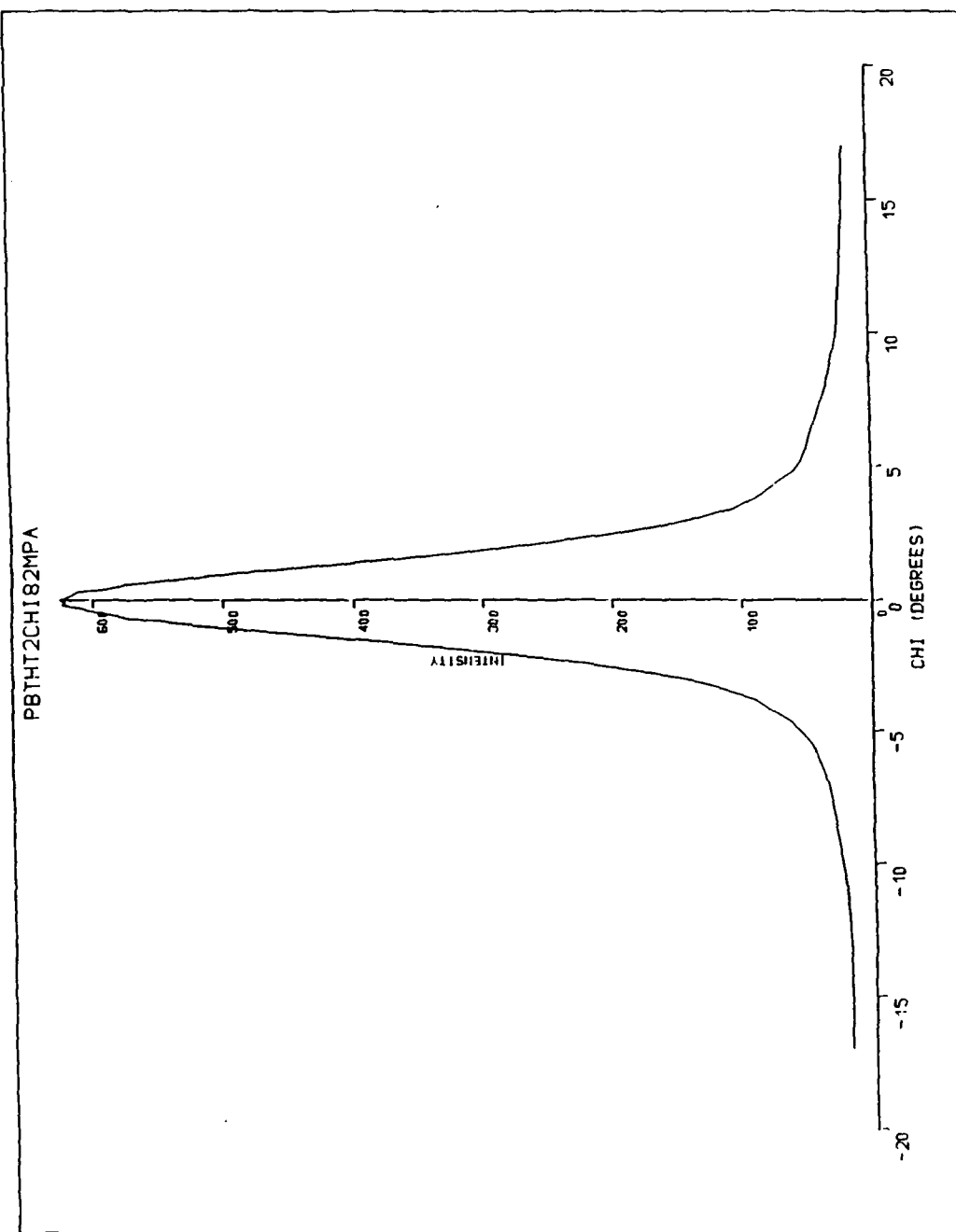


Fig.30 The χ scanning intensity distribution curve for HT-525 PBZT fibers.

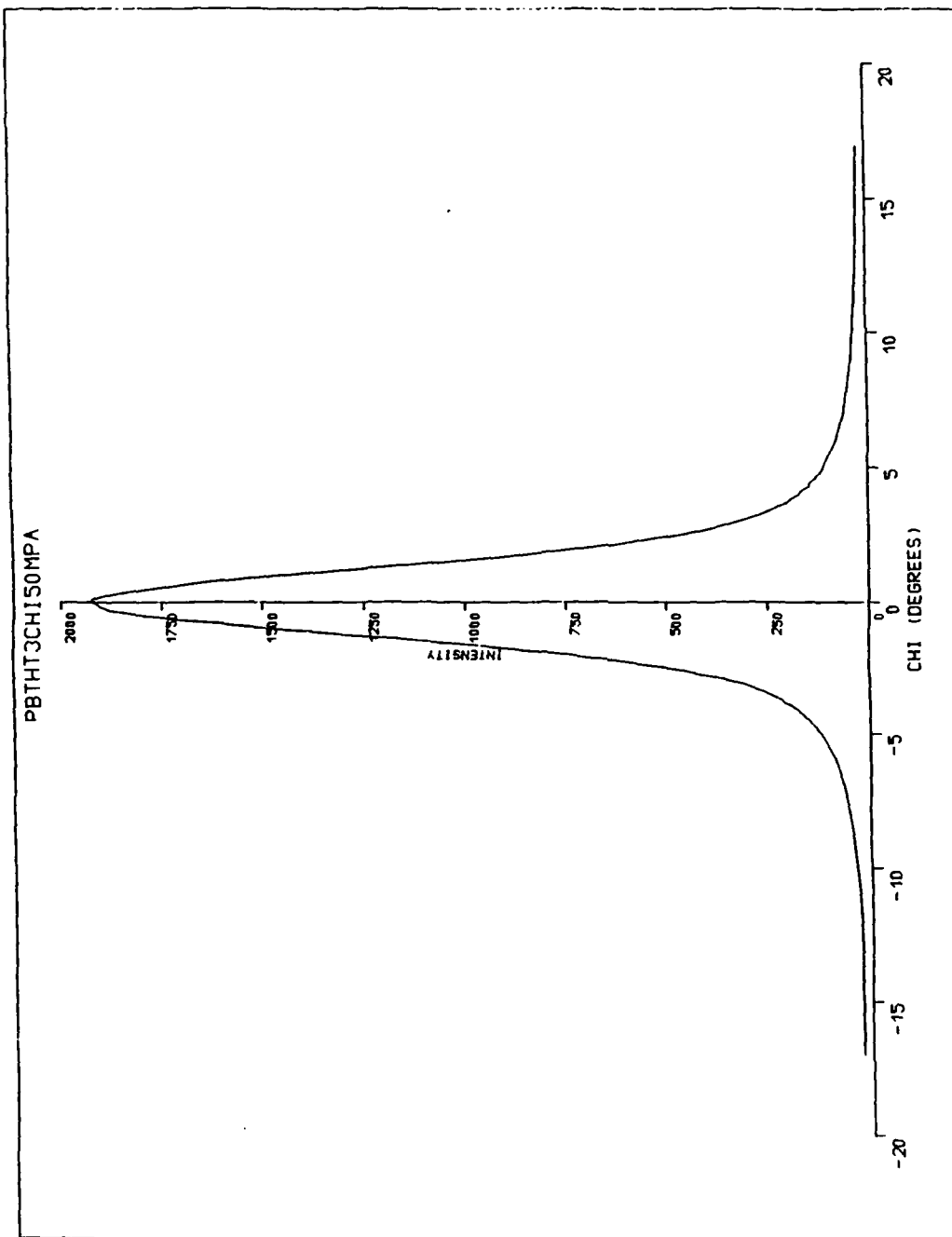


Fig.31 The χ scanning intensity distribution curve for HT-650 PBZT fibers.

3.2.4 Measurements of 2θ Equatorial Scan

The x-ray machine conditions were the same as the orientation measurement but 2θ was scanned instead of χ scanning. The equatorial 2θ scan was from 7° to 60° with 0.1° step. Figs. 32-4 are the measured equatorial 2θ scanning curves (i. e. I vs. 2θ curves) for all three PBZT samples.

The collected diffraction intensity data should be corrected and normalized as follows[89,90]:

- (1) Take the air scatter, $I_{\text{air}}(2\theta)$, away from the collected data $I_0(2\theta)$

$$I_1(2\theta) = I_0(2\theta) - I_{\text{air}}(2\theta) \quad (3-30)$$

- (2) Calculate the mean incoherent scatter, \bar{C} , and the mean square atomic scattering factor, \bar{f}^2

$$\bar{C} = \sum N_i \frac{C_i}{\sum N_i} \quad (3-31)$$

$$\bar{f}^2 = \sum N_i \frac{\bar{f}_i^2}{\sum N_i} \quad (3-32)$$

where C_i is the incoherent scatter for atoms of type i , N_i is the number of atoms of type i in the molecular repeat, and f_i is the atomic scattering factor given by Lee and Pakes.

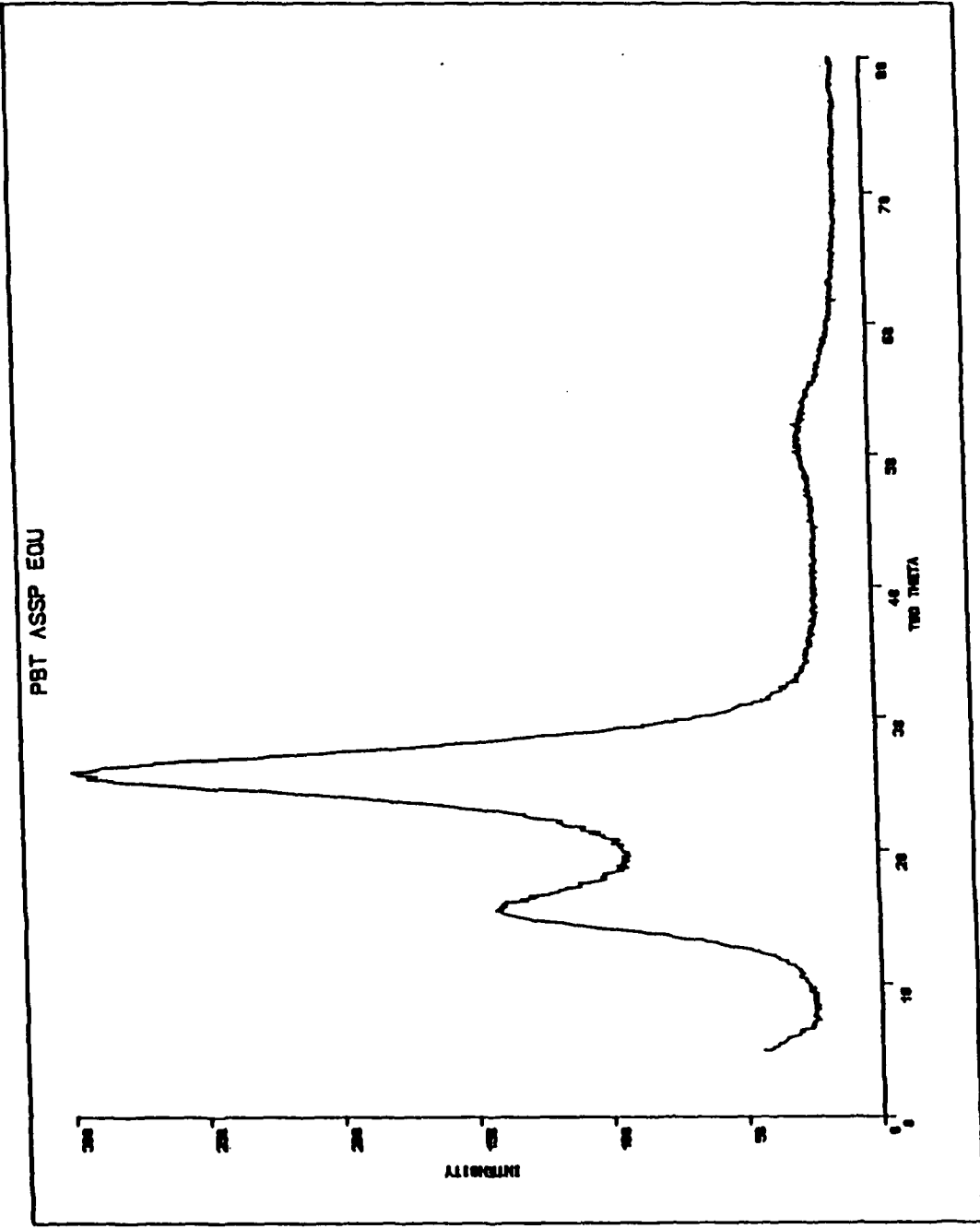


Fig.32 The equatorial 2θ scanning curve for as-spun PBZT fibers.

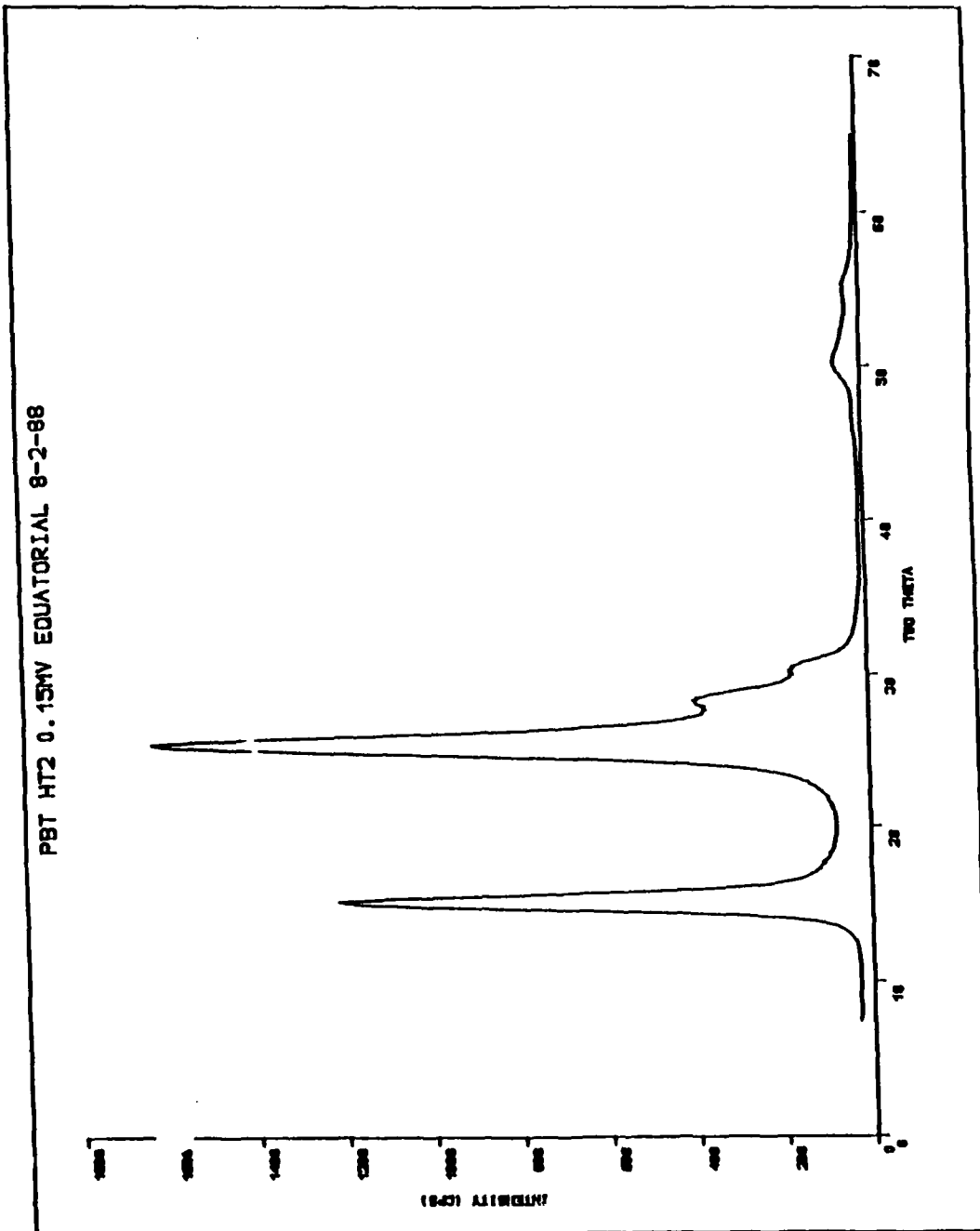


Fig.33 The equatorial 2θ scanning curve for HT-525 PBZT fibers.

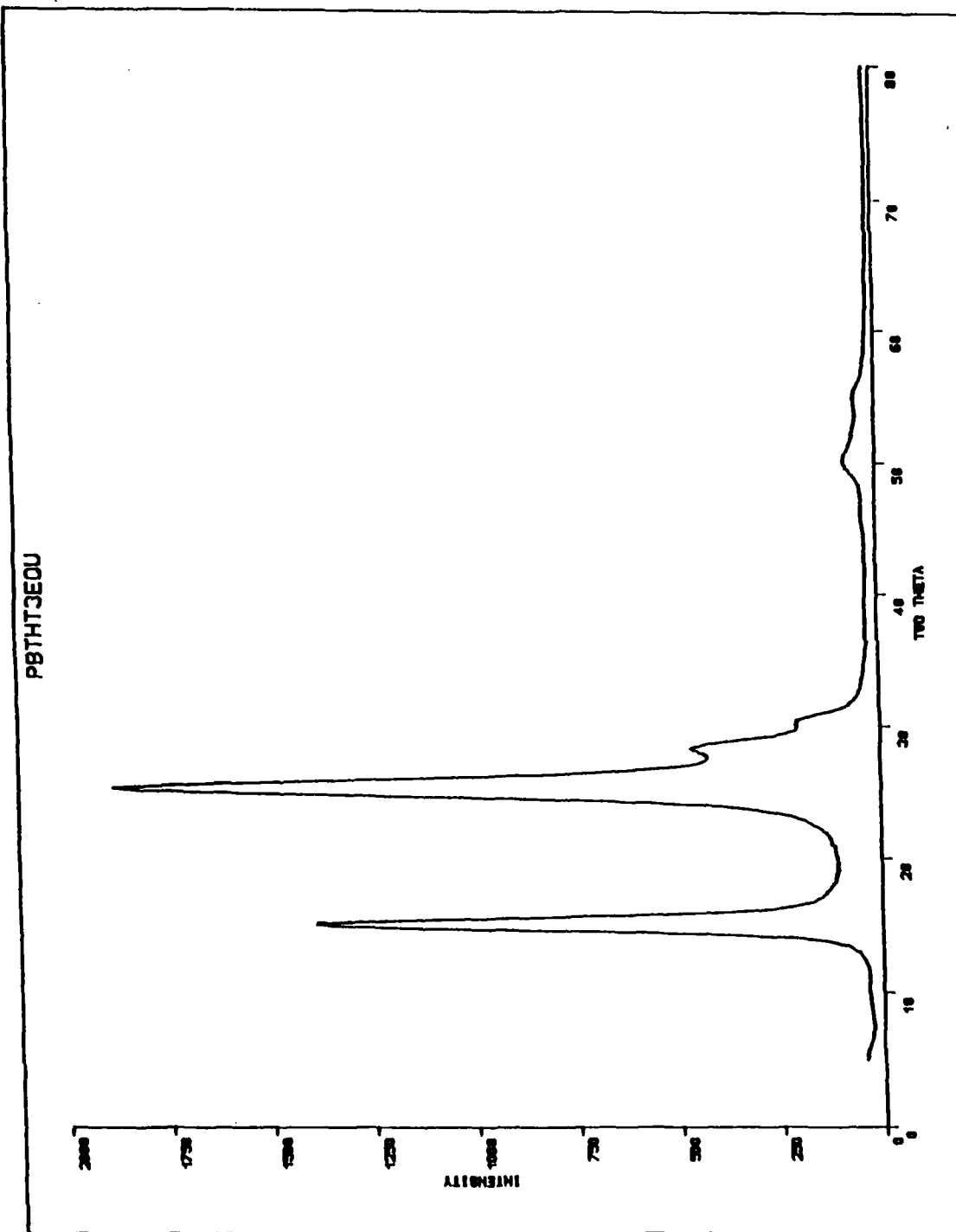


Fig.34 The equatorial 2θ scanning curve for HT-650 PBZT fibers.

(3) Evaluate the total scatter in terms of AR1

$$AR1 = \int_{2\theta_1}^{2\theta_2} (\vec{I}^2 + \bar{C}) \frac{\sin\theta \cos\theta d(2\theta)}{\lambda^2} \quad (3-35)$$

where λ is the wavelength of the radiation, θ is the diffraction angle.

(4) Correct polarization

$$I_2(2\theta) = I_1(2\theta) \frac{2}{(1 + \cos^2 2\theta)} \quad (3-36)$$

(5) Correct Lorentz geometric factor

$$I_3(2\theta) = I_2(2\theta) \sin 2\theta \quad (3-37)$$

(6) We obtain

$$AR2 = \int_{2\theta_1}^{2\theta_2} I_3(2\theta) \frac{\sin\theta \cos\theta}{\lambda^2} d(2\theta) \quad (3-38)$$

(7) Calculate the normalisation factor

$$N_f = \frac{AR2}{AR1} \quad (3-39)$$

(8) So, the scatter intensity array is

$$I_s(2\theta) = I_3(2\theta) N_f - \bar{C} \quad (3-40)$$

The above calculations were carried out by a computer program.

Owing to the peak overlapping, the normalized equatorial x-ray diffraction traces ($I_s(2\theta)$) were resolved into the individual peak by an

optimization method[89,90]. Each crystal peak is considered as a mixed function of the Gaussian and the Cauchy functions:

$$f_t G_t + (1 - f_t) C_t \quad (3-41)$$

where f_t is a profile parameter which can vary between -1 to +1; G_t , the Gaussian function; C_t , the Cauchy,

$$G_t = A_t \exp \left\{ -\ln 2 \left[\frac{2(x - P_t)}{W_t} \right]^2 \right\} \quad (3-42)$$

$$C_t = A_t / \left\{ 1 + \left[\frac{2(x - P_t)}{W_t} \right]^2 \right\} \quad (3-43)$$

where A_t is the peak height; W_t , the width of the peak at half height; P_t , the peak center position; x , the diffraction angle (2θ). The corresponding background scatter is expressed as a base-line:

$$a + bx \quad (3-44)$$

where a and b are constants. The function to be minimized in terms of these parameters is

$$S = \sum_{i=1}^n (I_{s_i} - I_{(norm)_i})^2 \quad (3-45)$$

If the 2θ range was from 7° to 35° , five peaks were used (100, 010, $1\bar{1}0$, 200 and 110); if the 2θ was from 35° to 65° , eight peaks were chosen ($2\bar{1}0$, 210, 300, $3\bar{1}0$, 020, $1\bar{2}0$, 120 and 310).

3.2.5 Thermal Wide Angle X-ray Diffraction Measurements

Wide angle x-ray diffraction measurements were also made as a function of temperature from 100° to 430°C with a Guinier-Simon camera which has a radius of 57.3 mm. The x-ray tube voltage was 40 kV and current, 30 mA. Cu K α radiation was used with a crystal monochromator and the size of the aperture was 4 mm. The specimen heating rate was 5.59°C/hr.

The data obtained from the x-ray diffraction photograph were read into a computer (Micro VAX) via a rotating autodensitometer with appropriate corrections for optical density. The data were treated in the same manner as described above.

3.3 Sampling

Three kinds of PBZT fibers, supplied by the Air Force Materials Lab, had been spun from nematic polyphosphoric acid solut: . They were washed and dried to a final denier of about 1.9. One was as-spun, two were heat-treated. (~~One had been treated at 525°C; the other, at 650°C~~) Their densities were 1.529, 1.573 and 1.572 respectively.

It was necessary to take some precautions in sample preparation. For the

samples used in the laser generated ultrasonic method, the fibers had to be long enough that several different incident positions on the fibers could be chosen and reflections of ultrasound from the ends did not interfere with the pulse being measured. The filaments in the sample were required to be straight and unbroken; further they all had to be of equal length between the generating and detecting positions so that the signals on the various fibers arrived at the detector in phase. We first tried different numbers of sample filaments in order to determine how many filaments we should choose. We tested sample bundles composed of 1, 2, 3, 5, 7, 10 and hundreds of filaments. All the results were nearly the same. That is, there was no big difference among the results for fibers with different numbers of filaments. But, if too many filaments are used, variations in length would cause the signal to travel different distances on different filaments and result in velocity errors as well as signal interference. If too few filaments are used, the signal would be too weak, especially for the as-spun fibers. Therefore, we chose sample bundles composed of 5-7 filaments.

For the samples used in x-ray orientation measurement, It is even more important to meet the requirements of straight and unbroken sample filaments. Since PBZT fibers are highly oriented, filament arrangement

seriously influences the measurement of χ -scan distribution. Therefore, great care was taken in making the χ -scan fiber sample. It is preferable to use a metal comb (to avoid static-electric charges) to comb the filaments vertically to guarantee all fibers in the sample being straight and parallel to each other. In addition, the diameter and thickness of the sample at the radiation position were kept nearly constant. Otherwise, the χ distribution will change.

Chapter Four

Results and Discussion

Some measured data for the as-spun and heat treated PBZT fibers are listed in Table 2. It is evident that the crystal structure of the HT fibers is much more perfect than that of as-spun fibers. The unit cell is more dense and the crystallites are bigger so that it has fewer defects and higher regularity. Because of the tension heat treatment, its orientation is more along the fiber axis. The differences between the HT-525 and HT-650 fibers are much less compared with the differences between the as-spun and HT fibers. All these features will be reflected in the nonlinear elasticity behavior which we shall discuss below in detail.

4.1 Nonlinear Stress-Modulus Behavior at Room Temperature

The Young's modulus of the PBZT fibers obtained at room temperature as a function of static tensile stress is shown in Fig. 35. The results are immediately reversible within the limits of experimental time and error. It is apparent that there is nonlinear elasticity for both as-spun and HT PBZT

Table 2. Some measured parameters about PBZT high-performance fibers

Samples	Fiber density (ρ_m , g/cm ³)	Crystal density (ρ_c , g/cm ³)	ρ_m/ρ_c	Crystal L_s (Å)	Crystal L_t (Å)	Half-width of orientation (deg.)	Sonic modulus (GPa)	Instron modulus (GPa)	X-ray modulus (GPa)
As-spun	1.529	-	-	12.8	15.1	4.67	181	186	344
HT-525	1.573	1.730	0.920	85.6	59.5	1.67	273	283	385
HT-650	1.577	1.732	0.921	85.9	60.1	1.43	291	290	393

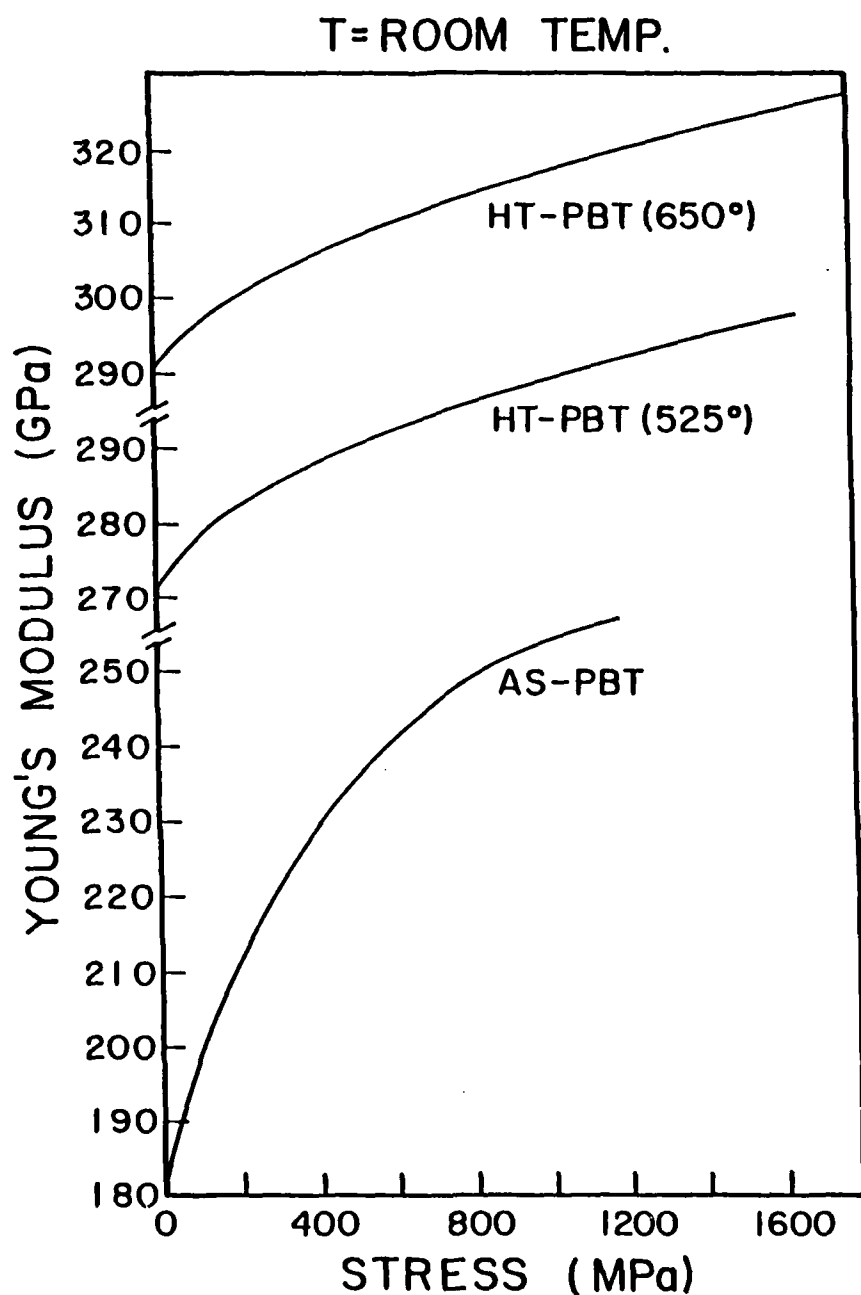


Fig.35 Young's modulus at room temperature as a function of static tensile stress for PBZT fibers: as-spun, heat treated at 525 and 650°C.

fibers. The nonlinear elasticity decreases with increasing initial modulus at no stress and it is less at high stress than at low stress for the same fiber. It might be anticipated that an increased alignment of the crystals with respect to the fiber axis with increasing stress is the main source of the nonlinear elasticity. Then, increased alignment with increasing initial modulus of the fiber would account for the decreasing nonlinear elasticity. The half-width at half maximum of the orientation distributions measured as a function of tensile stresses are shown in Fig. 36. They are in qualitative agreement with this idea. The fibers which exhibit a greater initial modulus also exhibit a more perfect alignment and a smaller change of alignment with tensile stress. However, the change of alignment does not completely explain the change of modulus either with stress or from one fiber to another. This can be seen in Fig. 37, in which Young's modulus is plotted vs the half-width of the crystallite orientation distribution for various tensile stresses at room temperature. The variation of modulus and half-width with stress for each fiber does not coincide with the variation of modulus and half-width from one fiber to the next at fixed stress. For the HT PBZT fibers, at the lower stresses, the experimental data fit comparatively well with the line compared to those of as-spun fibers. This means that for the HT fibers, especially at the lower tensile

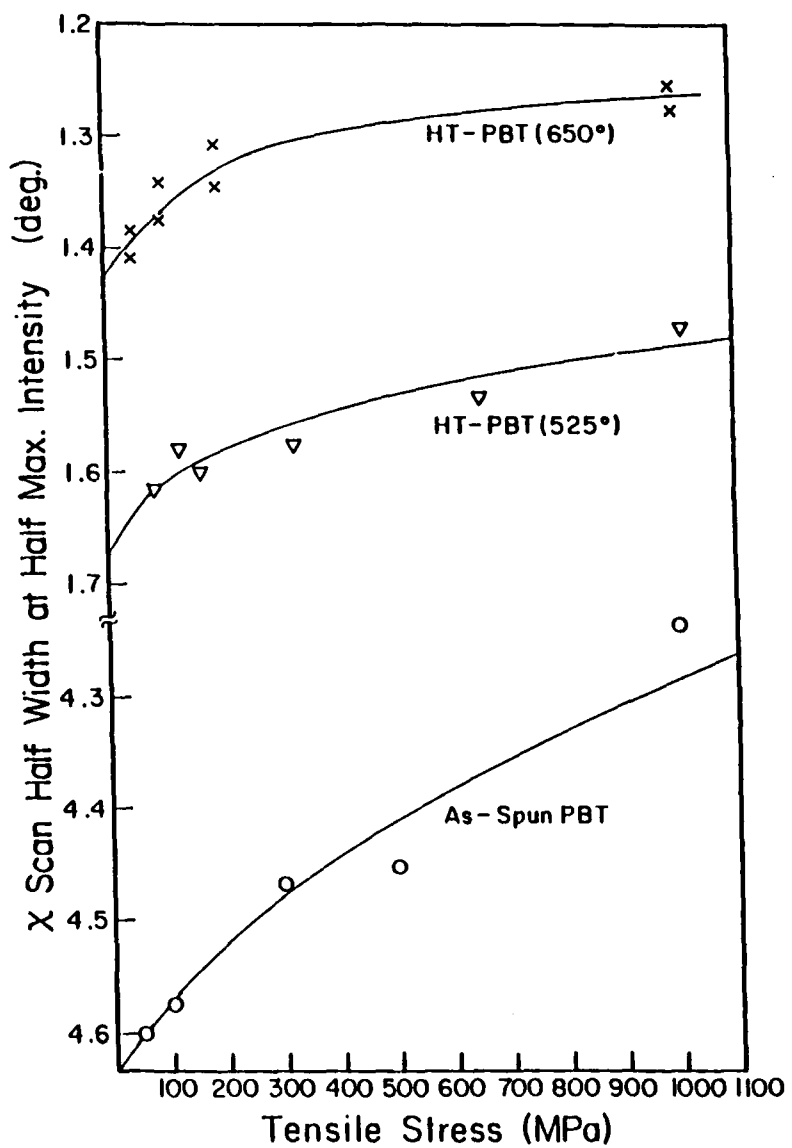


Fig.36 Half-width at half-maximum intensity determined by x-ray χ scans as a function of static tensile stress for the different fibers. The points are averages of several measurements taken at room temperature.

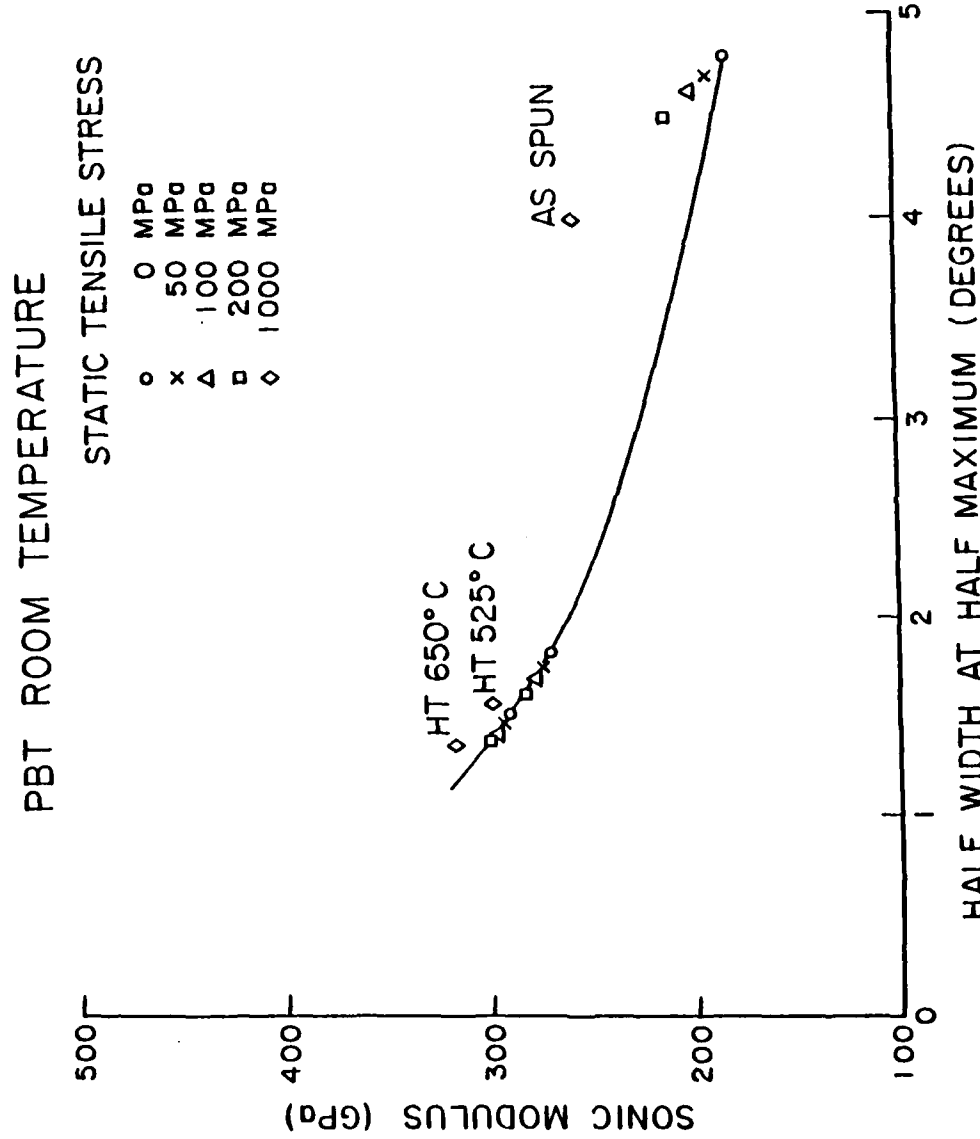


Fig.37 Young's modulus as a function of half-width at half-maximum for various tensile stresses and the different fibers.

stresses, the crystallite alignment is a dominating factor. However, for the higher stresses and for the as-spun fibers, there is clearly some other parameter involved. Similar effects are observed for pitch-based carbon fibers[95-98].

4.2 Uniform Stress and Uniform Strain Models

Uniform stress and uniform strain models were used to analyze the experimental data and to calculate the compliances of PBZT crystals and fibers.

4.2.1 Uniform Stress and Uniform Strain Assumptions for PBZT Crystals

For uniform stress, the analysis is straight forward. From the x-ray modulus measurements, the crystal modulus could be obtained directly for different samples. Namely, this is the modulus subject to the assumption that all crystals experience the same stress. For the as-spun sample, it is 344 GPa, for HT-525, 385 GPa and for HT-650, 393 GPa. Since the regularity, size and perfection of the PBZT crystals are continuously improved from the as-spun

samples to the HT650, their moduli are also improving. Various extrapolations of these values vs fiber density, half-width of crystal orientation distribution, reciprocal of crystal size and macroscopic modulus were used to obtain the value for an infinitely large crystal (Figs. 38-41). Their values were 524 GPa, 415 GPa, 402 GPa and 435 GPa, respectively. The average value of 444 GPa was chosen as the value for the perfect crystal of PBZT.

The analysis of the experimental data with the assumption that all crystals experience the same strain (uniform strain) is more complex. In addition to the value of $1/s_{22}$ for the perfect crystal, values of the other crystal constants are also required. For the narrow orientation distributions involved, the former is most important, but the latter contribute somewhat. Since most values of the PBZT crystal compliances and stiffnesses are not available, the published values for poly (*p*-phenylene benzobisoxazole) (PBO) were used[99]. The PBO and PBZT do not have major structural and property differences. In view of this and the lesser role of these constants in the calculation, the approximation is reasonable and should not qualitatively change the conclusions to be drawn.

For the uniform strain assumption, we have

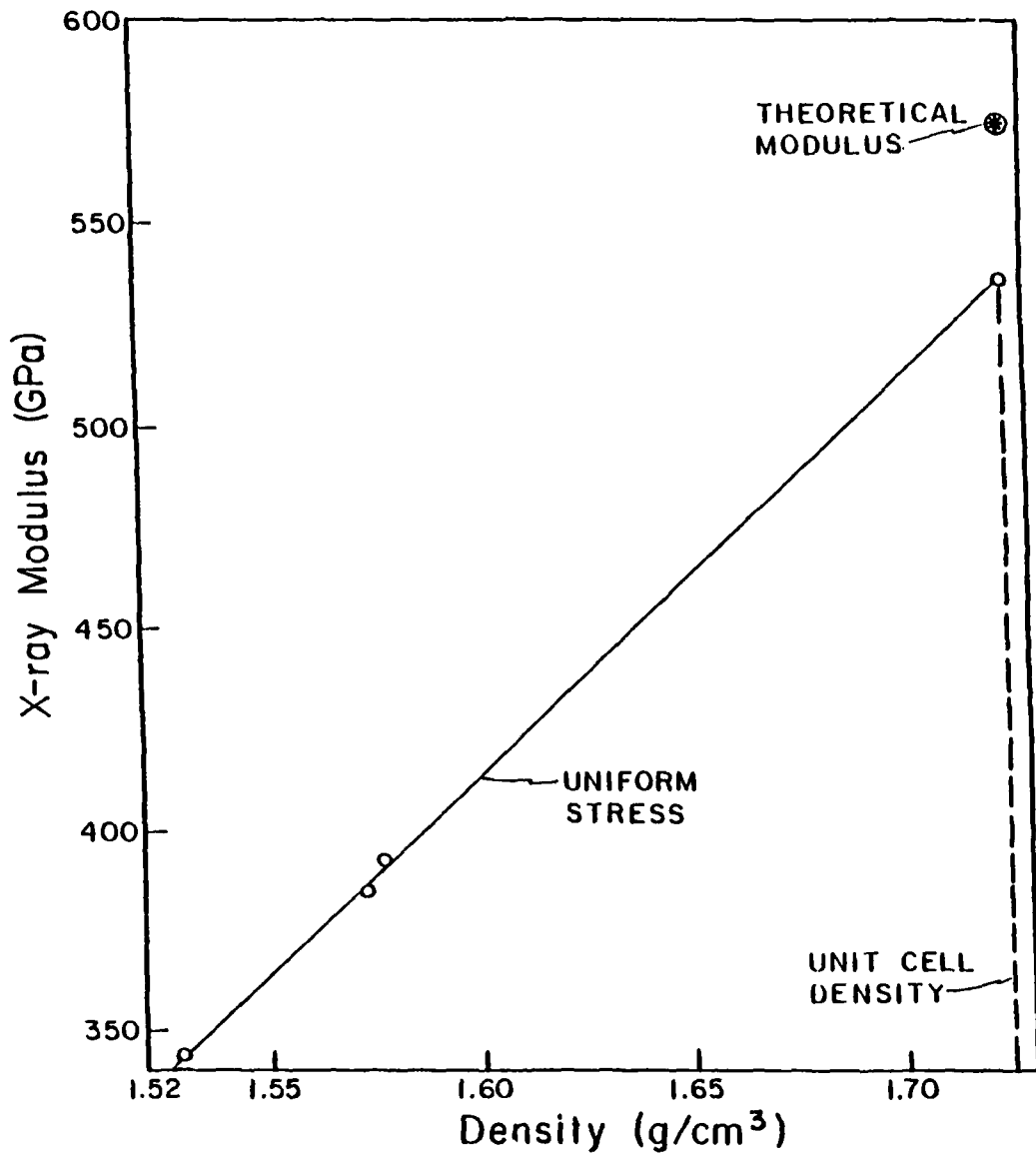


Fig.38 Fiber density vs crystal modulus for the assumptions of uniform stress.

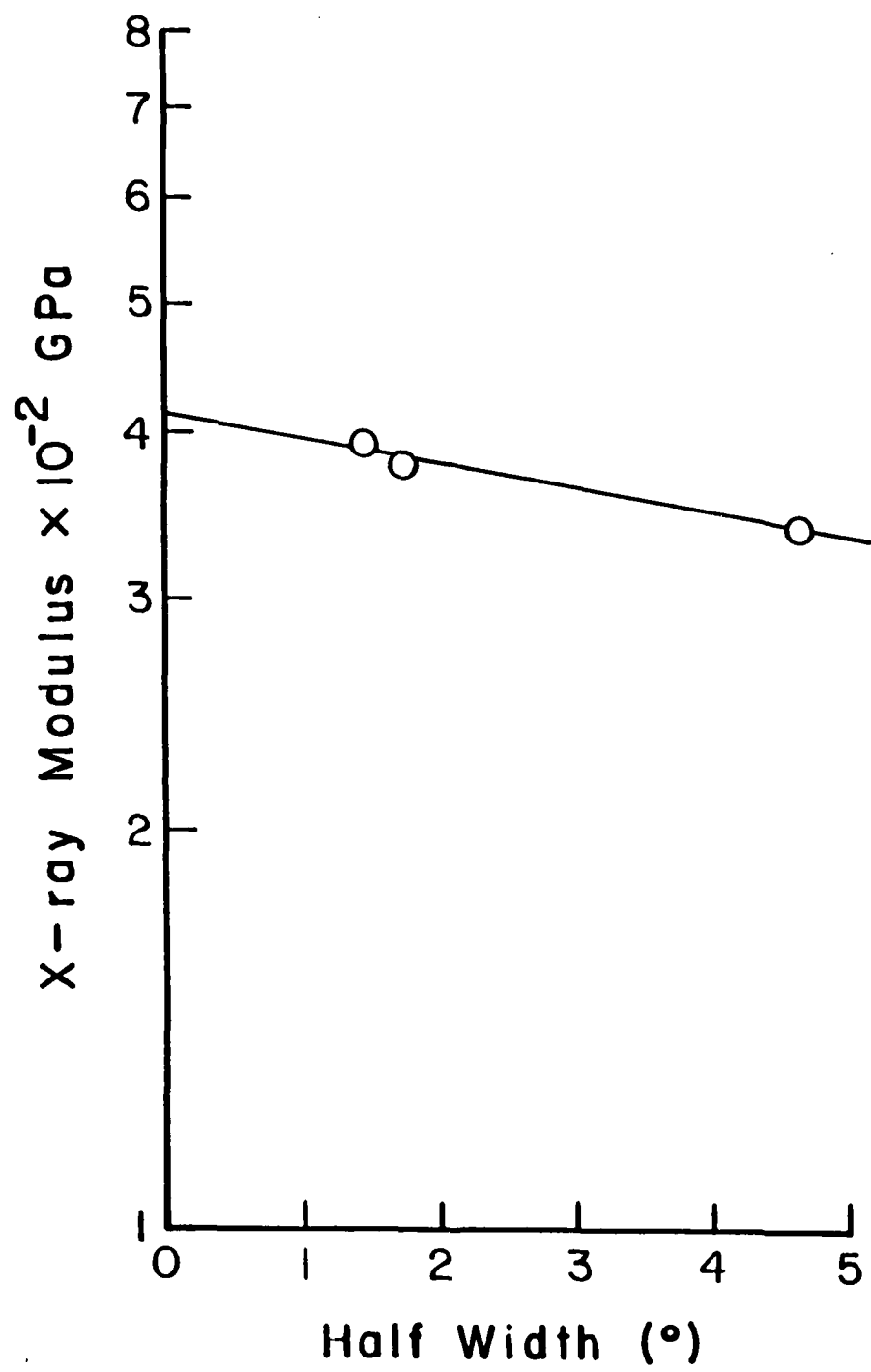


Fig.39 The extrapolation of the curve of half width at half-maximum vs. (log) crystal modulus to obtain the perfect crystal modulus.

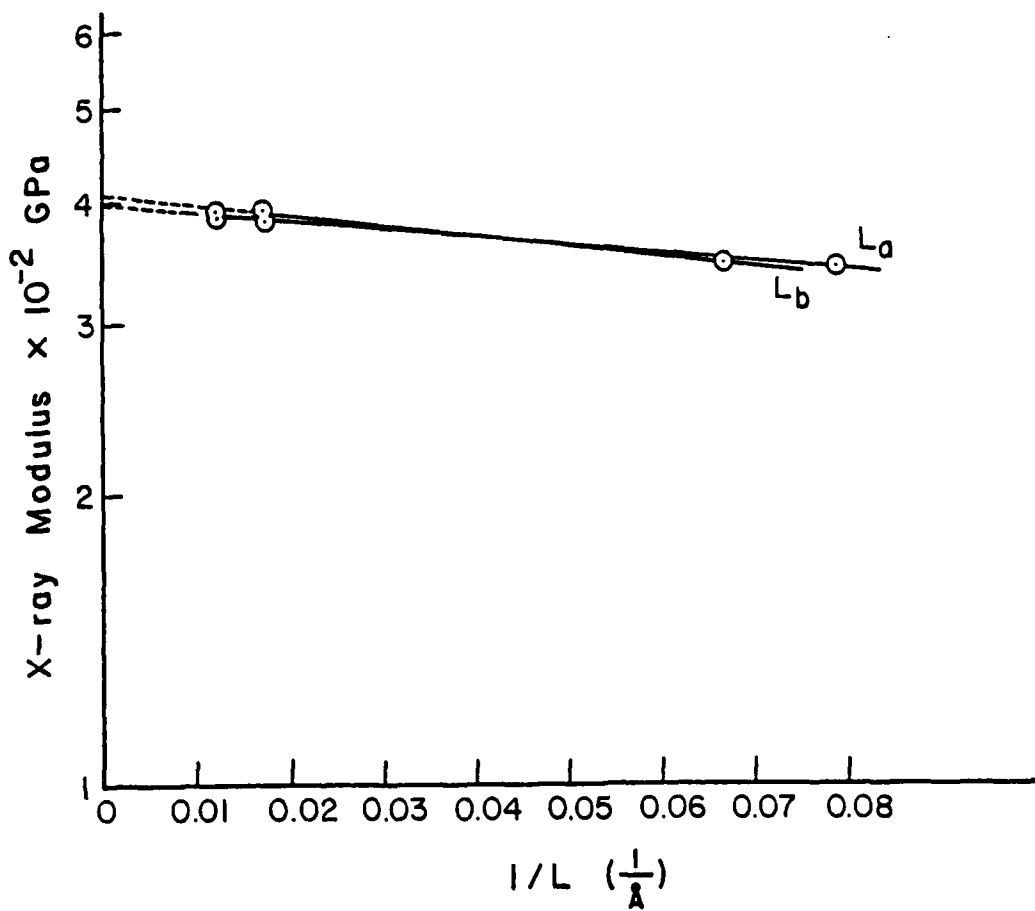


Fig.40 The extrapolation of the curve of reciprocal of crystal size ($1/L$) vs. (log) crystal modulus to obtain the perfect crystal modulus.

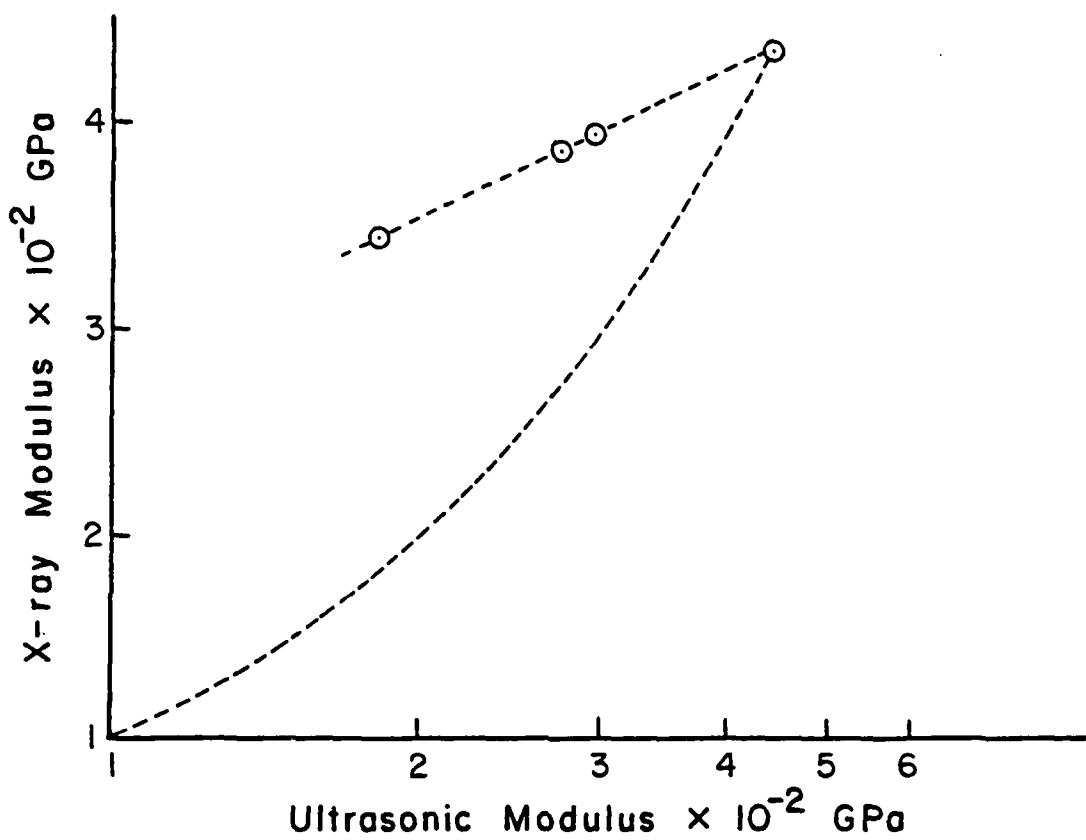


Fig.41 The extrapolation of the curve of crystal modulus vs. (log) ultrasonic modulus to obtain perfect crystal modulus.

$$\epsilon_m = \epsilon_{c_1} = \epsilon_{c_2} = \dots \quad (4-1)$$

where subscript m denotes macroscopic and c denotes crystal. If we treat the fiber as a composite with a distribution of crystal orientations,

$$E_m = \frac{\sigma_m}{\epsilon_m} = \frac{\sigma_m}{\epsilon_c} = E_c f_a + \frac{E_c}{B} f_b + \frac{E_c}{C} f_c + \dots \quad (4-2)$$

where E_c is the maximum modulus (along the fiber axis); E_c/B , E_c/C , ..., are different moduli at different angles with respect to the fiber axis; f_a , f_b , f_c , ..., are different area fractions at different angles with respect to the orientation axis, which are shown in Figs. 42-4 respectively. So, we obtain

$$E_m = E_c \left(f_a + \frac{f_b}{B} + \frac{f_c}{C} + \dots \right) \quad (4-3)$$

For the uniform strain assumption, modulus E_c is

$$E_c = E_m \frac{1}{\left(f_a + \frac{f_b}{B} + \frac{f_c}{C} + \dots \right)} \quad (4-4)$$

namely,

$$E_c = \frac{\sigma_m}{\epsilon_c} \frac{1}{\left(f_a + \frac{f_b}{B} + \frac{f_c}{C} + \dots \right)} \quad (4-5)$$

In fact, the term (σ_m/ϵ_c) is the modulus of the uniform stress model, (i. e. the previously determined modulus). Thus, from the $E - \theta$ (or $E - \alpha$) curve (Figs. 43 and 44) we could get E_c , E_c/B , ..., and furthermore the B , C , ..., and from

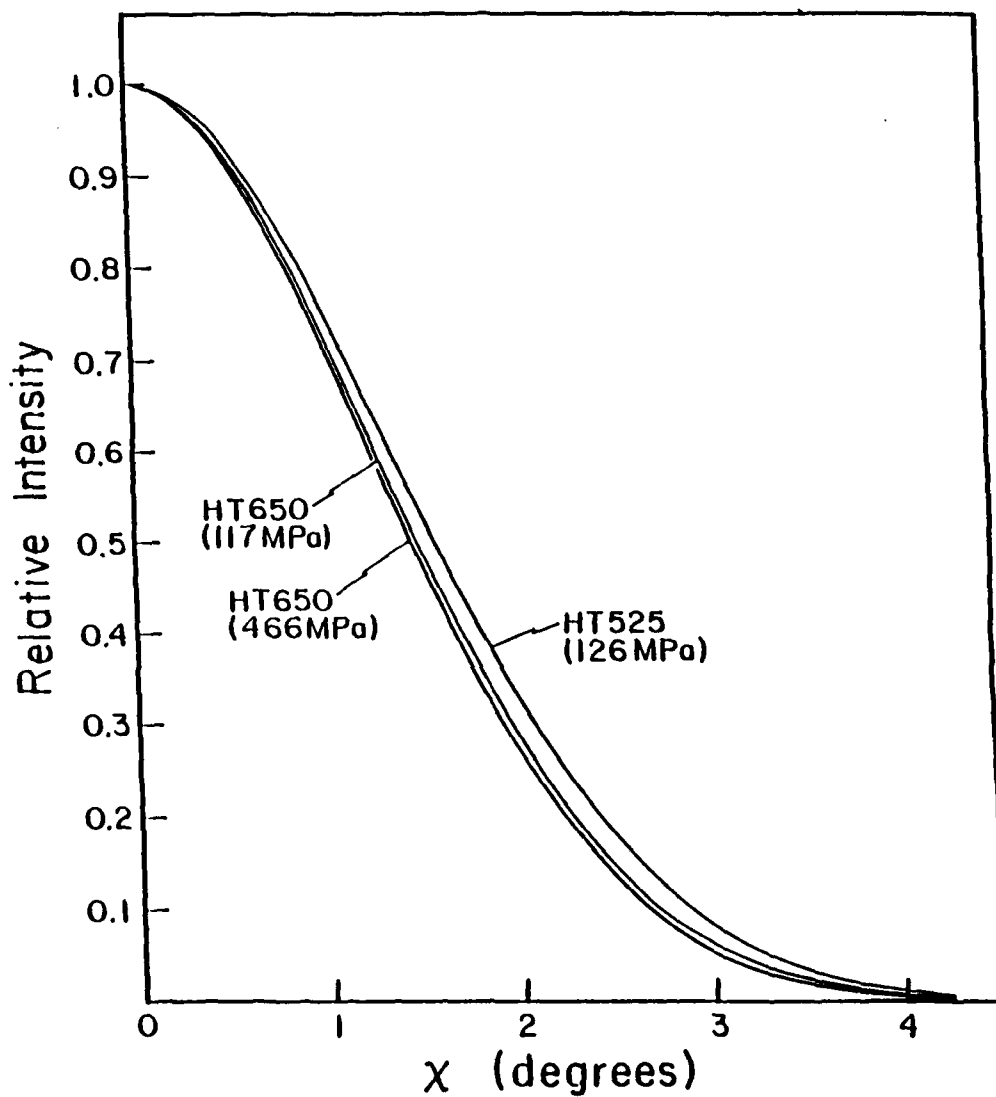


Fig.42 The comparison of the $I - \chi$ curves of two fiber samples (HT-525 and HT-650) under different tensile stresses.

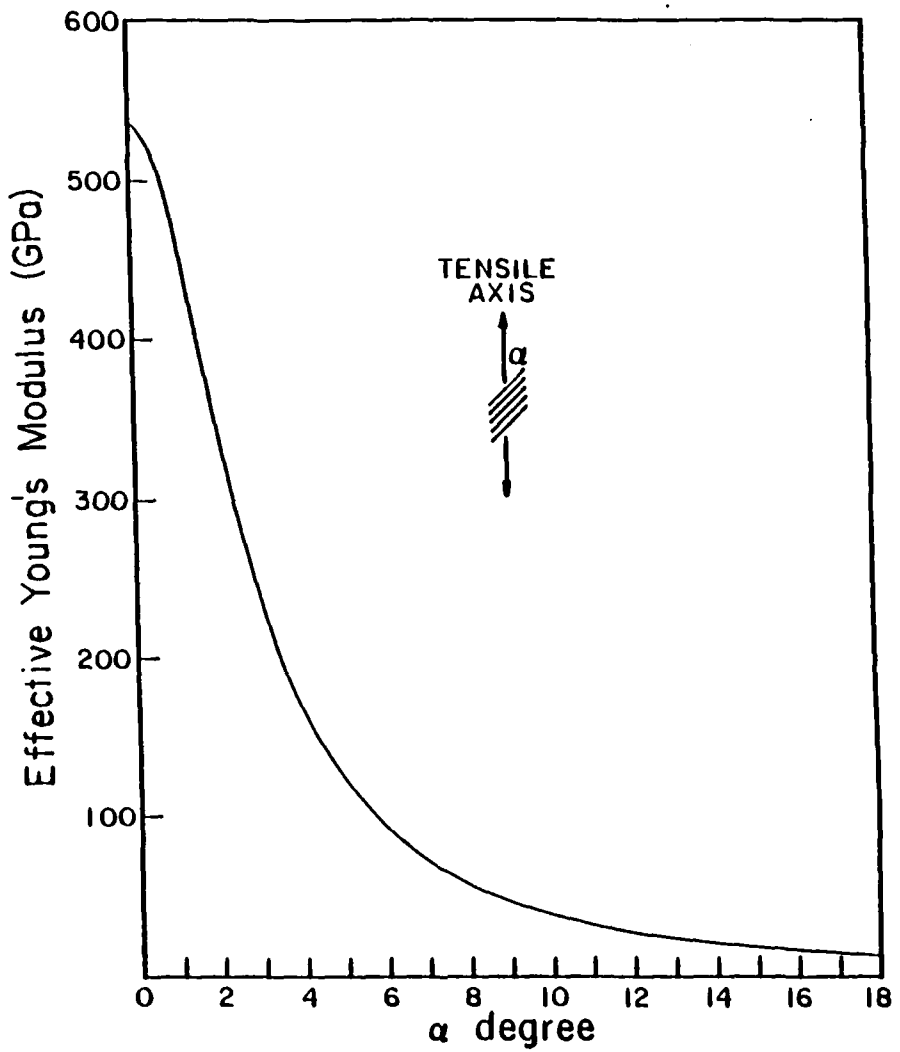


Fig.43 The schematic diagram of the effect of orientation angle α (or called as θ) on the effective Young's modulus for a PBZT single crystal.

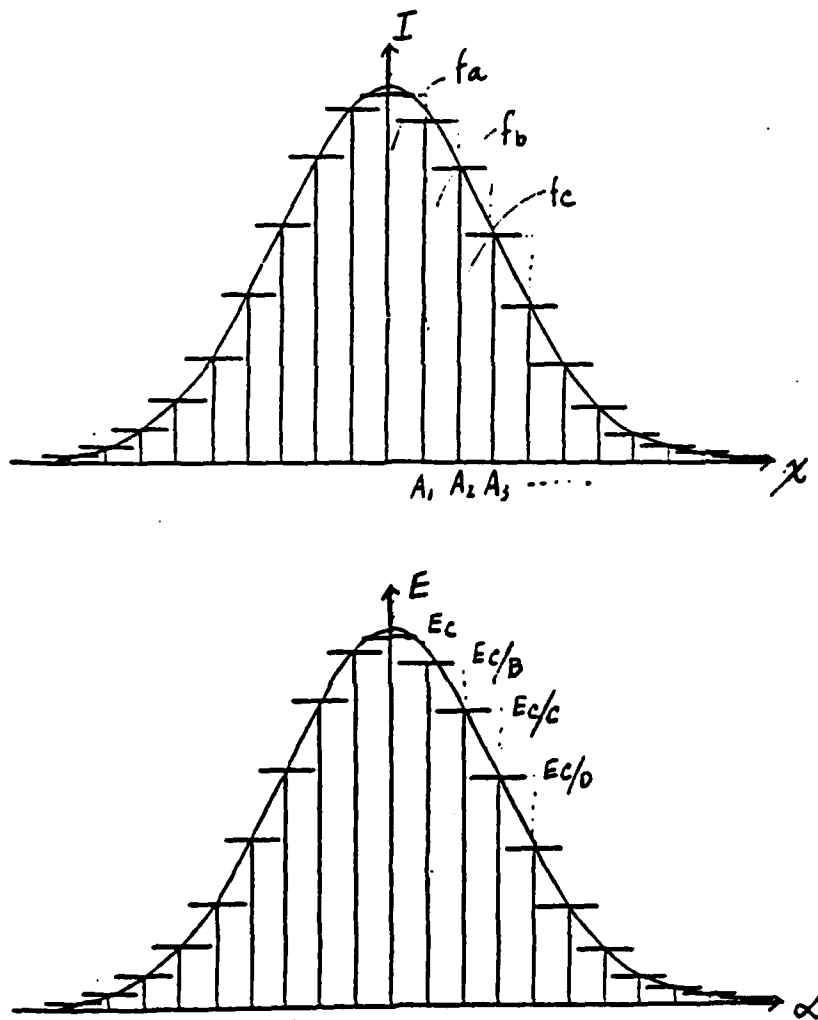


Fig.44 The choices of f_a, f_b, f_c, \dots , in the $I - \chi$ orientation distribution curve and $E_c, E_c/B, E_c/C, \dots$, in the $E - \alpha$ (or called as $E - \theta$) effective Young's modulus curve.

the $I - \chi$ curve Figs. 42 and 44) we could get f_a , f_b , So, by means Eqn.(4-5), the E_c for uniform strain assumption can be calculated.

There is one more thing we must consider. Since the elasticity of a single crystal depends on the direction of applied stress, the effective Young's modulus E for a given angle between the crystal b axis (which was chosen as the unique axis) and the tensile axis should be calculated through a series of matrix calculations. For PBZT crystals, the following steps should be taken:

(1) To obtain the s_{ij}

The PBZT unit cell is monoclinic one. Its compliance matrix has 13 constants if b axis is chosen as the fiber axis[66]:

$$\begin{bmatrix} s_{11} & s_{12} & s_{13} & 0 & s_{15} & 0 \\ s_{12} & s_{22} & s_{23} & 0 & s_{25} & 0 \\ s_{13} & s_{23} & s_{33} & 0 & s_{35} & 0 \\ 0 & 0 & 0 & s_{44} & 0 & s_{46} \\ s_{15} & s_{25} & s_{35} & 0 & s_{55} & 0 \\ 0 & 0 & 0 & s_{46} & 0 & s_{66} \end{bmatrix} \quad (4-6)$$

(2) To obtain transformation matrix

In order to consider different orientations of the crystal in the stress field, the rotation matrix should be calculated in terms of Eulerian angles (Eqn. 2-12).

The transformation matrix, N , is

[N] =

$$\begin{bmatrix} \omega_{11}^2 & \omega_{12}^2 & \omega_{13}^2 & \omega_{12}\omega_{13} & \omega_{13}\omega_{11} & \omega_{11}\omega_{12} \\ \omega_{21}^2 & \omega_{22}^2 & \omega_{23}^2 & \omega_{22}\omega_{23} & \omega_{23}\omega_{21} & \omega_{21}\omega_{22} \\ \omega_{31}^2 & \omega_{32}^2 & \omega_{33}^2 & \omega_{32}\omega_{33} & \omega_{33}\omega_{31} & \omega_{31}\omega_{32} \\ 2\omega_{21}\omega_{31} & 2\omega_{22}\omega_{32} & 2\omega_{23}\omega_{33} & \omega_{22}\omega_{33} + \omega_{23}\omega_{32} & \omega_{21}\omega_{33} + \omega_{23}\omega_{31} & \omega_{22}\omega_{31} + \omega_{21}\omega_{32} \\ 2\omega_{31}\omega_{11} & 2\omega_{32}\omega_{12} & 2\omega_{33}\omega_{13} & \omega_{12}\omega_{33} + \omega_{13}\omega_{32} & \omega_{13}\omega_{31} + \omega_{11}\omega_{33} & \omega_{11}\omega_{32} + \omega_{12}\omega_{31} \\ 2\omega_{11}\omega_{21} & 2\omega_{12}\omega_{22} & 2\omega_{13}\omega_{23} & \omega_{12}\omega_{23} + \omega_{13}\omega_{22} & \omega_{13}\omega_{21} + \omega_{11}\omega_{23} & \omega_{11}\omega_{22} + \omega_{12}\omega_{21} \end{bmatrix}$$

Because

$$[s'] = [N] [s] [\bar{N}] \quad (4-8)$$

where [s'] is the transformed compliance matrix; [\bar{N}] is the transposed matrix of [N].

Normally, for a single crystal, three rotations should be taken into account if we use the Eulerian relation (described at chapter two). Then for a monoclinic crystal, after rotating around the 2 axis (chosen as the unique axis), the second rotation around the 1 axis would lead to the same results as the second rotation around the 3 axis. Therefore, only two rotations should be considered for a PBZT crystal since it is a monoclinic one. One is a rotation

about the 2 axis (the unique axis, expressed by angle ϕ) and the other, rotation about 1 or 3 axis (expressed by angle θ or α).

For the PBZT single crystal, we obtain

$$\begin{aligned}
 s'_{22} = & \sin^4\theta \sin^4\phi s_{11} + \frac{1}{2} \sin^2 2\theta \sin^2\phi s_{12} + \frac{1}{2} \sin^4\theta \sin^2 2\phi s_{13} - \\
 & \frac{1}{2} \sin^4\theta \sin^2\phi \sin 2\phi s_{15} + \cos^2\theta s_{22} + \frac{1}{2} \sin^2 2\theta \cos^2\phi s_{23} - \frac{1}{4} \sin^2 2\theta \sin 2\phi s_{25} \\
 & + \sin^4\theta \cos^4\phi s_{33} - \sin^4\theta \cos^2\phi \sin 2\phi s_{35} + \frac{1}{4} \sin^2\theta \cos^2\phi s_{44} \\
 & - \frac{1}{4} \sin^2 2\theta \sin 2\phi s_{46} + \frac{1}{4} \sin^4\theta \sin^2 2\phi s_{55} + \frac{1}{4} \sin^2 2\theta \sin^2\phi s_{66} \quad (4-9)
 \end{aligned}$$

Owing to the fact that ϕ is random under the fiber situation, the $E - \theta$ (i.e., $1/s_{22} - \theta$) relation could be easily obtained when all the ϕ positions are averaged. Fig. 45 shows at different ϕ the $E - \theta$ relations.

Eventually, we put this $E - \theta$ relation into Eqn.(4-5), and the uniform strain modulus for the PBZT crystal was determined. We chose 18 fractions in the $E - \theta$ and $I - \chi$ curves for the as-spun PBZT fibers and 7 fractions for the HT fibers. The resulting values of $1/s_{22}$ are shown on Fig. 46 together with the values obtained with the assumption of uniform stress. For uniform strain, the value for as-spun fiber samples, $E_c = 408$ GPa; for HT 525 fiber samples, $E_c = 425$ GPa; for HT 650 fiber samples, $E_c = 430$ GPa.

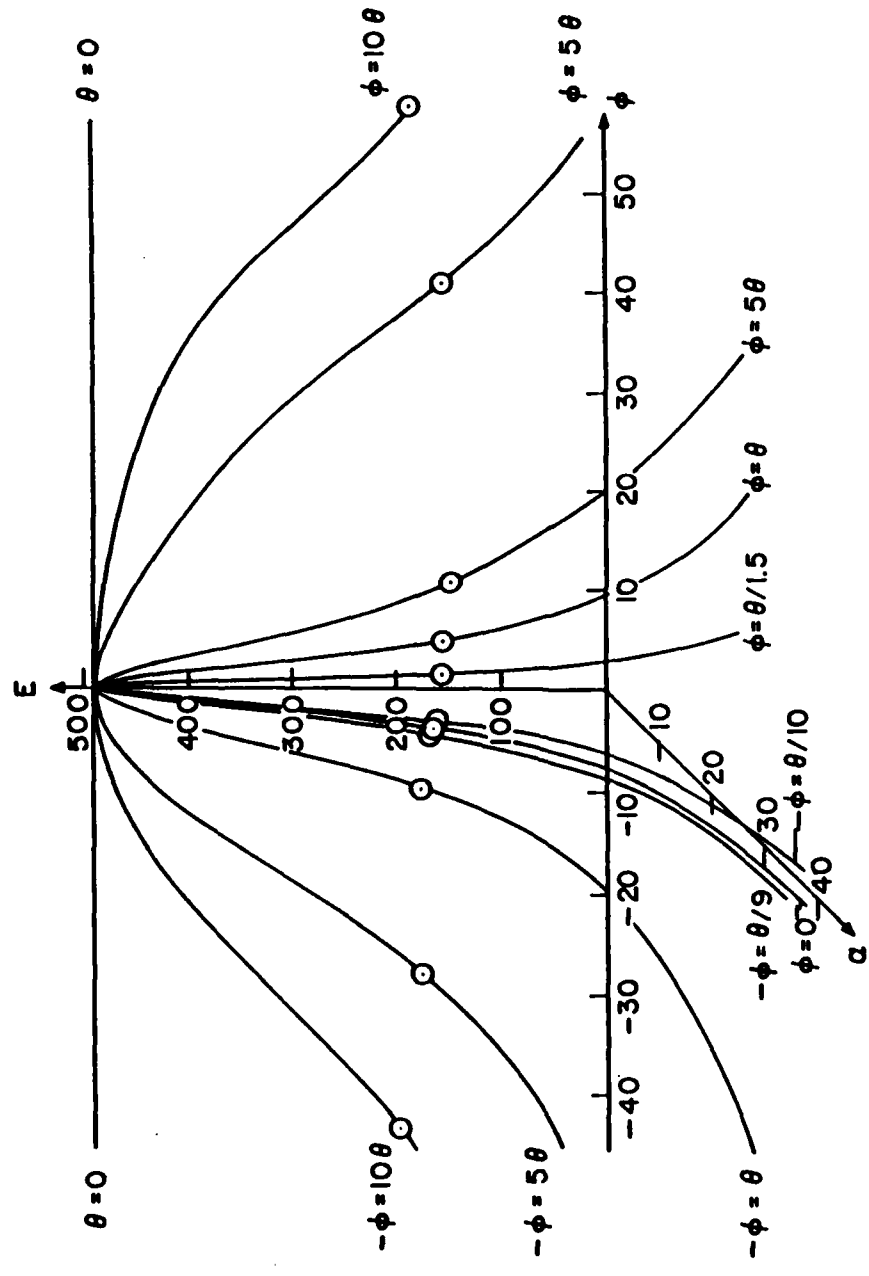


Fig.45 The $E - \alpha$ (or called as $E - \theta$) curves at different ϕ angles.

As to be expected, the value for the uniform strain assumption are greater than those based on uniform stress. As the orientation improves, the uniform stress moduli increase faster than the uniform strain moduli, and the two sets of data approach each other.

4.2.2 Uniform Stress and Uniform Strain Assumptions for PBZT

Fibers

The macroscopic moduli of polycrystalline PBZT fibers were also calculated in conjunction with the assumptions of uniform stress and uniform strain. In the Reuss or uniform stress model, a uniform stress is applied to each crystallite in the direction of the fiber axis. The strain developed in each crystallite will depend on its orientation. It is assumed that the crystallites are strongly linked along the fiber axis and the total fiber strain is the sum of the individual crystallite strains. The compliance of the fiber along the fiber axis, S_{22} , the fiber strain per unit stress, depends on the crystalite compliances and the way in which the crystallites are oriented with respect to the fiber axis.

Owing to

$$\langle S_{ij} \rangle = \frac{\int_0^\pi \int_0^\pi \int_0^{\pi/2} I(\chi, \phi, \psi) s_{ij}(\chi, \phi, \psi) \sin \chi d\chi d\phi d\psi}{\int_0^\pi \int_0^\pi \int_0^{\pi/2} I(\chi, \phi, \psi) \sin \chi d\chi d\phi d\psi} \quad (4-10)$$

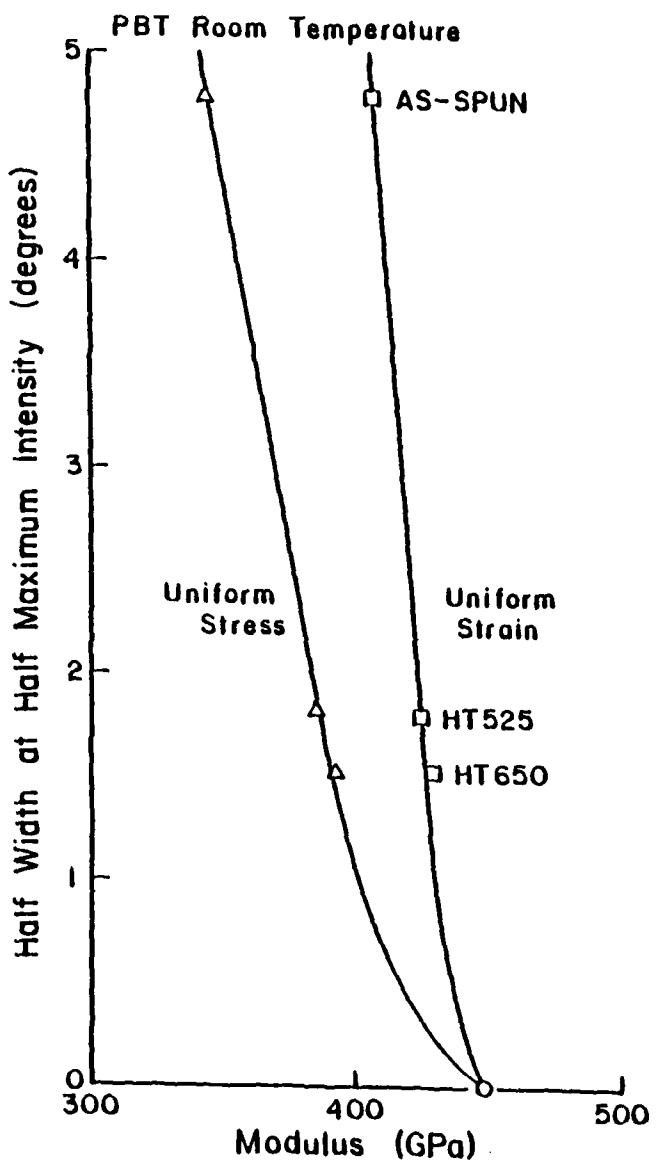


Fig.46 Half-width at half-maximum vs. crystal modulus ($1/s_{22}$) for the assumptions of uniform stress and uniform strain.

Since the fiber symmetry assumption is adopted, namely it is assumed that there is isotropy in a plane perpendicular to the direction of drawing (i. e. the direction of fiber axis), we obtain

$$S'_{22} = s_{22} + [s_{23} + s_{12} - s_{22} + \frac{1}{2} (s_{44} + s_{66})] \frac{I_3}{I_1} + [\frac{3}{8} (s_{33} + s_{11}) + \frac{1}{4} (s_{13} - s_{44}) - s_{12} - s_{23} + s_{22} + \frac{s_{55}}{8} - \frac{s_{66}}{2}] \frac{I_5}{I_1} \quad (4-11)$$

where

$$I_5 = \int_0^{\frac{\pi}{2}} I(\chi) \sin^5 \chi d\chi$$

$$I_3 = \int_0^{\frac{\pi}{2}} I(\chi) \sin^3 \chi d\chi \quad (4-12)$$

$$I_1 = \int_0^{\frac{\pi}{2}} I(\chi) \sin \chi d\chi$$

and $I(\chi)$ is the orientation distribution function. For the uniform stress assumption, the modulus $E_c = 1/S'_{22}$.

In the Voigt or uniform strain model the crystallites are assumed to be interlinked in a manner such that each crystallite is strained by the same amount. The stress developed in each crystallite depends on its orientation and the total fiber stress is the sum of the crystallite stresses. It yields C_{22} , the

fiber stress per unit strain. However, in a static stress-strain experiment only the components of compliance can be measured directly, thus, the resulting modulus should be given by $E_c = 1/S_{22}$. It is necessary to calculate all of the required C_{ij} and invert the matrix of stiffnesses to yield the corresponding compliances. Due to the fiber symmetry, (choosing the 2 axis as the axis of symmetry), the compliance matrix S reduces to

$$\begin{bmatrix} S_{11} & S_{12} & S_{13} & 0 & 0 & 0 \\ S_{12} & S_{22} & S_{12} & 0 & 0 & 0 \\ S_{13} & S_{12} & S_{11} & 0 & 0 & 0 \\ 0 & 0 & 0 & S_{44} & 0 & 0 \\ 0 & 0 & 0 & 0 & S_{44} & 0 \\ 0 & 0 & 0 & 0 & 0 & S_{66} \end{bmatrix} \quad (4-13)$$

where $S_{66} = 2(S_{11} - S_{13})$. Through the relation

$$[S][C] = [I]$$

we obtain

$$S_{22} = \frac{(C_{11} + C_{13})}{C_{22}(C_{11} + C_{13}) - 2C_{12}^2} \quad (4-14)$$

With the same approach described above, the required stiffnesses C_{11} , C_{12} , C_{13} and C_{22} could be calculated as follows:

$$C_{11} = \frac{3}{8} \left[\frac{3}{8} (c_{11} + c_{33}) + \frac{1}{4} (2c_{55} + c_{13}) - c_{12} + c_{22} - c_{23} - 2(c_{44} + c_{66}) \right] \frac{I_5}{I_1}$$

$$\begin{aligned}
 & + \left[\frac{1}{2} (c_{23} - c_{55}) - \frac{3}{8} (c_{11} + c_{33}) - \frac{c_{13}}{4} + c_{44} + c_{66} \right] \frac{I_3}{I_1} \\
 & + \frac{1}{2} \left[\frac{3}{4} (c_{11} + c_{33}) + c_{55} + \frac{c_{13}}{2} \right]
 \end{aligned} \tag{4-15}$$

$$\begin{aligned}
 C_{12} = & \frac{-1}{2} \left[\frac{3}{8} (c_{11} + c_{33}) + \frac{1}{4} (2c_{55} + c_{13}) - c_{12} + c_{22} - c_{23} - 2(c_{44} + c_{66}) \right] \frac{I_5}{I_1} \\
 & + \frac{1}{4} [c_{11} + c_{33} + 2(c_{13} + c_{22}) - 3(c_{12} + c_{23}) - 4(c_{44} + c_{66})] \frac{I_3}{I_1} \\
 & + \frac{1}{2} (c_{12} + c_{23})
 \end{aligned} \tag{4-16}$$

$$\begin{aligned}
 C_{13} = & \frac{1}{8} \left[\frac{3}{8} (c_{11} + c_{33}) + \frac{1}{4} (2c_{55} + c_{13}) - c_{12} + c_{22} - c_{23} - 2(c_{44} + c_{66}) \right] \frac{I_5}{I_1} \\
 & + \frac{1}{2} \left[c_{12} + c_{23} + c_{55} - \frac{3}{2} c_{13} - \frac{1}{4} (c_{11} + c_{33}) \right] \frac{I_3}{I_1} \\
 & + \frac{1}{2} \left[\frac{1}{4} (c_{11} + c_{33}) + \frac{3}{2} c_{13} - c_{55} \right]
 \end{aligned} \tag{4-17}$$

$$\begin{aligned}
 C_{22} = & \left[\frac{3}{8} (c_{11} + c_{33}) + \frac{1}{4} (2c_{55} + c_{13}) - c_{12} + c_{22} - c_{23} - 2(c_{44} + c_{66}) \right] \frac{I_5}{I_1} \\
 & + [c_{12} + c_{23} - 2(c_{22} - c_{44} - c_{66})] \frac{I_3}{I_1} + c_{22}
 \end{aligned} \tag{4-18}$$

The results shown in Figs. 47 and 48 are similar to those in Fig. 35, i. e. the changes of modulus with stress are similar to the corresponding changes in Fig. 35. The experimental values are located between the results based on uniform stress and uniform strain, as is to be expected. However, the calculated values do not exhibit so great an increase of modulus with stress as does

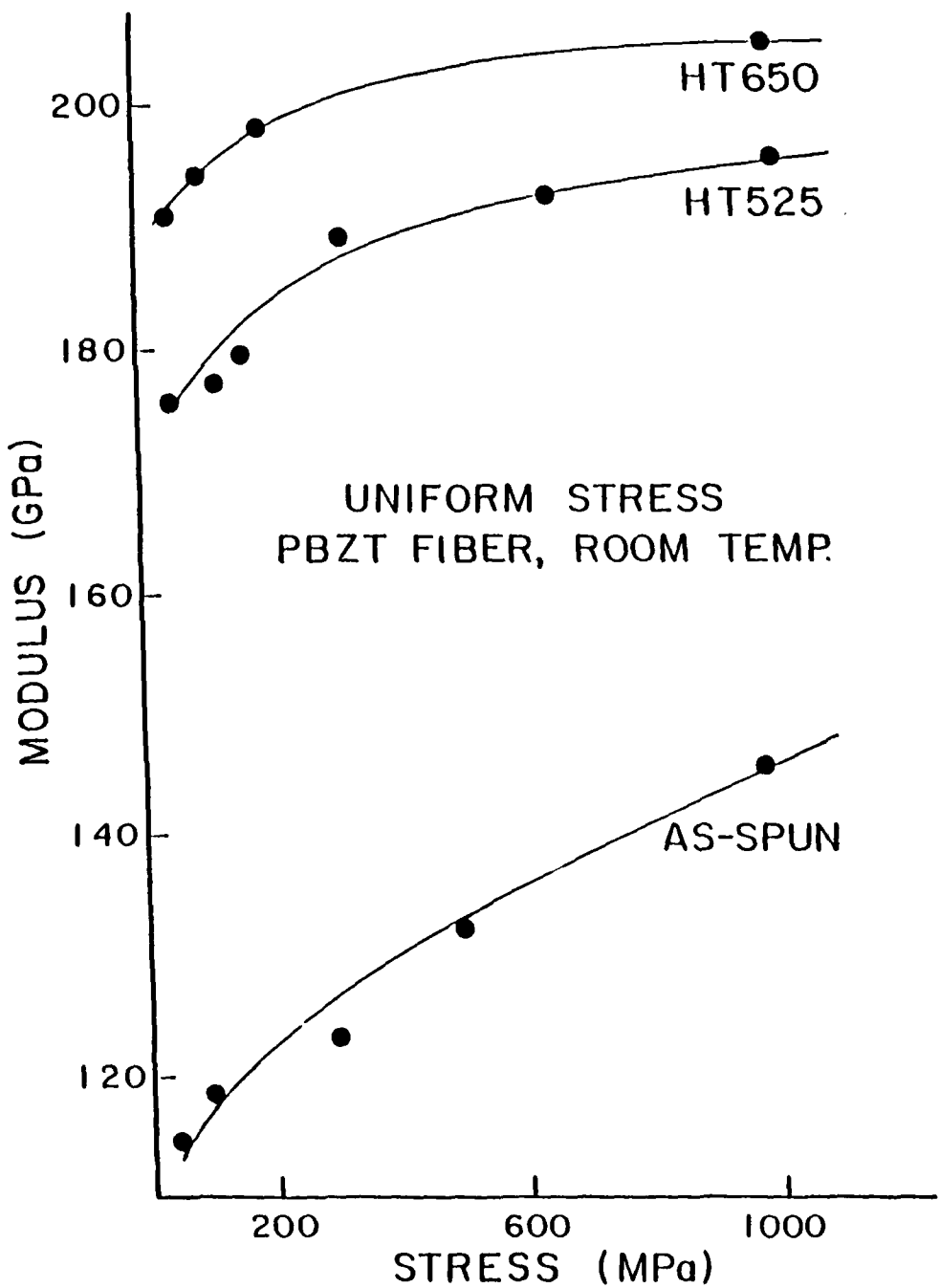


Fig.47 Macroscopic Young's modulus calculated with the assumption of uniform stress as a function of applied tensile stresses.

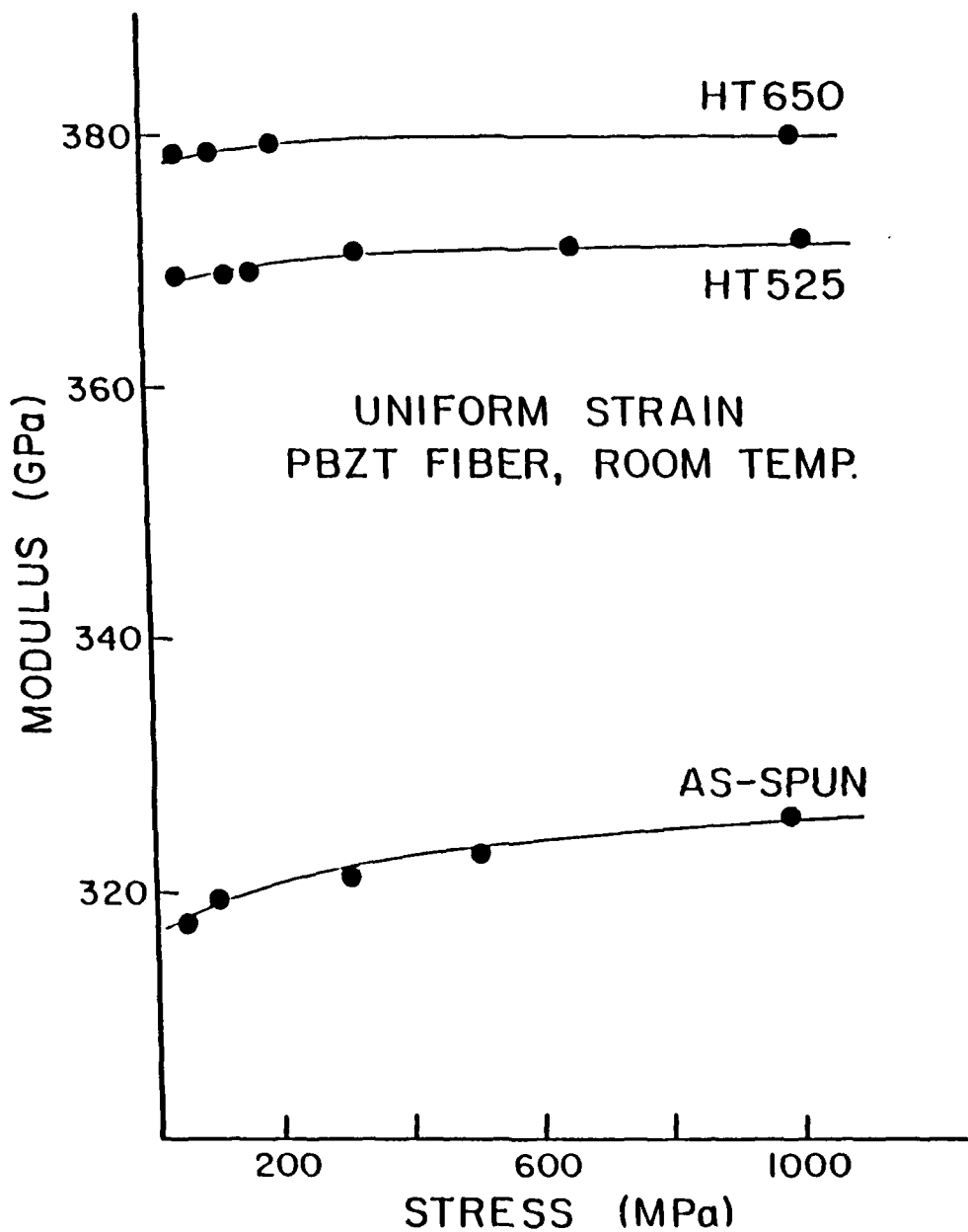


Fig.48 Macroscopic Young's Modulus calculated with the assumption of uniform strain as a function of applied tensile stresses.

the experimental data. To facilitate this comparison, the three sets of data are shown in Figs. 49-51 for the three fiber samples. The smaller change of the calculated modulus compared to the measured modulus is also observed for pitch-based carbon fibers[98]. Some parameters other than orientation are involved. Possibly, crystal size and defects (such as dislocations, vacancies, etc.) play a role. For example, if there is a low temperature (below room temperature) relaxation and if the strength of that relaxation decreases with increasing applied tensile stresses, it would contribute to the nonlinear results of Fig. 35. Such relaxation might involve the motion of dislocations, point-defects, etc., whose populations and locations might be affected by the applied stress, crystal size and regularity, crystal alignment and perfection, etc. Fig. 37 offers some support for this view. Under low stress, the moduli of the heat treated samples fit the curve better than those for the as-spun sample which already deviate from the curve. At high stresses, all deviate. For the heat treated fibers, the crystals are larger, better aligned and have fewer defects than crystals of as-spun fibers. Thus, their dislocations might move less and only under higher stress. Under this circumstance, the crystal alignment would play a more important role.

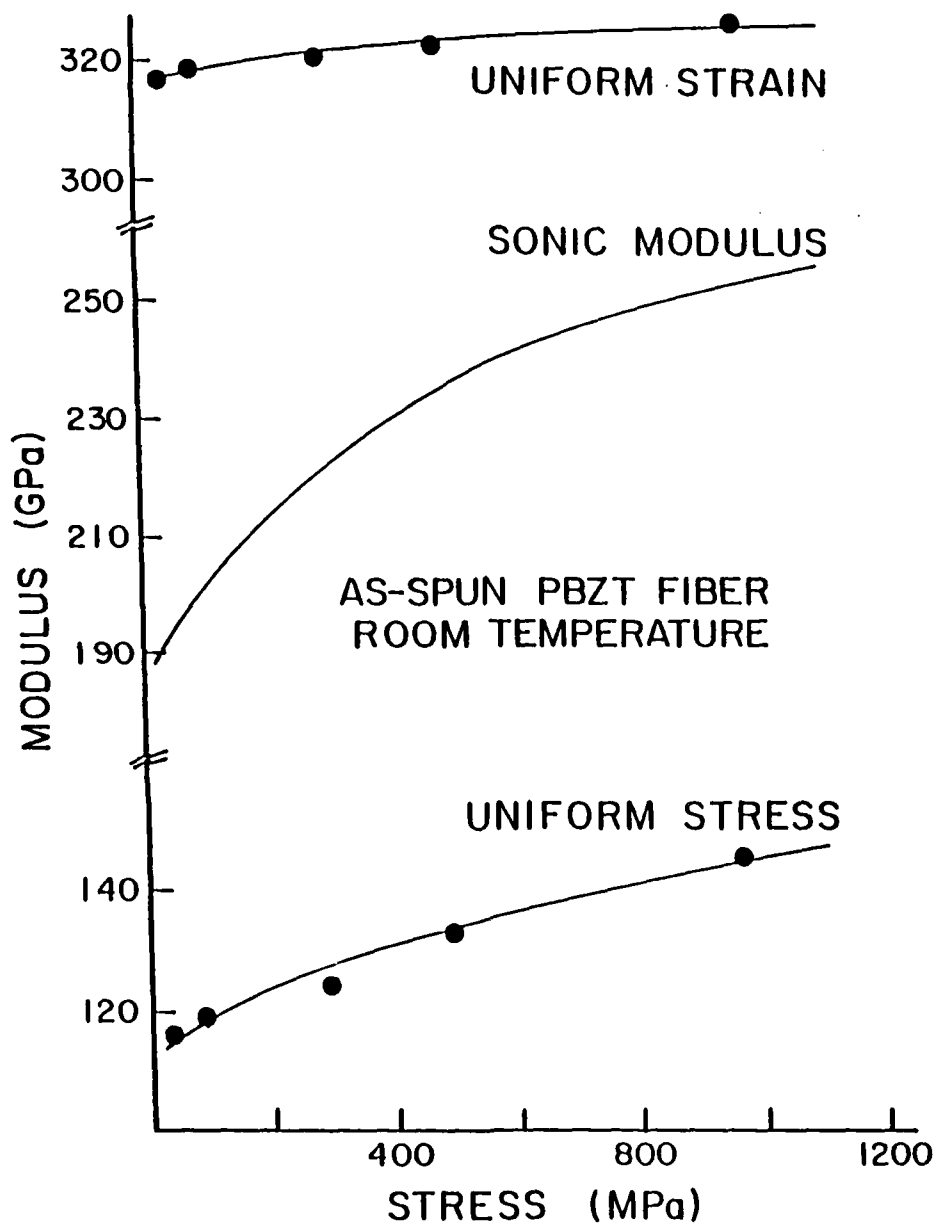


Fig.49 Comparison of measured and calculated Young's moduli as a function of static tensile stresses for the as-spun fibers.

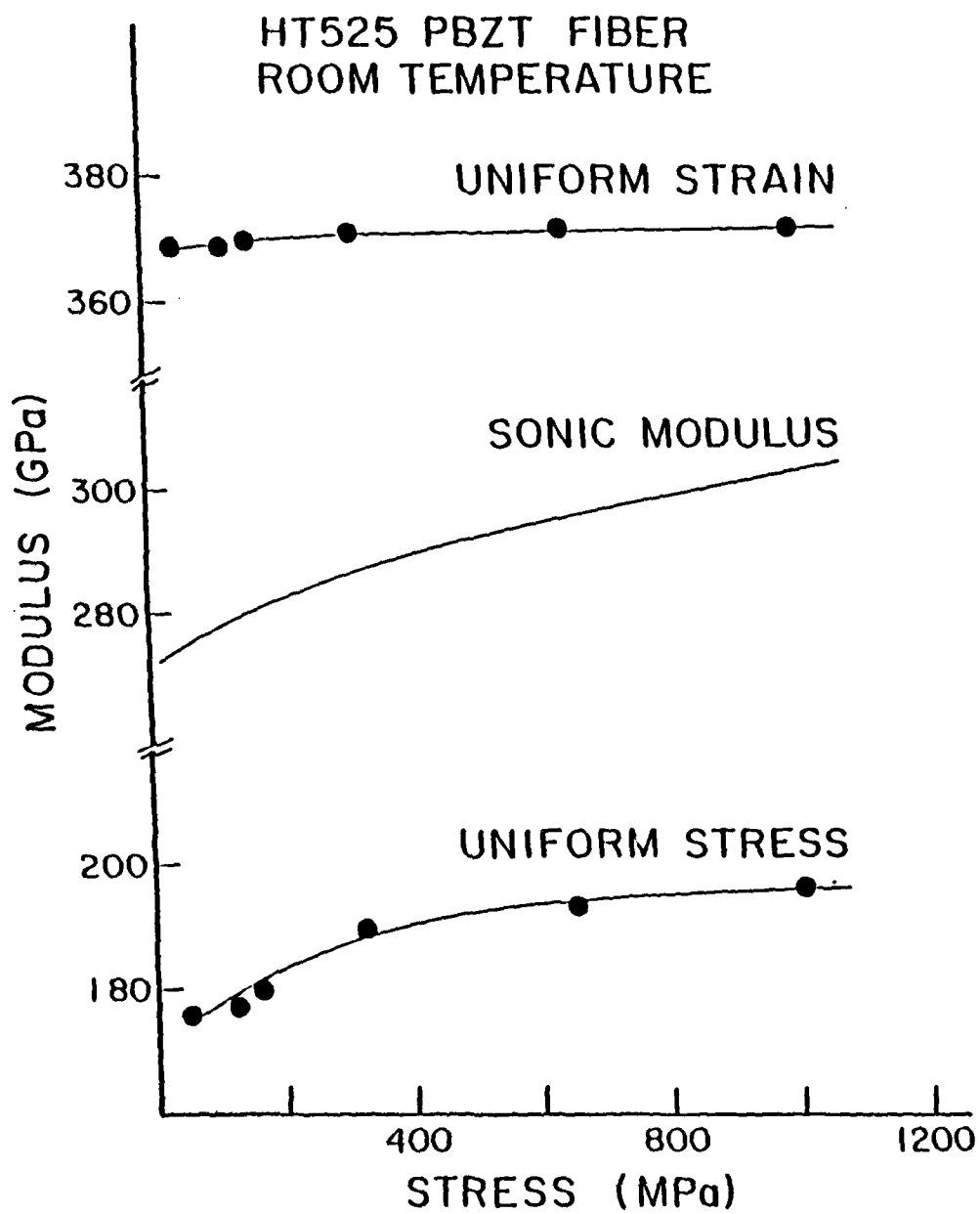


Fig.50 Comparison of measured and calculated Young's moduli as a function of static tensile stresses for the HT-525 fibers.

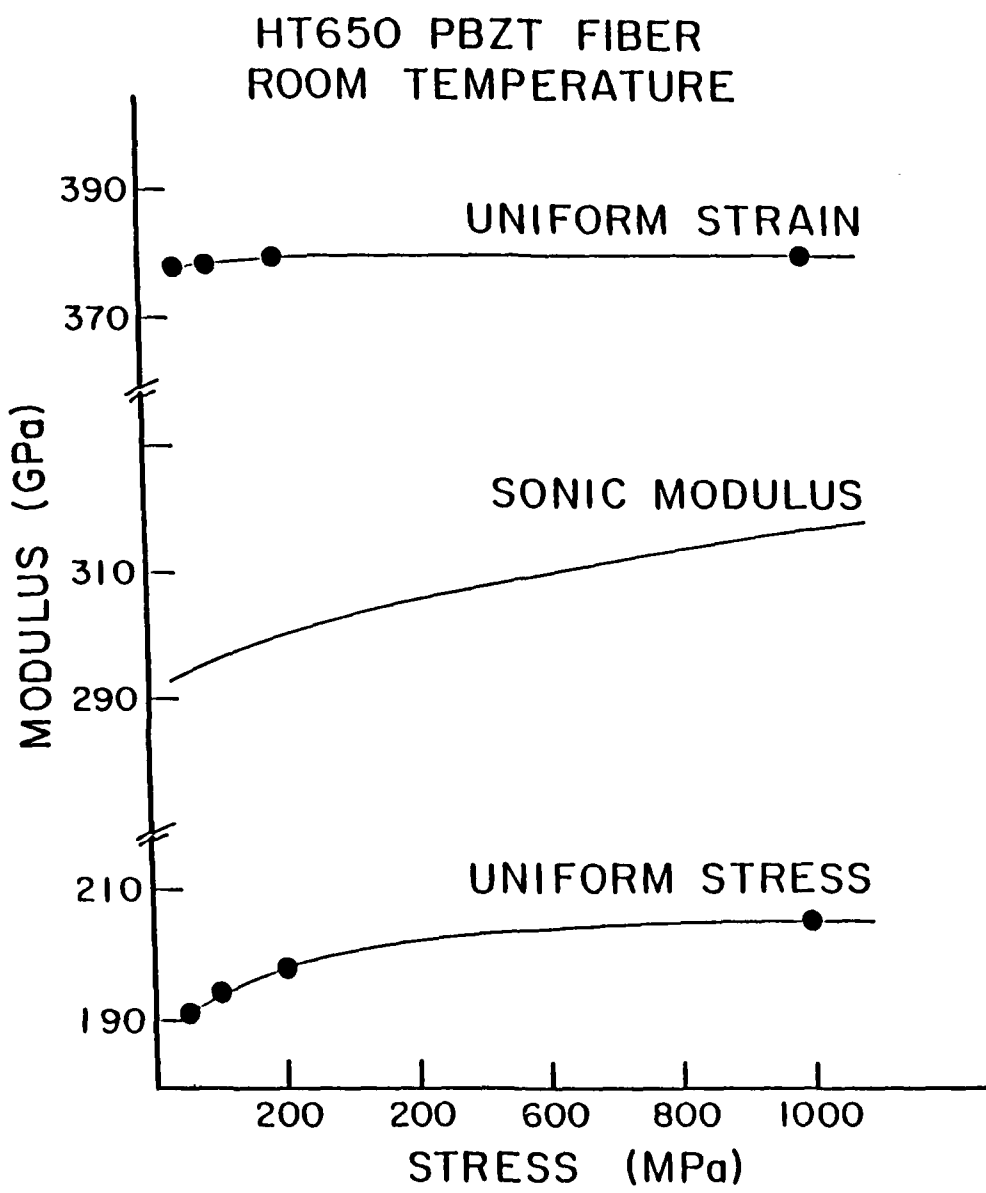


Fig.51 Comparison of measured and calculated Young's moduli as a function of static tensile stresses for the HT-650 fibers.

4.3 Nonlinear Stress-Modulus Behavior at High Temperature

The effect of temperature on the modulus and structure of PBZT fibers is also of great interest. Figs. 52-4 show the modulus vs stress at different temperatures. At high temperature, the nonlinear effect is greater than at low temperature. The data for the as-spun sample are not reversible above 20°C and will not be considered further. The data for the sample heat treated at 525°C are not reversible above about 360°C and those for the sample heat treated at 650°C are not reversible above about 480°C. (The time scale of the measurement is a matter of minutes). Our thermo gravimetric (TG) measurements of the three samples show that at about 300-400°C, there is a little loss in sample weight, which suggests that there is a small amount of residual low molecular weight materials to volatilize[62] (Figs. 55-7). It also indicates that there are no major chemical reactions. But above 500°C, the weight change is gradually apparent. So above this region, the PBZT structure varies by means of oxidation and/or degradation.

There is a similar phenomenon for stress-modulus curves measured at different temperatures. The nonlinear elasticity decreases with increasing tensile stress. Figs. 58-9 show the modulus vs temperature for different stresses.

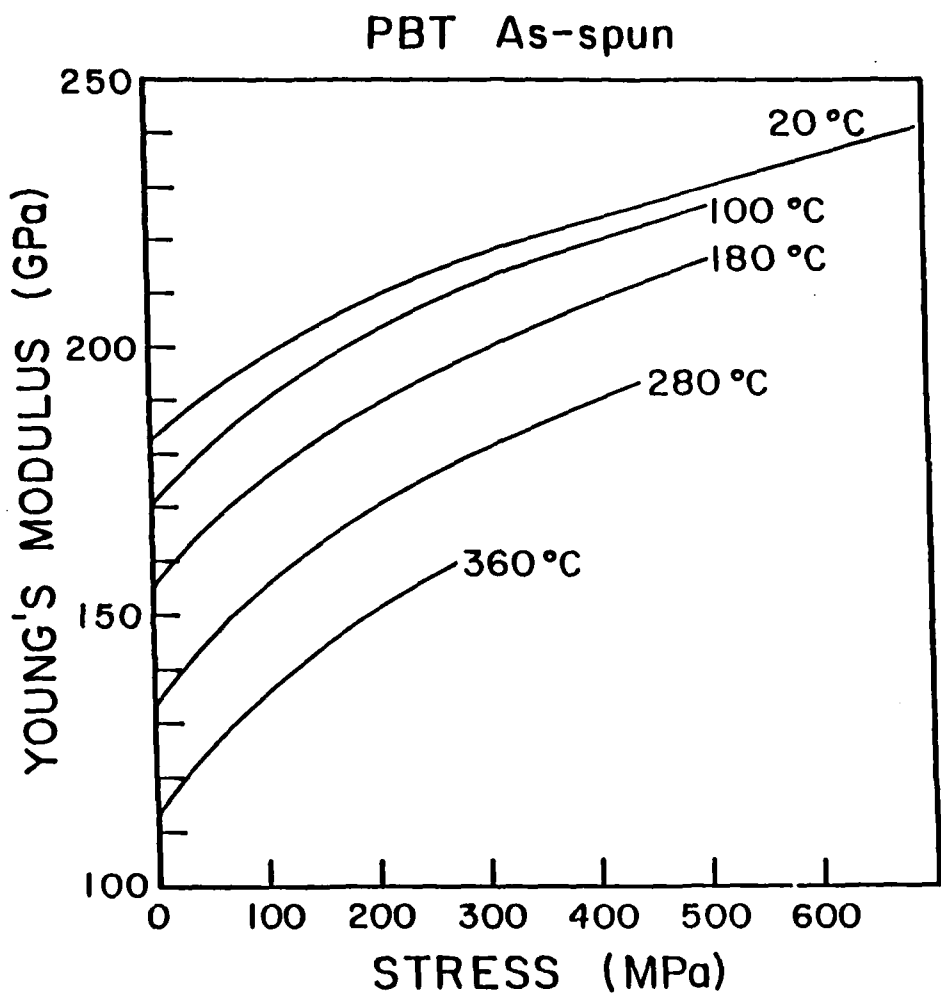


Fig.52 Young's modulus as a function of static tensile stresses at different temperatures for the as-spun fibers.

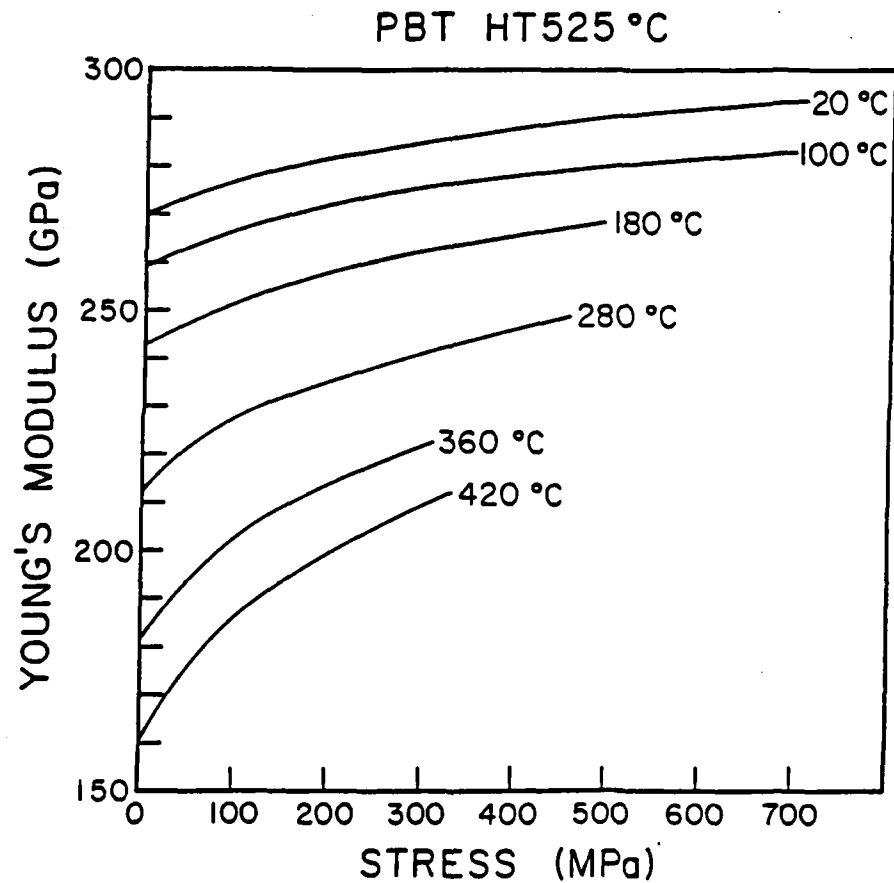


Fig.53 Young's modulus as a function of static tensile stresses at different temperatures for the HT-525 fibers.

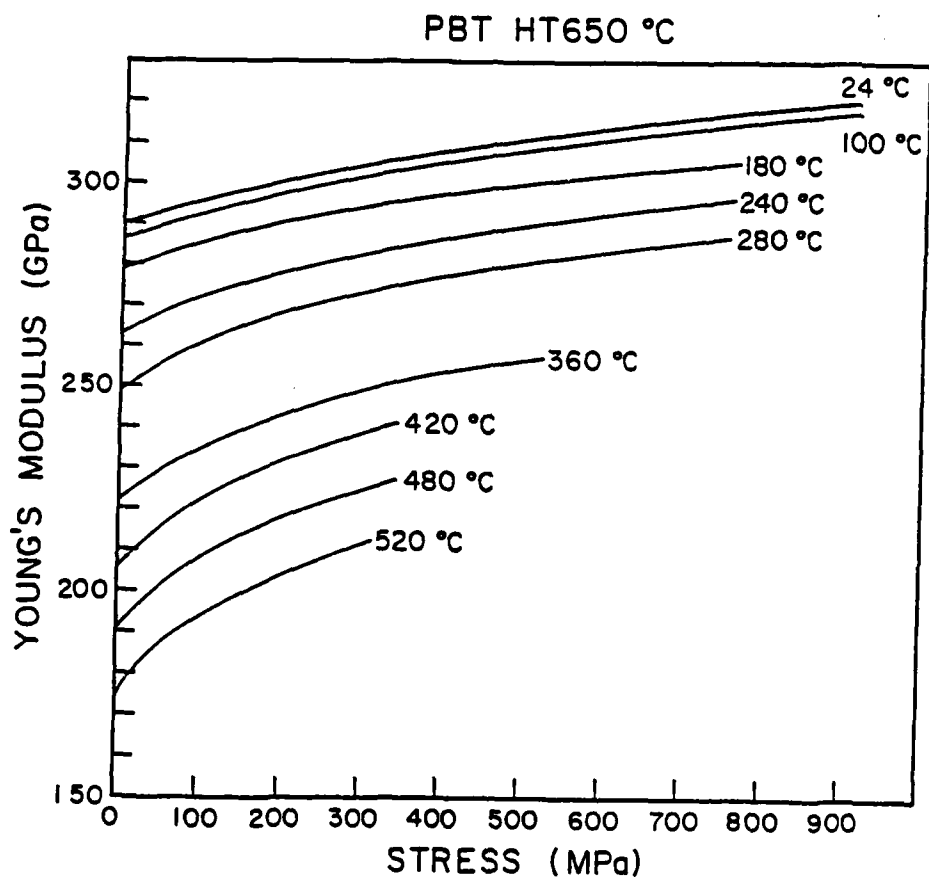


Fig.54 Young's modulus as a function of static tensile stresses at different temperatures for the HT-650 fibers.

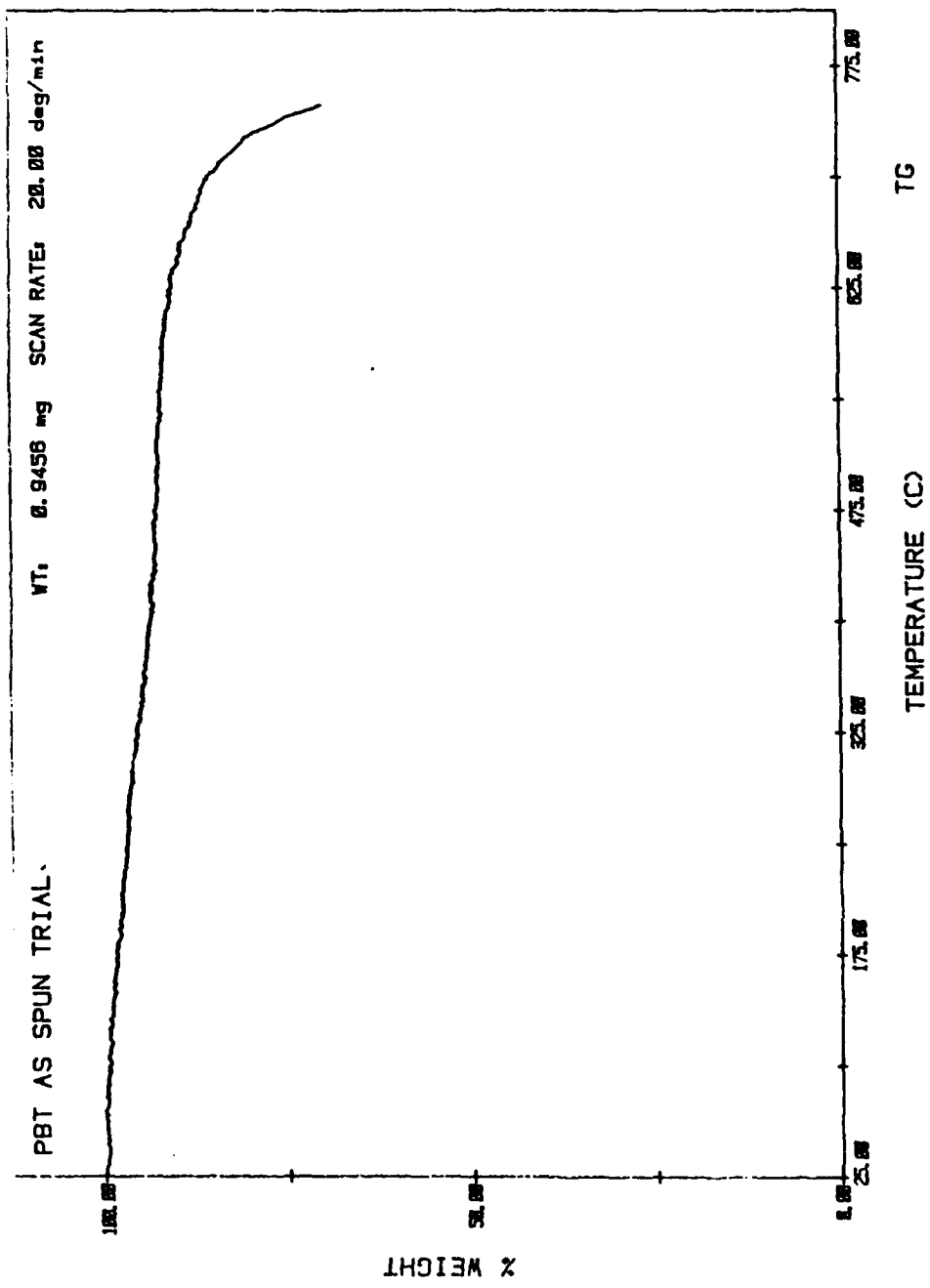


Fig.55 The TG curve for the as-spun PBZT fibers at the scanning rate of 20.0 deg./min.

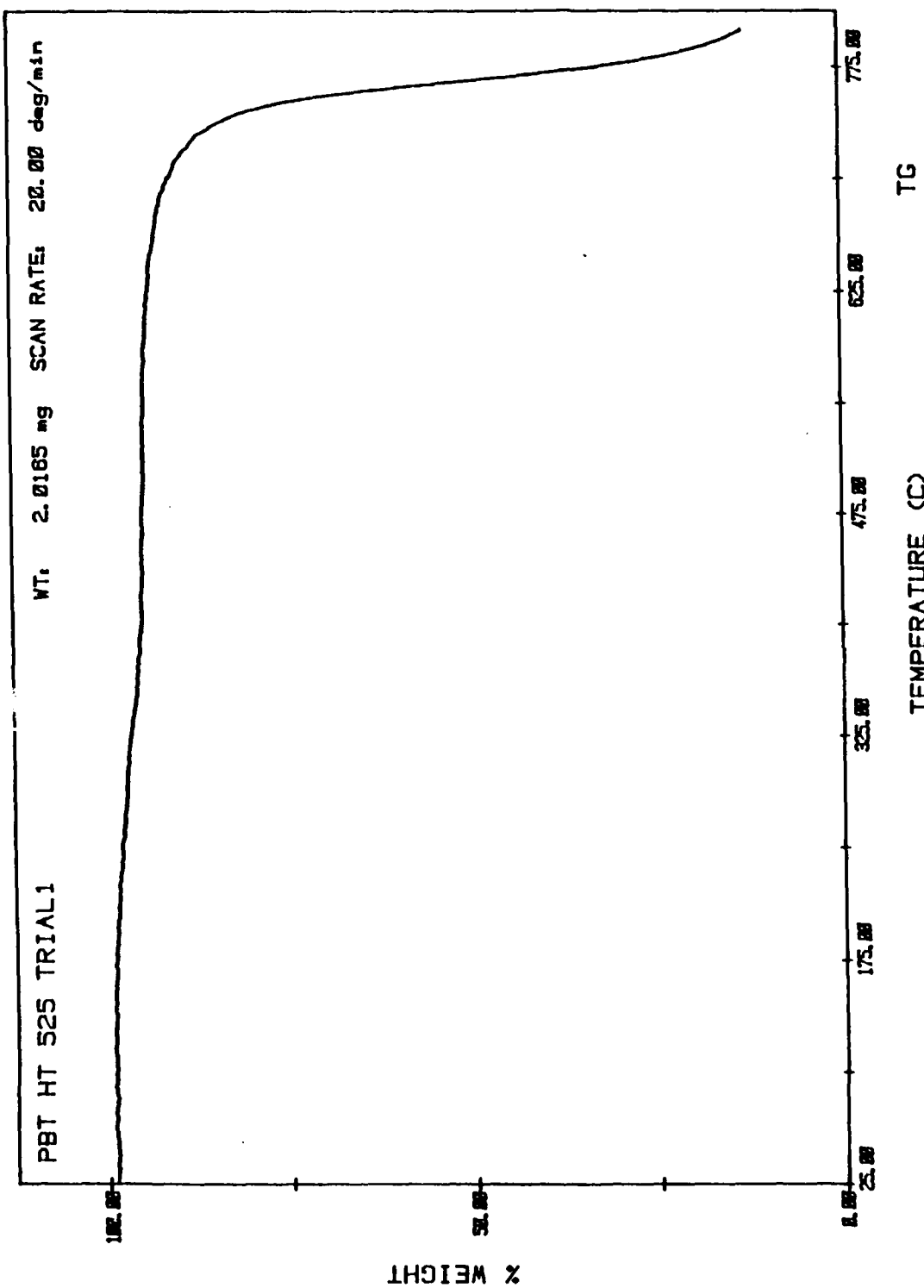


Fig.56 The TG curve for the HT-525 PBZT fibers at the scanning rate of 20.0 deg./min.

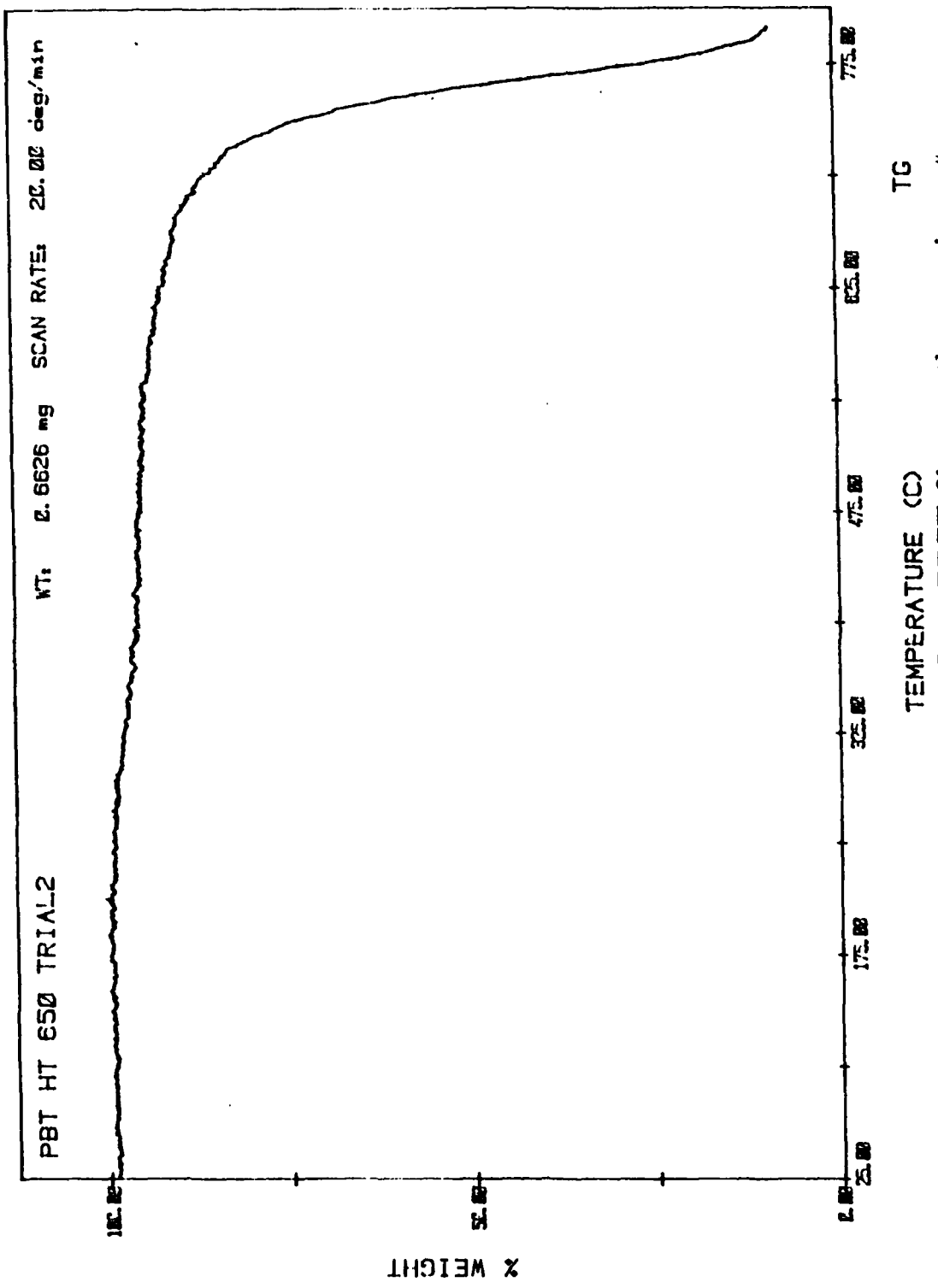


Fig.57 The TG curve for the HT-650 PBZT fibers at the scanning rate of 20.0 deg./min.

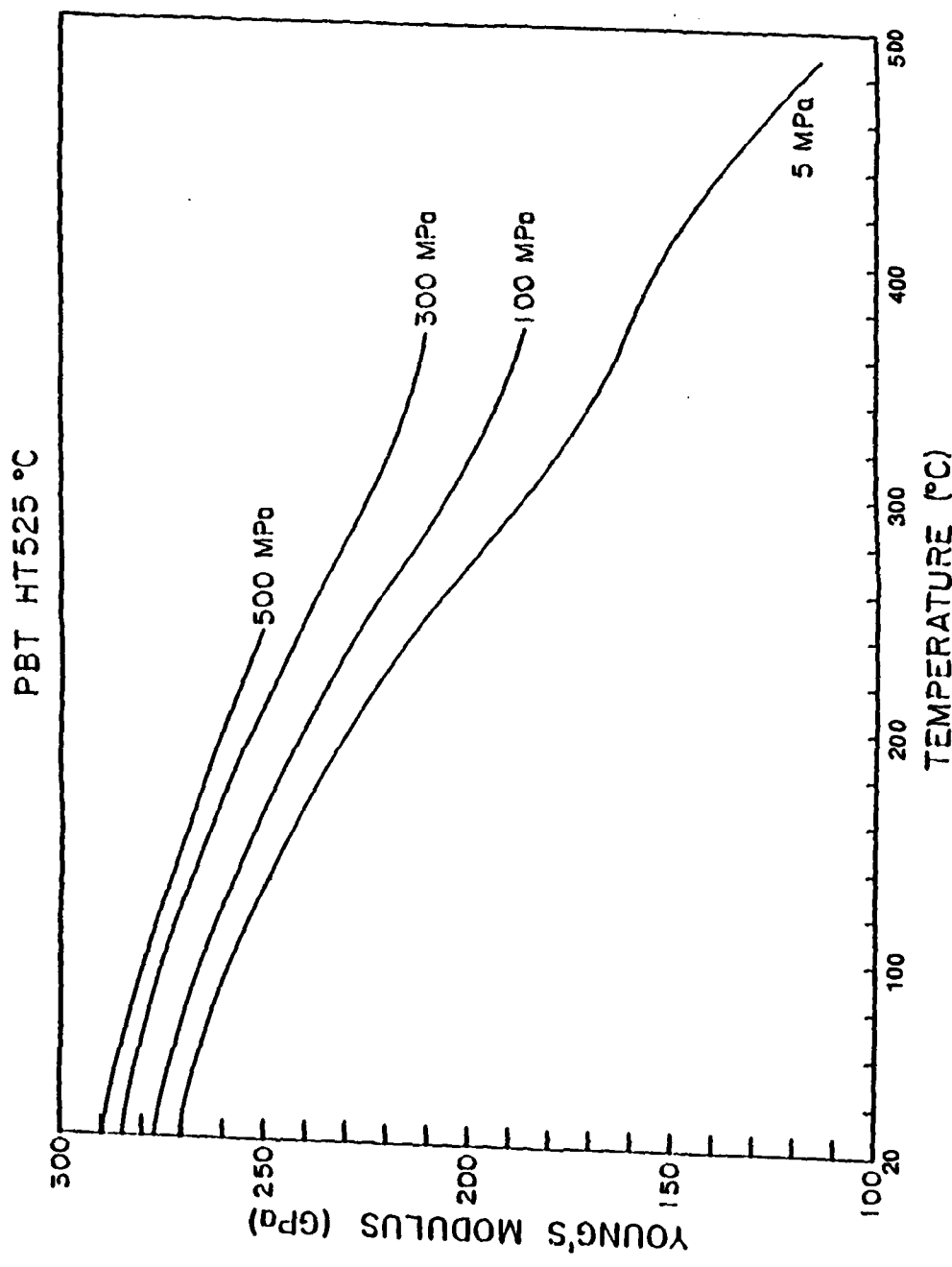


Fig.58 Young's modulus as a function of temperatures at different static tensile stresses for the HT-525 fibers.

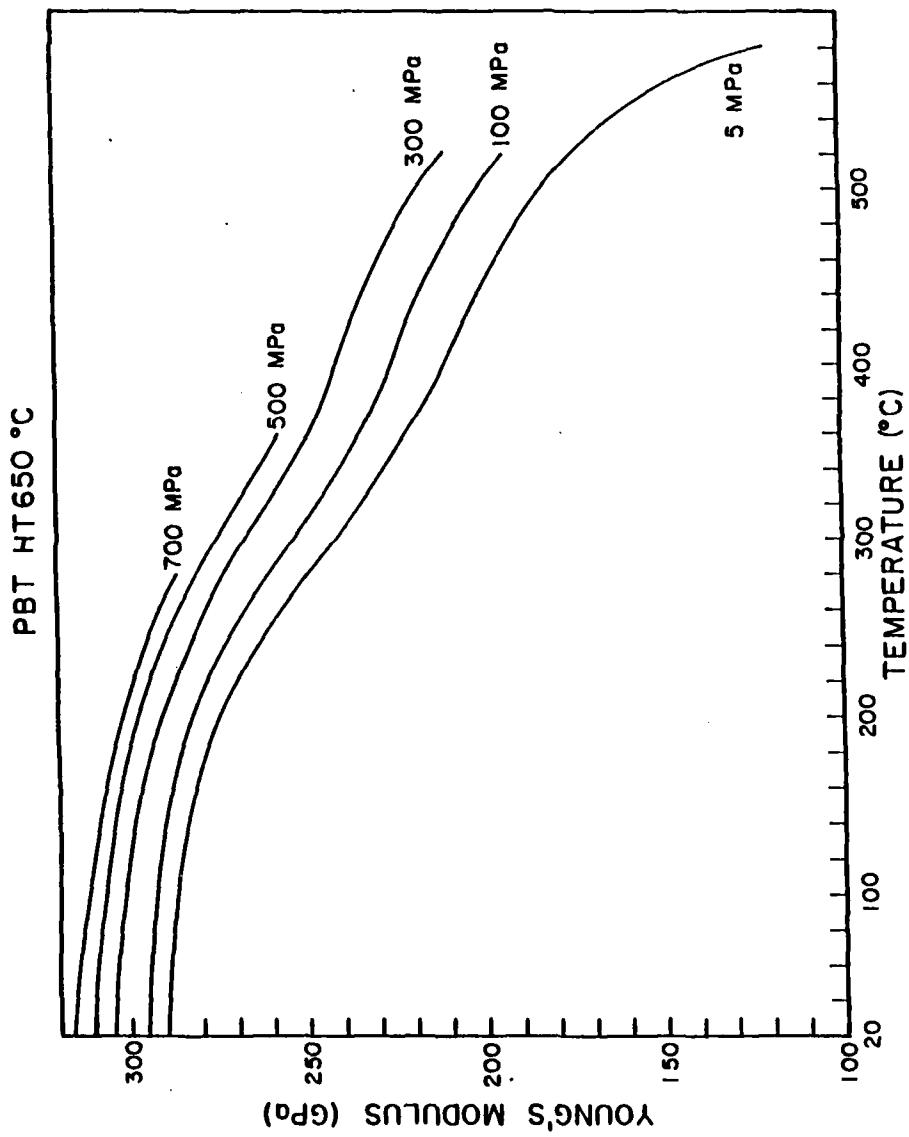


Fig.59 Young's modulus as a function of temperatures at different static tensile stresses for the HT-650 fibers.

With increasing temperature, the modulus drops. Below about 300°C, it decreases nearly linearly with increasing temperature. For the HT fibers, at about 300 to 400°C, there is an inflection with the decrease becoming more gradual. The WAXD data taken with increasing temperature exhibit a structural change in the same temperature range. The variations of the a-axis, b-axis and unit-cell volume also show a slope change at about 300 to 400°C (Fig. 60). Depending upon the temperature, time and tension of any heating, both effects appear to be subject to some irreversibility. The diffraction peak intensity ratio (100/010) (Fig. 61) begins to change markedly in this range. This is caused primarily by the drop of the peak intensity of (010) diffraction profile.

Evidently, the modulus variation in the temperature range 300-400°C is related to a structural variation. During the laser-generated ultrasonic measurements, it was also qualitatively observed that the attenuation of the ultrasonic waves exhibits a peak in the range. This fact suggests that the modulus effects are not associated only with the change in the basal area of the unit cell. Very likely there is a coupling of the applied stress with the molecular motions involved in the structural change. One possible such motion is a conformational oscillation of the molecules. Since the phenyl ring is connected to

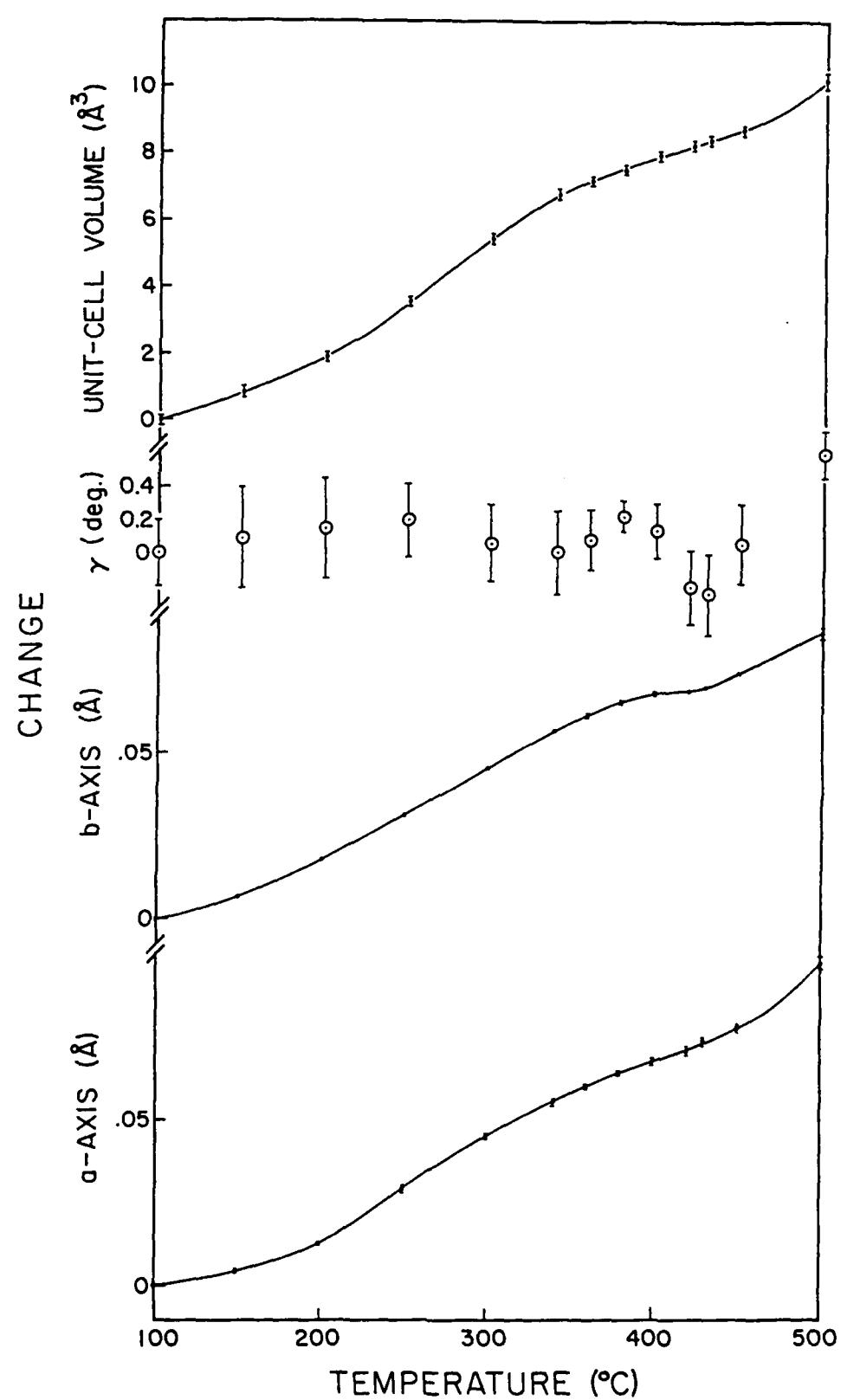


Fig.60 Changes of the a-axis, b-axis, γ and unit-cell volume as a function of temperature for the HT-650 fibers.

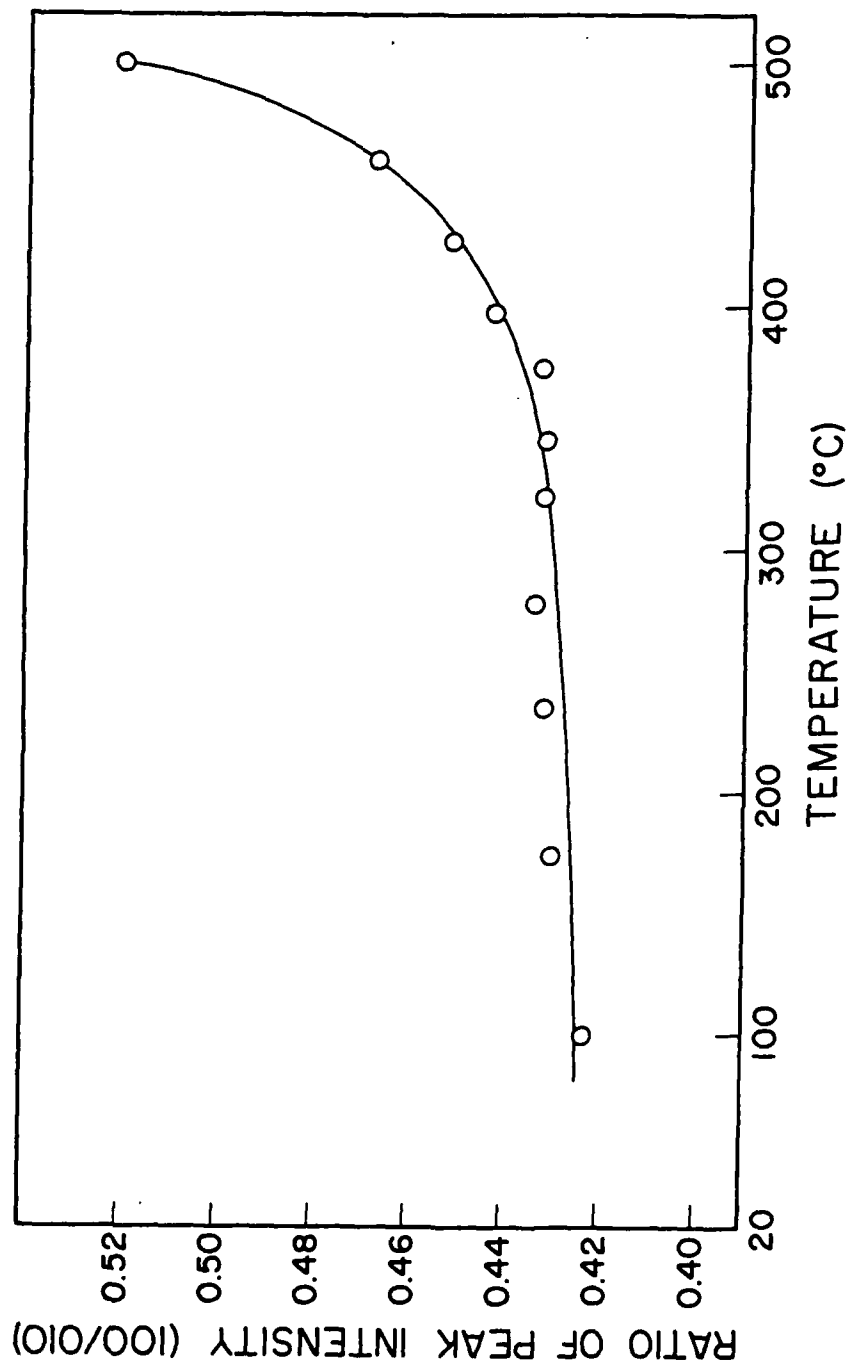


Fig. 61 Ratio of the intensities of the (100) and (010) diffraction peaks as a function of temperatures for the HT-650 fibers.

the bisthiazole moiety with a single bond, the phenyl and the bisthiazole groups may rotate around the single bond with respect to one another in a manner similar to that found in the *para*-phenylenes[100]. When the temperature is raised to about 300 to 400°C, the thermal energy might be high enough to promote the oscillations of the phenyl and the bisthiazole. According to the room-temperature unit cell structure (Fig. 62)[15], the setting angle between the a-axis and the phenyl ring is about 35 deg. and the setting angle between bisthiazole moiety and a-axis is about -5 deg. Therefore, the oscillation would reduce the diffraction intensity from the (010) plane more than that from the (100) plane and the ratio of peak intensities (100/010) would increase. This is exactly the phenomenon shown in Fig. 61. Since it has been calculated that the angle between the phenyl and bisthiazole groups is changed by tensile stress (Fig. 63)[101], there could be a coupling of the oscillation and the ultrasonic waves leading to a mechanical relaxation contributing to the attenuation peak and the modulus decrease in this temperature range. If the initial energy barrier to rotation of the phenyl and bisthiazole groups is overcome by thermal energy, an average planar molecular conformation could appear. As soon as conjugation of a planar structure is formed, it also could contribute to the modulus, and to the delay in modulus decrease

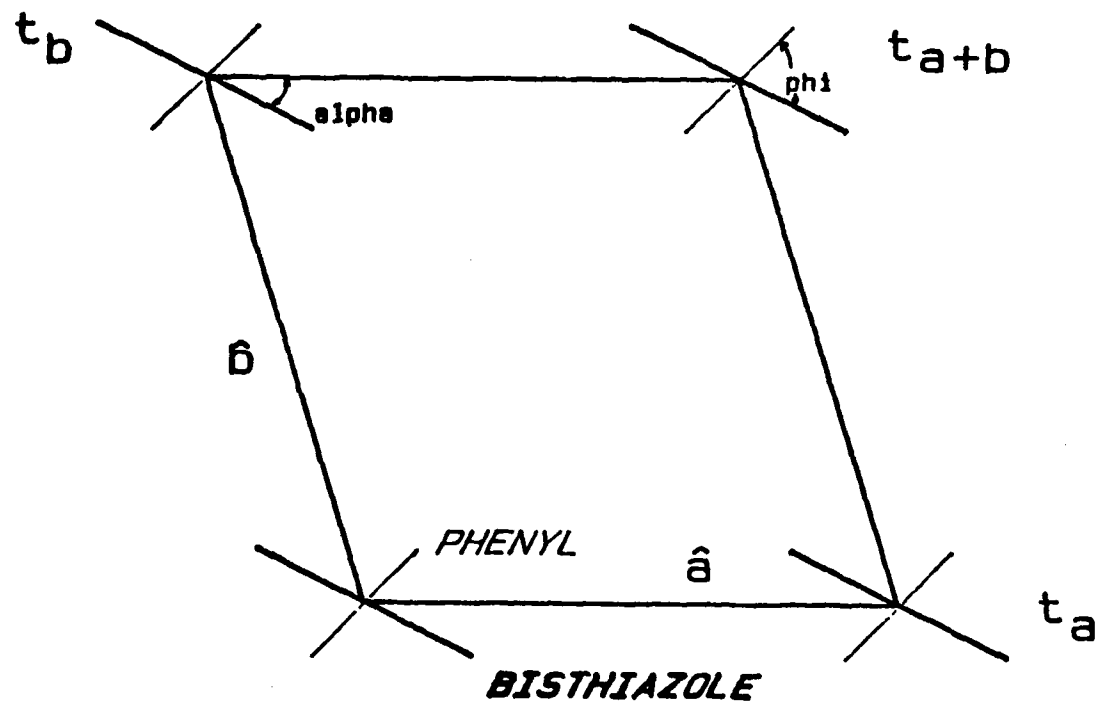


Fig.62 Configuration of packing calculation for PBZT crystal unit cell[15].

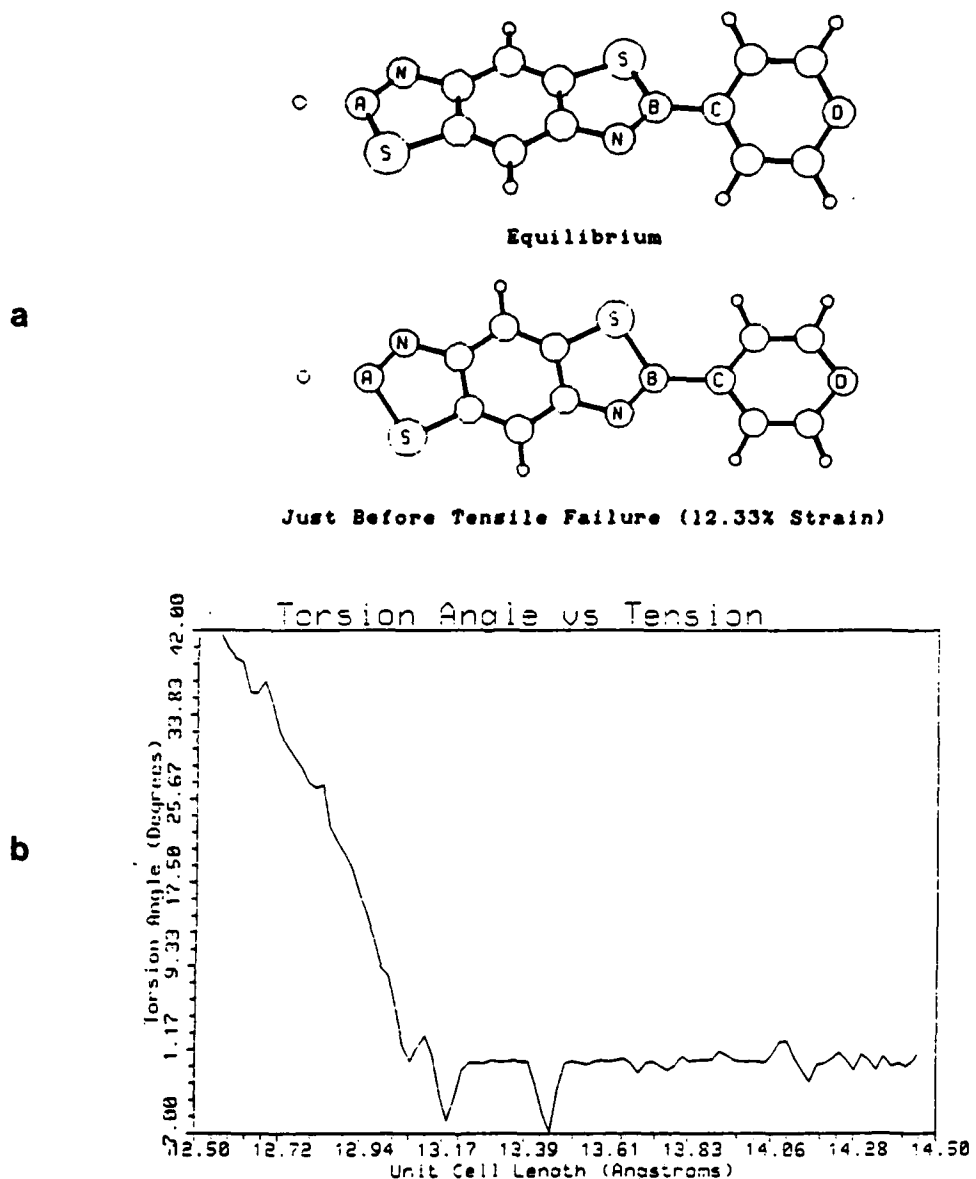


Fig.63 (a) The rotations of phenyl and bisthiazole moieties around the single bond connection under tensile stresses; (b) the variation of the C-C bond (under tension) vs. torsion angle of PBZT unit. As tension increases, the torsion angle decreases from about 42° to zero[101].

conformation could also lead to a change in structure as it does in the *para*-phenylenes[100]. This would contribute to the cell dimension changes in Fig. 60. Furthermore, the structural variation and the movement of phenyl and bisthiazole moieties facilitate the evolution of low-molecular-weight substances which were absorbed by the PBZT molecules. An inflation in the TG curves at about 300-400°C reflects this point (Figs. 55-7).

Above about 500°C, moduli of the samples decrease quickly. In this region, as described above, the PBZT's behavior is noticeably affected by the oxidative and degradative processes.

conformation could also lead to a change in structure as it does in the *para*-phenylenes[100]. This would contribute to the cell dimension changes in Fig. 60. Furthermore, the structural variation and the movement of phenyl and bisthiazole moieties facilitate the evolution of low-molecular-weight substances which were absorbed by the PBZT molecules. An inflation in the TG curves at about 300-400°C reflects this point (Figs. 55-7).

Above about 500°C, moduli of the samples decrease quickly. In this region, as described above, the PBZT's behavior is noticeably affected by the oxidative and degradative processes.

Chapter Five

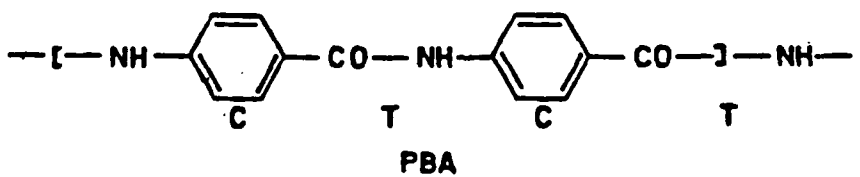
Conclusions and Suggestions

PBT fibers exhibit nonlinear elasticity and negative coefficient of thermal expansion parallel to the fiber axis. These can result in changes in the properties of a composite subjected to a wide variation in temperature. The Young's modulus along the fiber axis direction in a uniaxial lamina can increase rather than decrease with increasing temperature and the stresses generated in the composite can lead to yielding. Furthermore, these effects can lead to variation in the coefficient of thermal expansion in the fiber direction, depending upon the thermal history.

For the exhibited nonlinear elasticity, increasing orientation of the crystals with increasing tensile stress is a major mechanism, but it is not the sole mechanism. For example, if there is a (or more) low temperature relaxation(s) and if its strength decreases with increasing applied tensile stresses, it would contribute to the nonlinear behavior. All the structure factors such as dislocations, pointdefects, shearing on the $hk0$ crystal planes would be involved in this mechanism, especially under high stresses or at high temperature.

The nonlinearity of the PBZT fibers decreases with applied tensile stress and increases with temperature. In the range of 300 to 400°C, PBZT exhibits a mechanical relaxation which is associated with a structural change in the same temperature range. The structural change results from rotational oscillations of the phenyl and bisthiazole moieties about their single bond connection.

Although this paper gives a systematic investigation of the phenomena, mechanism and their relation with the structure, there are still a number of interesting areas in this field to be explored. As to the structural relaxation at about 300 to 400°C, if more research work could be done by means of high temperature NMR or others, some direct judgements may be obtained. It is also interesting that perhaps the structural relaxation at a certain temperature range is a common feature for some high-performance rigid-rod polymers with structures similar to PBZT. For example, in the curve of sonic compliance vs temperature (Fig. 64), for PRD 49 fibers (poly (p-benzamide)) (PBA) with the structure



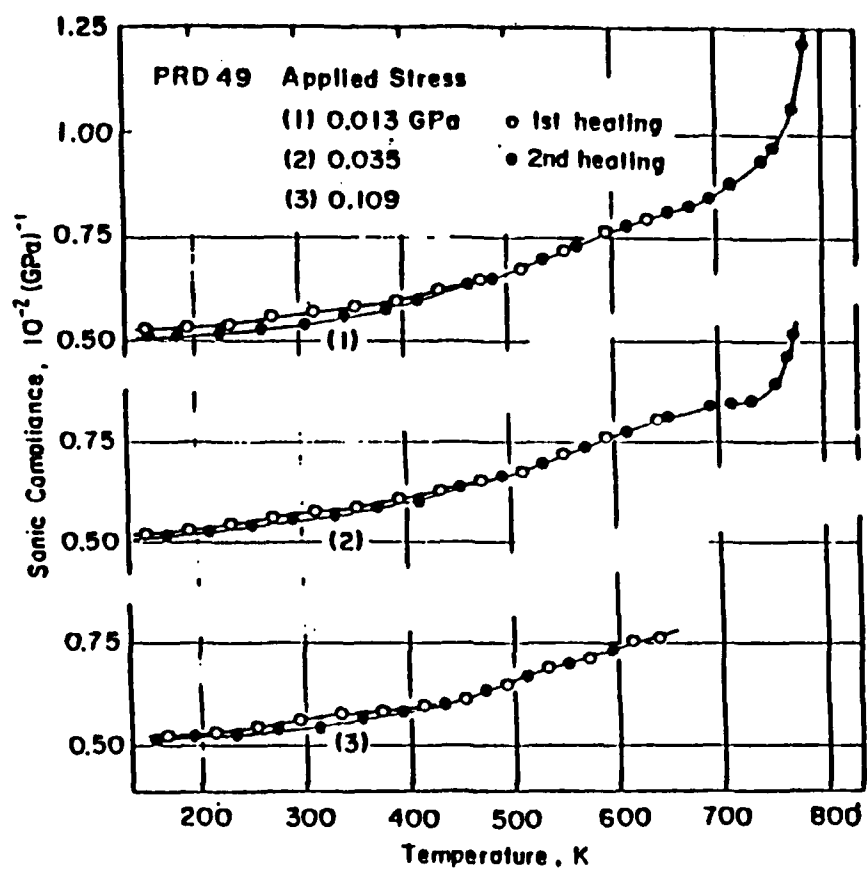


Fig.64 Temperature dependence of sonic compliance for PRD-49 fibers under various tensile stresses[102].

there is an inflection at the temperature around 550 to 700°K (300 to 400°C) too[102]. More studies on this kind of polymer should provide more insight to this question.

As discussed before, in low temperature, there might be one or more relaxations in PBZT structure. It is interesting and useful to complete the modulus (E) - temperature (T) diagram from low temperature through room temperature to high temperature, which would afford more details about the nonlinear behavior and its relationship with structure.

In addition, according to our WAXD work, it has been found that for as-spun PBZT fibers, in the 2θ equatorial scanning, the 2θ position of two characteristic peaks are higher than those for the heat treated PBZT fibers. This suggests that the crystal structure of the as-spun PBZT fibers is different from that of HT fibers. Whether the as-spun fibers retain the same unit cell structure (monoclinic) with different a, b, c axes the angle, or have a different cell such as triclinic or orthorhombic is not clear. Another possibility is a solvate structure. The x-ray diffraction spots for the as-spun fiber are so faint that it is not easy to confirm the unit cell structure. Thus, more work is needed.

References

- [1] W.W.Adams and R.K.Eby, MRS Bulletin, Nov.16/Dec.31, 22(1987)
- [2] S.Saito, C. & E. News, June 15, 13(1987)
- [3] T.A.Heppenheimer, Popular Sci., Sept., 74(1986)
- [4] B.Smith, Aviation Week, Nov.24, 40(1986)
- [5] "The Strength and Stiffness of Polymers", Ed. by A.E.Zachariades and R.S.Porter, Marcel Dekker Inc., N.Y.(1983)
- [6] "High Modulus Polymers", Ed. by A.E.Zachariades and R.S.Porter, Marcel Dekker Inc., N.Y.(1988)
- [7] "New and Specialty Fibers", Ed. by J.Economy, Applied Polymer Symposia No.29, John Wiley Inc., N.Y.(1976)
- [8] "New Polymeric Materials", Ed. by P.F.Bruins, Applied Polymer Symposia No.11, John Wiley Inc., N.Y.(1969)
- [9] "Fiber Science", Ed. by M.Lewin, Applied Polymer Symposia No.31, John Wiley Inc., N.Y.(1977)
- [10] "Strong Fibers", Ed by W.Watt and B.V.Perov, Elsevier Sci. Publish Co. Inc., Amsterdam(1985)

- [11] A.J.Pennings, C.J.H.Schouteten and A.M.Kiel, J. Polym. Sci., C38, 167(1972)
- [12] C. & E. News, July 20, 34(1987)
- [13] T.Kanamoto, A.Tsuruta, K.Tanaka, M.Takeda and R.S.Porter, Polym. J., 15, 327(1983)
- [14] U.S.P. 3,869,429
- [15] S.R.Allen, "Mechanical and Morphological Correlations in PBZT Fibers", Ph.D. Dissertation, U.Mass.(1983)
- [16] J.F.Wolfe, AFWAL-TR-86-4025(1986)
- [17] J.F.Wolfe, AFWAL-TR-80-4201(1981)
- [18] J.F.Wolfe, AFWAL-TR-82-4191(1983)
- [19] J.F.Wolfe and F.E.Arnold, AFML-TR-78-197(1978)
- [20] J.F.Wolfe and F.E.Arnold, U.S.P.4,108,835(1978)
- [21] J.F.Wolfe and F.E.Arnold, U.S.P.4,131,748(1978)
- [22] J.F.Wolfe and F.E.Arnold, Macromolecules, 14, 909(1978)
- [23] J.F.Wolfe and F.E.Arnold, Polymer Preprints, 18(2),414(1977)

- [24] J.F.Wolfe and B.H.Loo, U.S.P. 4,225,700(1980)
- [25] J.F.Wolfe, B.H.Loo and F.E.Arnold, Polym. Preprints, 20(1), 82(1979);
Macromolecules, 14, 915(1981)
- [26] J.F.Wolfe, Polym. Preprints, 19(2), 1(1978)
- [27] J.F.Wolfe, B.H.Loo and E.F.Sevilla, Polym. Preprints, 22(1), 60(1981)
- [28] J.F.Wolfe, P.D.Sybert and J.R.Sybert, U.S.P. 4,533,692(1985); J.F.Wolfe,
P.D.Sybert, J.R.Sybert and R.B.Wilson, U.S.P. 4,533,724(1985)
- [29] J.R.Minter, AFWAL-TR-82-4097(1982)
- [30] T.E.Helminiak, Chem. Preprints, 40, 475(1979)
- [31] E.C.Chenevy, AFWAL-TR-80-4142(1981)
- [32] E.W.Choe and S.N.Kim, Macromolecules, 14, 920(1981)
- [33] E.W.Choe, U.S.P. 4,423,202(1983)
- [34] Y.Cohen and E.L.Thomas, Polym. Engr. Sci., 25(17), 1093(1985)
- [35] S.R.Allen, et al, Macromolecules, 14(4), 1135(1981)
- [36] S.R.Allen, R.J.Farris and E.L.Thomas, J. Mat. Sci., 20, 2727(1985); 20,
4583(1985)

- [37] L.A.Pottick and R.J.Farris, Polym. Engr. Sci., 25(5), 284(1985)
- [38] E.L.Thomas, R.J.Farris and S.L.Hsu, AFWAL-TR-85-4151(1985);
AFML-TR-80-4045(1982)
- [39] S.J.DeTeresa, AFWAL-TR-85-4013(1985)
- [40] S.R.Allen, AFWAL-TR-83-4065(1983)
- [41] U. Mass., AFML-TR-80-4055(1981)
- [42] E.L.Thomas, L.Feldman and R.J.Farris, J. Mat. Sci., 20, 2719(1985)
- [43] E.L.Thomas, S.R.Allen and R.J.Farris, J. Mat. Sci., 20, 3643(1985)
- [44] S.R.Allen, et al, J. Appl. Polym. Sci., 26, 291(1981)
- [45] J.R.Minter, K.Shimamuru and E.L.Thomas, J. Mat. Sci. 16, 3303(1981)
- [46] J.A.Odell, A.Keller and E.D.T.Atkins, ibid., 16, 3309(1981)
- [47] E.J.Roche, T.Takahashi and E.L.Thomas, "Fiber Diffraction Methods",
Ed. by A.D.French and K.H.Garden, ACS symposium series 141(1980)
- [48] L.Feldman, A.M.Zihlif, R.J.Farris and E.L.Thomas, J. Mat. Sci., 22,
1199(1987)
- [49] D.C.Martin and E.L.Thomas, MRS Bulletin, Nov.16/Dec.31, 27(1987)

- [50] W.W.Adams, et al, AFWAL-TR-82-4153(1982)
- [51] W.W.Adams, et al, Zeitschrift fur Kristallographie, 150, 321(1979)
- [52] W.W.Adams, et al, Acta Cryst. B32, 954(1978)
- [53] J.B.Stamatoff, Mol. Cryst. Liq. Cryst., 110(1-4), 75(1984)
- [54] L.A.Pottick, S.R.Allen and R.J.Farris, J. Appl. Polym. Sci., 29(12), 3915(1984)
- [55] E.L.Thomas, K.Shimammura, J.R.Minter, J. Mat. Sci. (Letters), 18, 54(1983)
- [56] A.V.Fratini, Private Communication (1988)
- [57] I.M.Murakami and G.C.Berry, J. Polym. Sci. Polym. Phys. Ed., 14, 1721(1976)
- [58] E.G.Jones, AFWAL-TR-4167(1981)
- [59] S.J.Krause, T.Haddock and W.W.Adams, Bull. Am. Phys. Soc., 29(3), 455(1984)
- [60] A.K.Kulshreshtha and G.E.Price, AFWAL-TR-82-4047(1982); AFWAL-TR-82-4133(1982)

- [61] S.L.Hsu and D.Y.Shen, Polymer, 23, 969(1982)
- [62] S.L.Hsu and C.Chang, J. Polym. Sci. Polym. Phys. Ed., 23, 2307(1985)
- [63] I.M.Ward, Proc. Phys. Soc., 80, 1176(1962)
- [64] I.M.Ward, "Machenical Properties of Solid Polymers", John Wiley & Sons Ltd., New York (1983)
- [65] R.L.McCullough, "Treatise on Materials Sciences and Technology", Vol.10, Ed. J.M.Schultz, Academic Press, New York (1977)
- [66] B.A.Auld, "Acoustic Fields and Waves in Solids", John Wiley & Sons, New York (1973)
- [67] "High Temperature Resistance Fibers from Organic Polymers", Applied Polymer Symposia, Vol. 9, Ed. J. Preston, John Wiley & Sons, N.Y. (1969)
- [68] H.Goldstein, "Classical Mechanics", Addison-Wesley Press Inc., Boston (1951)
- [69] B.W.Shaffer, Proc. Conf. SPI, 18th Sect. G-E (1963)
- [70] M.Takayanagi, Proc. Inst. Congr. Rheol., 4th Part 1, 161, N.Y. (1965)

[71] A.E.Love, "A Treatise on the Mathematical Theory of Elasticity", 4th Ed., Macmillan, N.Y. (1944)

[72] J.J.Smith, H.Jiang, R.K.Eby and W.W.Adams, Polym. Comm., 28(1), 14(1987)

[73] "Ultrasonic Methods in Evaluation of Inhomogeneous Materials", Ed. A.Alippi and W.G.Mayer, Martinis Nijhoff Publishers, Dordrecgt (1987)

[74] R.A.Pethrick, "Progress in Polymer Science", 9(2/3), 263(1983)

[75] R.M.White, J. Appl. Phys., 34, 2123(1963)

[76] C.M.Pereival, J. Appl. Phys. 38, 5313(1967)

[77] M.J.Brienza and A.J.DeMaria, Appl. Phys. Lett. 11, 4(1967)

[78] J.R.Hutchinson and C.M.Pereival, J. Acoust. Soc. Am., 44, 1204(1968)

[79] C.A.Calder and W.W.Wilcox, Rev. Sci. Instrum., 45, 1557(1974)

[80] A.V.Bondarenko, Yu B. Drobot and S.V.Kruglov, Sov. J. Nondestruct. Test, 12, 655(1976)

[81] R.J.Dewhurst, D.A.Hutchins, S.B.Palmer and C.B.Scruby, J. Appl. Phys., 53, 4064(1982)

- [82] W.W.Mosley Jr., J. Appl. Polym. Sci., 3, 266(1960)
- [83] R.J.Samules, "Structured Polymer Properties", John Wiley & Sons, New York(1974)
- [84] P.G.Lenhert and W.W.Adams, J9.3, MRS Fall Meeting, Boston, Nov.28-Dec.3(1988)
- [85] P.G.Lenhert, J.F.O'Brien, W.W.Adams, AFWAL-TR-86-4024(1986)
- [86] I.Sakurada, Y.Nukushima and T.Ito, J. Polm. Sci., 57, 651(1962)
- [87] H.Tadokoro, "Structure of Crystalline Polymers", John Wiley & Sons, N.Y. (1979)
- [88] H.P.Klug and L.E.Alexander, "X-ray Diffraction Procedures", John Wiley & Sons, N.Y. (1962)
- [89] A.M.Hindeleh, D.J.Johnson and P.E.Montague, "Fiber Diffraction Mehtods", ACS Symposium Series 141, Ed. A.D.French and K.H.Gardner, P.149(1980)
- [90] H.Jiang, Microcomputers, 6, 58(1981)
- [91] F.W.Jones, Proc. Roy. Soc., A166, 16(1938)

- [92] A.R.Stokes, Proc. Phys. Soc., 61, 382(1948)
- [93] J.D.Lee and H.W.Pakes, Acta Cryst., A25, 712(1969)
- [94] L.E.Alexander, "X-ray Diffraction Methods in Polymer Science", Wiley Interscience, London (1969)
- [95] D.Hull, "AnIntroduction to Composite Materials", Cambridge Univ. Press, Cambridge (1981)
- [96] E.G.Wolff, B.K.Min and M.H.Koral, J. Mat. Sci., 20, 1141-9(1985)
- [97] J.D.H.Hughes, J.Phys. D: Appl. Phys., 20, 276-85(1987)
- [98] P.Arsenovic, H.Jiang, R.K.Eby, W.W.Adams and J.M.Liu, in Carbon'88, Ed. B.MeEnaney and T.V.Mays, 485-7, IOP Publishing Ltd., Bristol (1988)
- [99] D.N.Rao, Y.Pang, R.Burzynski and P.N.Prasad, Macromolecules, 22(2), 985-9(1989)
- [100] J.L.Baudour, Y.Delugeard and P.Rivet, Acta Cryst., B34, 625(1978)
- [101] S.G.Wierschke, AFWAL-TR-88-4201(1988)
- [102] Tadaoki Ii, Kohji Tashiro, Masamichi Kobayashi and Hiroyuki Tadokoro, Macromolecules, 19, 1809-14(1986)